

MEMS-Based Endomicroscopes for High Resolution *in vivo* Imaging

by

Xiyu Duan

A dissertation submitted in partial fulfillment
of the requirements for the degree of
Doctor of Philosophy
(Biomedical Engineering)
in the University of Michigan
2017

Doctoral Committee:

Professor Thomas D. Wang, Chair
Professor Eric R. Fearon
Associate Professor Kenn R. Oldham
Associate Professor Zhen Xu

DEDICATION

This dissertation is dedicated to my family, for their unconditional love and support.

ACKNOWLEDGEMENT

Primarily, I would like to thank to Professor Thomas D. Wang for his guidance, patience, and kindness. He introduced me to the field of biomedical optics and provided support and resources throughout the course of my research. He created a wonderful multidisciplinary research environment, which allowed me to develop my skills and experience across multiple fields. The research and dissertation would not have been possible without his support. I would also like to express thanks to the guidance and help from other committee members Professor Kenn Oldham, Professor Eric Fearon and Professor Zhen Xu.

I would like to thank my great lab-mates and collaborators. Especially Dr. Haijun Li, who developed all kinds of amazing MEMS devices, and Dr. Gaoming Li, who provided insights and knowledge in optics. I would also like to thank Chi Qiu, Lu Wang and Prashanth K J who helped me with mechanical fabrication. Additionally, I would like to thank Dr. Asha Pant, Quan Zhou, Dr. Supang Khondee and Dr. Xue Li who helped me with the animal experiments. I would like to thank Zhen Qiu, Jongsoo Choi, Miki Lee, Arlene Smith , Coco Tseng and other group members for their efforts in helping me with my projects and research studies.

A lot of my work involves mechanical design and fabrication. I would like to thank Steve Sdoná from LSA machine shop for sharing his knowledge in traditional machining..

I would like to thank our collaborators at University of Washington, Dr. Eric Seibel and Richard S. Johnston for giving the opportunity to learn the scanning fiber endoscope system so I could use the knowledge in my project.

Finally, I would like to thank my wife, Zijing Wu, for her love, patience, and encouragement. I am so thankful for my parents for their unconditional love and support.

TABLE OF CONTENTS

DEDICATION	ii
ACKNOWLEDGEMENT	iii
LIST OF TABLES	xiv
LIST OF FIGURES	xv
ABSTRACT.....	xx
Chapter 1 Introduction.....	1
1.1 Colorectal Cancer	1
1.2 Intra-Vital Imaging of Tissue Epithelium	2
1.3 Confocal and multiphoton microscopy	3
1.4 Actuators for endomicroscopes	6
1.4.1 Distal scanning mechanisms	7
1.4.2 Micro-actuator based endomicroscopes	11
1.5 Peptides as cancer targeting molecular probes.....	12

1.6	Small animal imaging.....	13
1.7	Specific aims	14
1.8	Dissertation overview.....	14
Chapter 2	Materials and Methods.....	16
2.1	Light source.....	17
2.2	Optical fibers for light delivery.....	20
2.2.1	Optical fibers for confocal endomicroscope	20
2.2.2	Optical fibers for multiphoton endomicroscope.....	21
2.3	MEMS based 2D scanner.....	27
2.3.1	MEMS scanner characterization	29
2.3.2	2D scan pattern generation.....	30
2.3.3	Image reconstruction.....	33
2.4	Optical system design.....	35
2.4.1	Numerical aperture.....	35
2.4.2	Beam scanning configurations	36
2.4.3	Scanner parameters and optical performance.....	37

2.5	Data acquisition and image reconstruction	38
2.6	Design flow of an endomicroscope probe.....	39
Chapter 3	Multiphoton endomicroscope	40
3.1	Introduction	40
3.2	Background	41
3.2.1	Two-photon microscopy	41
3.3	Methods.....	42
3.3.1	2D MEMS scanner	42
3.3.2	Optical design.....	45
3.3.3	System architecture	47
3.3.4	Mechanical design and packaging.....	49
3.3.5	System resolution	50
3.3.6	Imaging of mouse colon.....	51
3.4	Results	52
3.4.1	System resolution	52
3.4.2	Imaging of mouse colon.....	53

3.5	Discussion	54
3.6	Summary	56
Chapter 4	Side-view multiphoton endomicroscope.....	57
4.1	Introduction	57
4.2	Methods.....	57
4.2.1	Side-view objective design.....	57
4.2.2	Optical design of the distal probe.....	61
4.2.3	Mechanical design and packaging of side-view probe.....	62
4.2.4	Mechanical design and packaging of the handheld instrument.....	63
4.2.5	Ex vivo imaging of mouse colon tissue	64
4.2.6	In vivo imaging	65
4.3	Results	65
4.3.1	System resolution	65
4.3.2	Lens paper imaging	66
4.3.3	Ex vivo imaging of mouse colon tissue	66
4.3.4	In vivo imaging of mouse colon.....	67

4.4	Discussion	68
4.5	Summary	69
Chapter 5	Side-view confocal endomicroscope	70
5.1	Introduction	70
5.2	Methods	72
5.2.1	System architecture	72
5.2.2	Optical design.....	73
5.2.3	MEMS scanner	74
5.2.4	Mechanical design and packaging.....	76
5.2.5	Imaging performance characterization.....	78
5.2.6	Peptide.....	78
5.2.7	In vivo imaging	78
5.3	Results	80
5.3.1	Imaging performance	80
5.3.2	In vivo imaging	82
5.3.3	Ex vivo validation	83

5.3.4	Mosaic image	84
5.4	Discussion	86
5.5	Summary	88
Chapter 6	Side-Viewing Confocal Endomicroscope for XY/XZ Imaging.....	90
6.1	Introduction	90
6.2	Methods.....	92
6.2.1	System architecture	92
6.2.2	Optical design.....	92
6.2.3	Geometry of the MEMS chip.....	94
6.2.4	3D MEMS scanner	95
6.2.5	Scanner characterization	96
6.2.6	Switchable horizontal/vertical imaging.....	97
6.2.7	Packaging and alignment	98
6.2.8	Resolution and FOV	99
6.2.9	Mouse model of colorectal cancer with tdTomato optical reporter ..	99
6.3	Characterization	100

6.3.1	Resolution and FOV	100
6.3.2	Imaging of 3D fluorescent phantom.....	101
6.4	Applications	102
6.4.1	Imaging of colonic dysplasia with peptide.....	102
6.4.2	Imaging of tdTomato optical reporter mouse.....	103
6.4.3	Inflammation monitoring in the mouse colon	106
6.5	Summary	107
Chapter 7	MEMS-based multiphoton microscopy for vertical sectioning	108
7.1	Introduction	108
7.2	Methods.....	110
7.2.1	System architecture	110
7.2.2	Optical simulation for axial scan.....	112
7.2.3	Lateral MEMS scanner.....	113
7.2.4	Axial MEMS scanner	114
7.2.5	Switchable horizontal/vertical imaging.....	116
7.2.6	Optical properties characterization.....	117

7.2.7	Imaging performance demonstration	118
7.2.8	Tissue preparation	118
7.3	Results	119
7.3.1	PSF simulation	119
7.3.2	Optical properties characterization.....	120
7.3.3	Axial scan performance demonstration.....	121
7.3.4	Tissue imaging	122
7.4	Discussion	123
Chapter 8	Future Works	127
8.1	Side-view multiphoton endomicroscope with distal MEMS scanning .	127
8.2	Side-view multiphoton endomicroscope with remote axial scanning...	129
8.3	Side-view dual axes confocal endomicroscope.....	130
8.4	Widefield endoscope	131
Chapter 9	Conclusion	133
9.1	Summary	133
Appendix	134

References..... 137

LIST OF TABLES

Table 1.1. Comparison of MEMS scanners with different working principles.....	10
Table 1.2. Summary of recently published endomicroscopes using miniature actuators.	11
Table 2.1. Fluorophores used for peptide labelling	18
Table 2.2. Fluorescent proteins.....	18
Table 4.1. Performance comparison of two optical designs	60

LIST OF FIGURES

Fig. 1.1. Carcinoma of the colon arises from a transformation of normal epithelium to dysplasia.....	3
Fig. 1.2. Comparison of resolution and penetration depth for different imaging modalities.	4
Fig. 1.3. Distal scanning mechanisms.....	7
Fig. 1.4. Fiber scanning mechanisms used in endomicroscopes.....	8
Fig. 2.1. Schematic diagram of a typical laser scanning endomicroscope system.	16
Fig. 2.2. Lasers sources for endomicroscope systems.	19
Fig. 2.3. Double clad photonic crystal fiber.....	23
Fig. 2.4. Pulse stretching by the DCPCF.	25
Fig. 2.5. Grating pair pulse compression.	26
Fig. 2.6. Hollow core photonic bandgap fiber.	27
Fig. 2.7. First generation electrostatic MEMS scanner developed by our group.....	28

Fig. 2.8. Laser based MEMS testing platform.	30
Fig. 2.9. Three commonly used scan patterns.	32
Fig. 2.10. Schematic of beam scanning with a 2D scanner.	33
Fig. 2.11. Distortion profile of a 2D beam scanner.	35
Fig. 2.12. Beam scanning configurations.	36
Fig. 2.13. LabVIEW program flow.	38
Fig. 2.14. LabVIEW program interface.	38
Fig. 2.15. Design flow of a MEMS based endomicroscope.	39
Fig. 3.1. 2D MEMS scanner.	43
Fig. 3.2. MEMS scanner characterization.	44
Fig. 3.3. Zemax Simulation.	47
Fig. 3.4. Schematic.	48
Fig. 3.5. Endomicroscope packaging.	50
Fig. 3.6. Image resolution.	52
Fig. 3.7. Imaging results.	53
Fig. 4.1. Side-view optical configurations.	58

Fig. 4.2. Zemax simulation of two side-view objective designs.....	59
Fig. 4.3. PSFs of the two-lens objective.	61
Fig. 4.4. Optical design and lens selection for the distal probe.	62
Fig. 4.5. Distal probe design and packaging.....	63
Fig. 4.6. Handheld probe mechanical design and packaging.....	64
Fig. 4.7. Image resolution.	66
Fig. 4.8. Lens paper imaging.	66
Fig. 4.9. Ex vivo imaging of mouse colon tissue.....	66
Fig. 4.10. In vivo and ex vivo imaging of mouse colon.	67
Fig. 5.1. Optical system schematic.	72
Fig. 5.2. Optical design.....	74
Fig. 5.3. MEMS Scanner.....	75
Fig. 5.4. Packaging and alignment.....	77
Fig. 5.5. Image resolution.	81
Fig. 5.6. Imaging of mouse colonic dysplasia.	82
Fig. 5.7. Ex vivo validation.....	83

Fig. 5.8. Mosaic image of mouse colon in vivo.....	85
Fig. 5.9. In vivo imaging of colonic dysplasia with QRH peptide.	85
Fig. 6.1. Schematic.....	92
Fig. 6.2. Optical design and Zemax simulation.	93
Fig. 6.3. Geometry of the MEMS chip and the reflective mirror.	94
Fig. 6.4. 3D MEMS scanner.	95
Fig. 6.5. Characterization of the MEMS scanner.....	97
Fig. 6.6. Packaging and alignment.....	98
Fig. 6.7. Performance characterization.	100
Fig. 6.8. 3D reconstruction of fluorescent beads phantom.	101
Fig. 6.9. Ex vivo images of mouse colon tissue with EGFP peptide binding.....	102
Fig. 6.10. Ex vivo images of tdTomato mouse colon tissue.	103
Fig. 6.11. Ex vivo images of different organs of tdTomato mouse.	104
Fig. 6.12. In vivo images of tdTomato mouse colon tissue.	105
Fig. 6.13. In vivo and ex vivo images of mouse colon with IBD.	106
Fig. 7.1. Schematic diagram of the 3D multiphoton microscope.	110

Fig. 7.2. Lateral MEMS scanner.....	113
Fig. 7.3. Axial MEMS scanner.....	115
Fig. 7.4. Effect of tilt on PSF.....	119
Fig. 7.5. Axial scan performance characterization.....	120
Fig. 7.6. Multiphoton excited fluorescence images of pollen grains.....	121
Fig. 7.7. Multiphoton excited fluorescence images of mouse colonic epithelium ex vivo.	122
Fig. 8.1. Side-view multiphoton endomicroscope with post-objective MEMS scanning.	128
Fig. 8.2. Side-view multiphoton endomicroscope with remote axial scanning for 3D imaging.....	129
Fig. 8.3. Side-view dual axes confocal endomicroscope.....	131
Fig. 8.4. Wide-field endoscope.....	132

ABSTRACT

Intravital microscopy is an emerging methodology for performing real time imaging in live animals. This technology is playing a greater role in the study of cellular and molecular biology because *in vitro* systems cannot adequately recapitulate the microenvironment of living tissues and systems. Conventional intravital microscopes use large, bulky objectives that require wide surgical exposure to image internal organs and result in terminal experiments. If these instruments can be reduced sufficiently in size, biological phenomena can be observed in a longitudinal fashion without animal sacrifice. The epithelium is a thin layer of tissue in hollow organs, and is the origin of many types of human diseases. *In vivo* assessment of biomarkers expressed in the epithelium in animal models can provide valuable information of disease development and drug efficacy. The overall goal of this work is to develop miniature imaging instruments capable of visualizing the epithelium in live animals with subcellular resolution.

The dissertation is divided into four projects, where each contains an imaging system developed for small animal imaging. These systems are all designed using laser beam scanning technology with tiny mirrors developed with microelectromechanical systems (MEMS) technology. By using these miniature scanners, we are able to develop endomicroscopes small enough for hollow organs in small animals. The performance of

these systems has been demonstrated by imaging either excised tissue or colon of live mice. The final version of the instrument can collect horizontal/oblique plane images in the mouse colon in real time (>10 frames/sec) with sub-micron resolution (<1 μm), deep tissue penetration (~200 μm) and large field of view (700 x 500 μm). A novel side-viewing architecture with distal MEMS scanning was developed to create clear and stable image in the mouse colon. With the use of the instrument, it is convenient to pinpoint location of interest and create a map of the colon using image mosaicking. Multispectral fluorescence images can be collected at excitation wavelength ranging from 445 nm to 780 nm. The instruments have been used to 1) validate specific binding of a cancer targeting agent in the mouse colon and 2) study the tumor development in a mouse model with endogenous fluorescence protein expression. We use these studies to show that we have developed an enabling technology which will allow biologist to perform longitudinal imaging in animal models with subcellular resolution.

Chapter 1 Introduction

1.1 Colorectal Cancer

Approximately 149,000 new cases of colorectal cancer occur annually in the U.S. where the rate of incidence is among the highest in the world (41 cases/100,000 population in 2009-2013) [2]. The average lifetime risk for developing this disease is about 1 in 20 in the industrialized world [3]. Despite the widespread availability of colonoscopy, colorectal carcinoma remains the second most common cause of cancer, and the mortality and morbidity associated with this disease is far more common than expected. The miss rate for colonic adenomas, as determined by tandem colonoscopy, has been found to be as high as 22%, and a significant number of cases of colorectal cancers (2.4 cancer/1000 person-years) have been diagnosed within a year following screening colonoscopy [4]. Moreover, there is evidence that up to 25% of spontaneously occurring adenomas arise from sporadically occurring flat or depressed lesions that may be difficult to visualize by conventional white light endoscopy [5] [6]. These lesions frequently contain high grade dysplasia and progress more rapidly through the adenoma-carcinoma sequence than polypoid adenomas [7]. A greater understanding of molecular target expression patterns over time is needed to develop better strategies for risk stratification and early detection.

1.2 Intra-Vital Imaging of Tissue Epithelium

Transformed cells that develop into cancer of the colon originate within the epithelium of the mucosa, as shown in Fig. 1. Intra-vital microscopy is a powerful tool for studying the molecular mechanisms of epithelial cancer biology in vivo because this technique can directly access this thin, superficial layer of tissue to provide the highest resolution possible in live animals [8] [9] [10] [11]. A miniature fiber optic instrument can be placed in contact with the tissue surface to collect real time images with sub-cellular resolution. These instruments can be either inserted into hollow organs or hand held against the outer body in small animal models [12] [13]. Intra-vital imaging allows for longitudinal (non-terminal) studies to be performed where each animal is used as its own control. This approach can significantly reduce the number of animals needed and can provide a more robust study design. Also, this technique can be adapted for multi-spectral imaging where ligand-receptor interactions and cell tracking behavior can be studied in vivo. These processes are difficult to observe with any other imaging modality.

As shown in **Fig. 1.1**, normal colonic epithelium transforms to a pre-malignant condition (dysplasia) prior to evolving into carcinoma [14]. Molecular changes develop well in advance of morphological changes. Imaging in the vertical cross-section (dashed black box) which is the plane perpendicular to the tissue surface provides a comprehensive view of the epithelium which normally differentiates in the basilar to luminal direction. This orientation also can accurately register the location of biological behavior of interest relative to the tissue surface. Imaging in the horizontal cross-section which is the plane

parallel to the tissue surface reveals a local view of the epithelium along a surface that tends to have a similar degree of differentiation. This imaging orientation is not adequate to provide information about biological behavior either above or below this plane, and can be difficult to register the location relative to the tissue surface.

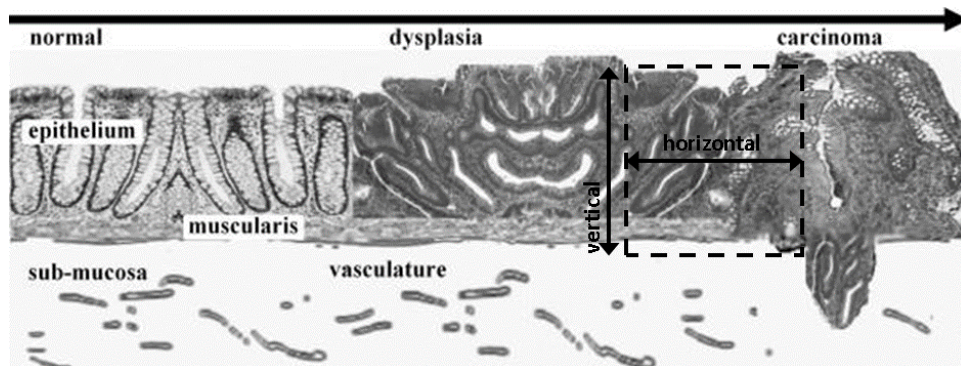


Fig. 1.1. Carcinoma of the colon arises from a transformation of normal epithelium to dysplasia. Subtle molecular changes develop first in the crypts prior to morphological changes in the tissue. Imaging in the vertical cross-section (plane perpendicular to tissue surface) can better detect subtle differences in tissue differentiation patterns and for identifying the early presence of invasion, compared to the horizontal cross-section. **Confocal and multiphoton microscopy**

Standard medical imaging modalities, including ultrasound, CT and MRI, have great penetration depth, but the resolution is not good enough to detect early lesions in the epithelial layer, **Fig. 1.2**. In comparison, optical imaging techniques can provide the resolution and speed needed to detect changes in the cellular and molecular level in real time. OCT has been brought into clinical use recently due to its high spatial resolution. Endoscopic and catheter-based OCT probes have been developed to image esophagus and cardio-vasculatures in vivo [15] [16]. Although OCT can detect morphology changes in the tissue with several millimeters' penetration, it is not sensitive to fluorescence and thus lacks molecular specificity. Confocal and multiphoton microscopy (MPM) can achieve

submicron resolution in real time, a level of performance that cannot be matched by any other imaging modality. They can also be used to visualize multiple fluorophores at the same time. However, light is highly scattered in tissue, and sophisticated methods are needed to produce clear images.

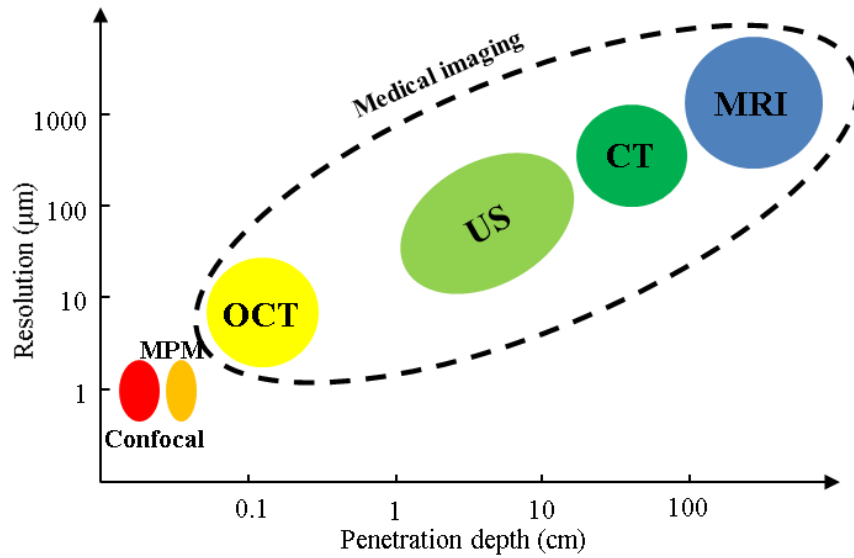


Fig. 1.2. Comparison of resolution and penetration depth for different imaging modalities.

Confocal microscopy uses a pinhole which is placed before the detector such that only the light that originates from within the focal volume to be collected, and the out of focus light will be rejected [17] [18]. To form an image, a pair of galvo scan mirrors are used to divert the laser beam in orthogonal orientations such that the specimen is illuminated point by point in a raster pattern. Light signal is collected at each point and the image is reconstructed serially. This technique is known as optical sectioning and can produce a high resolution image at a fixed depth below the tissue surface. Optical sectioning, or depth discrimination capability is the key difference between a conventional

microscope and a confocal microscope. The imaging depth of confocal microscopy is typically around 100 μm [19].

Multiphoton microscopy, also known as nonlinear or two-photon microscopy, is an alternative to confocal microscopy with advantages specifically in deep tissue imaging. In lightly scattered tissue, about 1 mm penetration depth has been demonstrated using two-photon microscopy [20] [21] [22]. The two-photon effect occurs when two lower energy (longer wavelength) photons arrive at a biomolecule simultaneously to excite fluorescence and generate a higher energy (shorter wavelength) photon [23]. Two photon absorption is a rare event, and the probability of this event is dependent on the square of the illumination intensity, therefore a high numerical aperture objective in the single axis configuration is used to maximize the intensity at the focus and increase the collection efficiency. Because of this nonlinear relationship, two photon absorption only occurs in the focal volume, so it is less sensitive to tissue scattering and there is less photobleaching in comparison to that for single photon fluorescence [24] [25]. Moreover, because of the use of longer excitation wavelengths, deeper tissue penetration could be achieved. However, most two-photon instruments use a bulk microscope objective that requires a large region of exposure to image the target organs, resulting in terminal experiments [1].

For both confocal and multiphoton microscopy, optical sectioning images can be collected at sufficiently fast frame rates to observe biological behavior in small animal models with minimal disturbance from motion artifacts caused by breathing displacements and heart beating.

1.4 Actuators for endomicroscopes

Both confocal and multiphoton microscopy rely on galvanometers, or commonly called as galvos, to perform high speed laser scanning. A galvo scanner typically consists of a motor and a mounted mirror with position sensors for precise control. The size of a galvo scanner is in the range of centimeters, which is too big to be integrated into an endomicroscope form factor.

For endomicroscopy applications, the location of the beam scanner is either proximal or distal with respect to the light source [12]. Proximal scanners are located between the light source to the flexible fiber, and are often used with a fiber bundle [26] [27] [28] [29] [30] [31]. Most of these fiber bundles consist of more than 100,000 individual step-index fibers with total diameter from hundreds of microns to a few millimeters and core-to-core spacing of around 5 microns [32]. The spatial arrangements of the fiber cores are identical at both ends to maintain the same intensity profile through transmission. Each core of the fiber bundle serves as a pinhole to reject out of focus light. The advantage of using a proximal scanner is that a conventional galvo scanner can be used since the scanning is occurring before entering the miniature probe. Real time imaging can be achieved using high speed galvo scanners, and the imaging rate can be further improved using line/multipoint scanning instead of single point scanning [33] [34] [35]. The use of fiber bundles also has a few drawbacks, however, including high manufacturing cost, limited spatial resolution by the number of fiber cores and low depth penetration. The major disadvantage is the pixelation effect due to the empty spaces between fiber cores, resulting

in limited lateral resolution. Light transmission in the cladding could also result in reduced imaging contrast. Various image processing techniques have been developed to smoothen the imaging pixelation effect [36]. Another method has been demonstrated by Choi's group that, instead of using a fiber bundle, a single multimode fiber can be used with proximal scanning for an ultra-compact endomicroscope [37]. Direct image transmission through a multimode fiber is possible due to the existence of multiple spatial modes inside the fiber. A clean image can be recovered using the speckle pattern from the multiple reflections of light. The limitation of this approach is that bending of the fiber will change its transmission matrix, therefore it's applicable only for rigid type endoscopes.

1.4.1 Distal scanning mechanisms

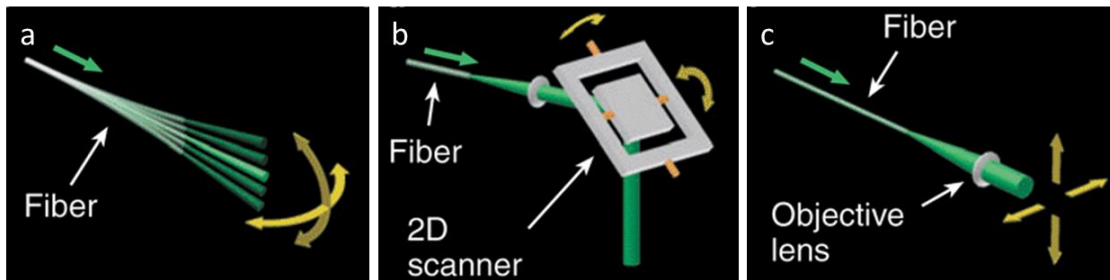


Fig. 1.3. Distal scanning mechanisms. a) Fiber scanning. b) Beams scanning with micro-mirrors. c) Lens scanning. Figure adapted from [12].

To achieve better image quality, distal scanning mechanisms are needed. However, there are challenges to develop small actuators which are small enough to fit inside the endomicroscope probe. With limited space, it is also difficult to achieve high scanning speed. The probe may also be sensitive to shocks, vibrations, pressure and temperature. The following discussion focuses on three types of scanning mechanisms: **fiber scanning**, **beam scanning** and **lens scanning**, as shown in **Fig. 1.3**.

1.4.1.1 Fiber scanning

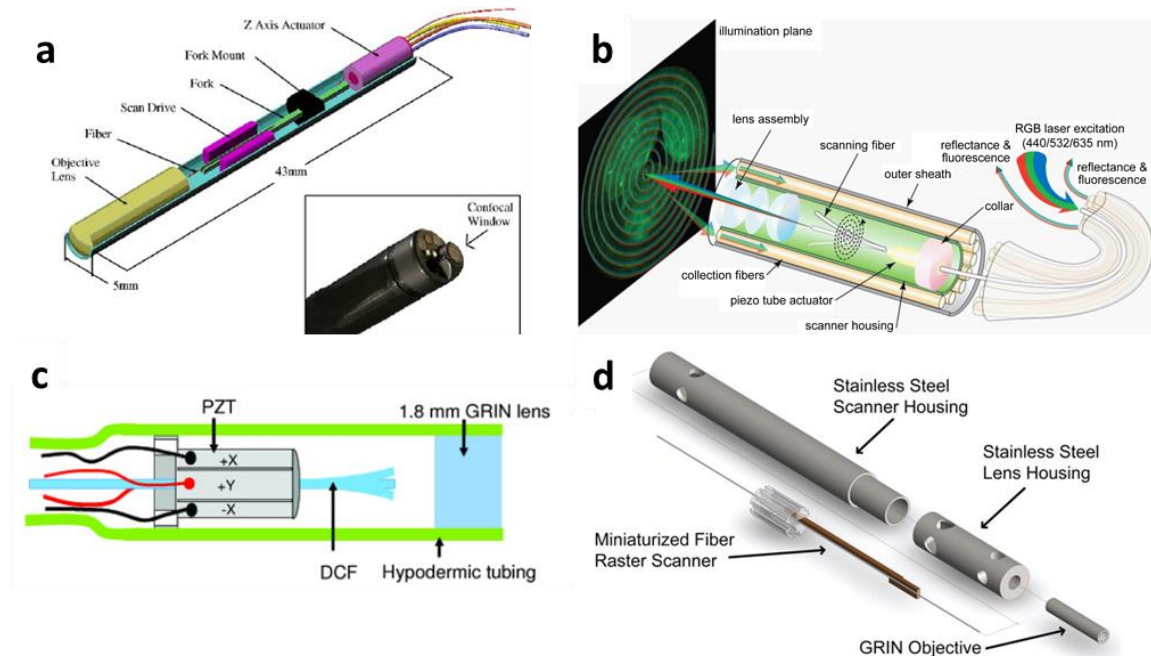


Fig. 1.4. Fiber scanning mechanisms used in endoscopes. a) Electromagnetic fiber scanner used in a medical endoscope with confocal imaging modality, developed by Optiscan and Pentax. b) Piezoelectric tube for fiber scanning in a spiral pattern, used in a wide field scanning fiber endoscope and c) two-photon endomicroscope. d) A two-photon endomicroscope using two piezoelectric bending cantilevers for raster scanning.

Single-mode optical fibers are used for light delivery in endoscopes, therefore it is natural to scan the fiber directly and use optics to relay the image formed by the fiber tip onto the sample plane. Fiber scanning technology has many advantages, including ultra-compact size, robustness and high scanning speed. The first clinical confocal endomicroscope system was developed by Optiscan Pty. Ltd. (Victoria, Australia) and integrated into a medical endoscope (Pentax Precision Instruments EC-3870K, Tokyo, Japan) [38]. A single-mode optical fiber is attached to a miniature magnet and 2D scanning was performed two pair of coils, as shown in **Fig. 1.4a**. The images are collected in horizontal sections at a frame rate of 0.8 Hz with 1024×1024 pixels. Axial scanning is

performed with a shape memory alloy (SMA) actuator that translates the focal volume over a range of 250 μm .

Seibel's group developed scanning fiber endoscopes with outer diameter as small as 1 mm, **Fig. 1.4b**, using piezoelectric tube actuators [39] [40]. The fiber operates in resonance with >10 kHz frequency in both axes and it is scanned in a spiral pattern. Images were acquired at a 30 Hz frame rate with 500x500 pixels. The instrument was later adapted to a two-photon endomicroscope by changing the fiber to a hollow-core photonic crystal fiber and adding a second fiber for fluorescence collection [41]. Shown in **Fig. 1.4c**, Li's group also used piezoelectric tube actuators to develop a multiphoton endomicroscope probe, with a double clad fiber for light delivery and fluorescence collection [42]. Also using a spiral scan pattern, Imaging rate of 2.6 Hz was reported with 512x521 pixels [43]. Xu's group developed another multiphoton probe using two piezoelectric strips, **Fig. 1.4d**, to perform 2D scanning in a raster scan pattern. The fast axis operates in resonant with 1.05 kHz, results in a frame rate of 4.1 Hz with 512x512 pixels [44].

The vibratory motion of a fiber scanner can be modeled as a cylindrical cantilever with base excitation and fixed-free boundary conditions [39]. The resonant frequencies of different bending modes of the fiber scanner are a function of its length, shape and material properties [45]. One limitation of this technology is that the choice of the fiber will affect the scanning performance. Special care is needed during the assembly process since the free length of the fiber will also impact the scanning frequency, making mass fabrication

difficult. Furthermore, since the fiber tip has an un-planar motion in resonance, complicated optical design is needed to compensate the change of fiber tip position [46].

1.4.1.2 Beam scanning

Table 1.1. Comparison of MEMS scanners with different working principles.

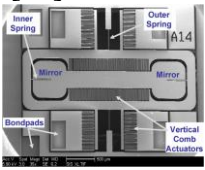
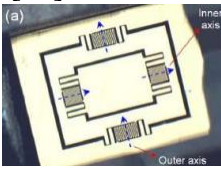
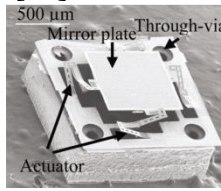
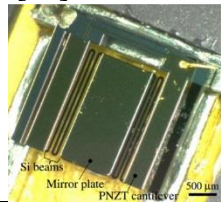
Actuation Mechanism	Electrostatic	Electromagnetic	Electrothermal	Piezoelectric
Scanner	[48] 	[49] 	[50] 	[51] 
Fabrication	Simple	Simple	Moderate	Complex
Integration complexity	Simple	Complex, require coil/magnet	Simple	Simple
Voltage (V)	High (>30 V)	Low (< 20V)	Low (< 10 V)	Low (< 20 V)
Operation mode	Resonant	DC/Resonant	DC/Resonant	DC/Resonant
Mechanical tilt (°)	+/- 10	+/- 20	+/- 20	+/- 10
Power consumption	Low	~200 mW	~100 mW	Low

Table-top confocal and microscopes rely on galvo scanners, or galvanometers, which are mirrors mounted on dc motors with internal position feedback. These scanners are in the scale of centimeters, which are too big for endomicroscopy applications. With recent development of micro electromechanical systems (MEMS) technology, miniature scanning mirrors have been developed and integrated into endomicroscopes. MEMS

scanning technology has the advantages of high speed, small in size (5 mm or smaller), and ease of batch fabrication [47]. These MEMS scanners are designed mainly based on the actuation principles of **electrostatic**, **electromagnetic**, **electrothermal** and **piezoelectric**.

Comparison between these actuation principles is summarized in **Table 1.1**.

1.4.2 Micro-actuator based endomicroscopes

Table 1.2. Summary of recently published endomicroscopes using miniature actuators.

Modality	Reference, Year	Actuation mechanism	OD (mm)	Resolution $\Delta x \times \Delta z$, (μm)	FOV (μm^2)	Depth (μm)	Frame Rate (Hz)
Confocal	[38], 2004	EM fiber scanner	5	0.7 x 7	500 x 500	200	0.8/1.6
	[56], 2005	MEMS	3.3	0.5 x 2.9	100 x 100	N.R.	20
	[57], 2012	MEMS	5.5	5 x 6.5	362 x 212	140	5
	[58], 2013	MEMS x 2	7	1 x 7	180 x 180	380	0.75
	[59], 2014	Piezo tube	2.5	1.7 x 19	200 x 200	200	N.R.
	[60], 2016	MEMS	4.2	0.87 x 13.2	300 x 400	100	5 - 10
Multi-photon	[61], 2010	Piezo tube	2.8	1.5 x 9.2	150 x 150	N.R.	1.1
	[44], 2011	Piezo strips	3	0.8 x 10	110 x 110	70	4.1
	[62], 2011	MEMS	9.6	1.27 x 13.5	130 x 100	N.R.	7
	[63], 2012	Piezo tube	2	0.69 x 6.15	110 x 110	15	2.7
	[64], 2013	MEMS	3	1 x 24	70 x 70	N.R.	N.R.
	[65], 2013	MEMS	N.R.	0.6/2 x N.R.	59 x 93 / 178 x 280	N.R.	34
	[66], 2014	Piezo tube	3.5	0.67 x 3.1	100 x 100	N.R.	N.R.
	[67], 2015	MEMS	3.4	2 x 9	300 x 300	60	5 - 10
	[68], 2015	Piezo tube	2.2	0.8 x 12	450 x 450	300	8
	[69], 2016	MEMS	40	1.3 x N.R.	151 x 236	N.R.	0.4
	[70], 2016	Piezo strips	3.5	2.2 x 9.1	200 x 200	N.R.	1.25

Recent advancements in miniature optics, availability of fiber-optics, and emergence of micro-actuators have allowed for the technique of confocal microscopy to be performed in vivo through medical endoscopes to perform rapid, real-time optical assessment of tissue pathology [52] [10] [53]. Recently, fiber-optic two-photon instruments have also been developed that use photonic crystal fibers for femtosecond pulse delivery and micro-actuators for beam scanning [54] [55]. The use of these endomicroscopes enables sub-cellular resolution optical sectioning in small animals and in human subjects. **Table 1.2** summarizes recently developed endomicroscopes using micro-actuators.

1.5 Peptides as cancer targeting molecular probes

Peptides have demonstrated great promise for clinical use to detect overexpressed cell surface targets from dysplastic tissue during endoscopy [71] [72]. Peptides have a number of pharmacokinetic advantages because of their small size and low molecular weight (<1 kilodalton). Compared with antibodies and other much larger molecular probes, peptides have better vascular permeability, improved tissue penetration, and faster circulatory clearance. The specificity of peptides can be very high because of the large diversity of sequences possible [73]. Also, because of their flexibility for fluorophore labeling [74], it is feasible to simultaneously image multiple targets to address tumor heterogeneity.

Researchers from our lab have previously developed peptides which bind specifically to cell surface targets, which are overexpressed in colonic adenomas. These targets include including EGFR [75], Claudin-1 [76] and HER2 [77]. After labelling with

Cy5.5, peptide binding to specific targets was validated in vivo in a mouse model of spontaneous colorectal cancer. All the in vivo validation studies were performed using an NIR wide-field fluorescence endoscope. In order to perform further validation in the cellular level in a live animal, we need to develop a new imaging technology specifically for this purpose.

1.6 Small animal imaging

In vivo imaging of small animals, such as mice, is an essential component for preclinical biomedical research and the demand is increasing [78] [79] [80] [81]. Mice are mostly commonly used among all kinds of small animals due to the fact that they are small in size, easy to breed, short lifespan and genetical and physiological similarities to human. Mice can develop conditions that are representative of human disease, including cancer. For in vivo peptide validation, our lab used a CPC;Apc mouse model of colon cancer. In this mouse model, the APC gene is deleted in colonic epithelium [82], resulting in spontaneous formation of colonic adenomas. This model is closely related to human disease because APC mutations are found in more than 80% of colorectal cancers [83]. We used a rigid small animal endoscope (Karl Storz Veterinary Endoscopy-America, Goleta, CA) to image the distal portion of the colon. There is a need to develop high resolution imaging tools to study small animals.

1.7 Specific aims

The overall goal of the research plan is to develop a miniature endomicroscope to study small animals with high spatial and temporal resolution. The instrument will be able to collect horizontal/vertical images in the mouse colon in real time (>10 frames/sec) with sub-cellular resolution ($<5\ \mu\text{m}$), deep tissue penetration ($>200\ \mu\text{m}$) and large field of view ($>300\ \mu\text{m}$). Imaging performance will be demonstrated using fluorescence-labeled peptides that specifically bind to over expressed cell surface targets.

- **Specific Aim 1:** Design, assemble, and package a MEMS based confocal or multiphoton endomicroscope for in vivo imaging in the mouse colon with subcellular resolution.
- **Specific Aim 2:** Develop algorithms and software to control the 2D MEMS scanner and reconstruct images in real time.
- **Specific Aim 3:** Characterize instrument performance using imaging phantom and mouse tissue.
- **Specific Aim 4:** Demonstrate the usefulness of the instrument by imaging specific peptide in vivo in the mouse colon.

1.8 Dissertation overview

Chapter 1: Introduction and background information.

Chapter 2: Materials and methods used for the development of the following endomicroscopes.

Chapter 2: Handheld, front view multiphoton endomicroscope.

Chapter 3: Handheld, side-view multiphoton endomicroscope

Chapter 4: Side-view confocal endomicroscope for in vivo imaging.

Chapter 5: Side-view confocal endomicroscope with switchable horizontal and oblique plane imaging.

Chapter 6: Agitation free all MEMS based multiphoton microscope for 3D imaging.

Chapter 7: Future Works.

Chapter 8: Conclusion.

Chapter 2 Materials and Methods

A laser scanning endomicroscope system consists of two subsystems: the endomicroscope probe and the imaging station, as shown **Fig. 2.1**. All the different type of endomicroscope systems will be based on this schematic.

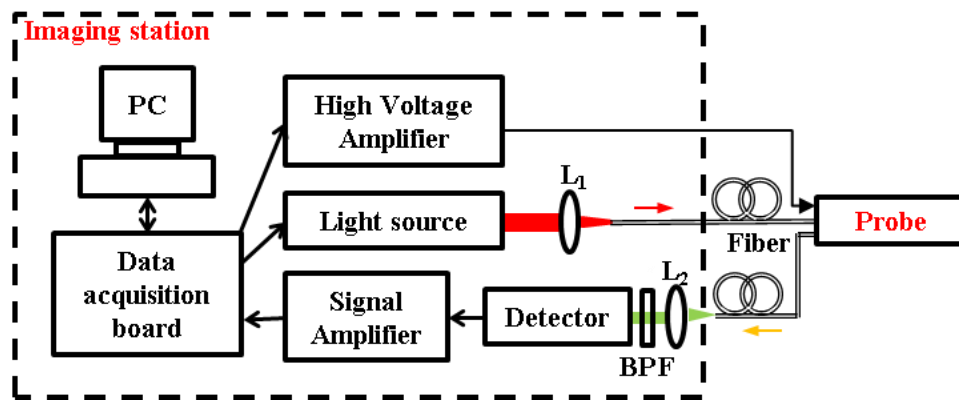


Fig. 2.1. Schematic diagram of a typical laser scanning endomicroscope system.

The probe is usually designed to be inserted into the hollow organs of small animals or passed through an instrument channel of a wide-field endoscope for clinical use. The probe is connected to the imaging station using a flexible catheter which houses optical fibers and electrical wires for information transmission. The challenges of designing an endomicroscope probe are mainly in the development of a micro actuator for beam scanning and the miniature optics around it. The design criteria for the probe mainly includes the mechanical dimension, lateral and axial resolutions, field of view (FOV),

frame rate and sensitivity. The challenges of designing the imaging station include precision actuator control, high speed data acquisition, weak signal detection and real-time image reconstruction. For the whole system to function properly, it is critical to ensure every single component in the system is selected or designed correctly.

This chapter is focused on the overall design flow of the system, as well as the specific design and material choice of each component. A detailed discussion of the theory behind laser scanning microscopy is also included. The design of the instruments covered in later chapters will be based on the methods and principles established in this chapter.

2.1 Light source

Both non-coherent light sources, such as arc lamps, halogen lamps and light-emitting diodes, and coherent light sources, such as laser, have been used in confocal microscopy [84] [85]. Lasers are ideal light sources for confocal microscopy due to because of the properties including high brightness, narrow bandwidth, low noise and can be focused to a tiny spot [86]. Since variation in the light source may be interpreted as change of reflectance or fluorescence from the specimen, the intensity stabilities of lasers are also important. Biologists use a wide range of fluorophores, with excitation wavelengths ranging from 400 nm to 800 nm. In modern laser scanning confocal microscopy (LSCM), multiple lasers can be used simultaneously to image multiple fluorescent probes at the same time. When choosing a light source for the instrument, first we should know what is the biological application and what fluorophores will be used. Our lab has previously developed peptide labeled with several different fluorophores,

summarized in **Table 2.1**. We also plan to use the instrument to visualize genetically engineered mouse models with fluorescent protein expression, summarized in **Table 2.2**.

Table 2.1. Fluorophores used for peptide labelling

Dye	Ex (nm)	EM (nm)
DEAC [40]	432	472
FITC [72]	495	518
TAMRA [40]	541	561
Cy 5	650	670
Cy5.5 [87] [88] [75] [77] [76] [89]	675	694
IRDye 800CW [90]	774	789

Table 2.2. Fluorescent proteins

Fluorescent protein	Ex (nm)	EM (nm)
mCFP [91] [92]	434	477
EGFP [91] [92]	488	511
EYFP [91] [92]	514	527
tdTomato [93]	554	581
RFP [91] [92]	563	582

Two-photon microscopy also relies on lasers as the light source, but a different type of laser is used. As two-photon absorption happens when two photons with the same wavelength are absorbed by the same molecular at the same time, the probability for this to happen is very low [23]. To increase the probability of two-photon absorption, a high intensity light source is needed. Compared to continuous wave (CW) lasers, which are commonly used in confocal microscopy, pulsed lasers are preferred because they can achieve high peak intensity with the same average intensity. It has been shown that two-

photon absorption of a fluorophore will be about the same, using a 10 W continuous-wave laser or a 30 mW from a typical femtosecond pulsed laser [94].

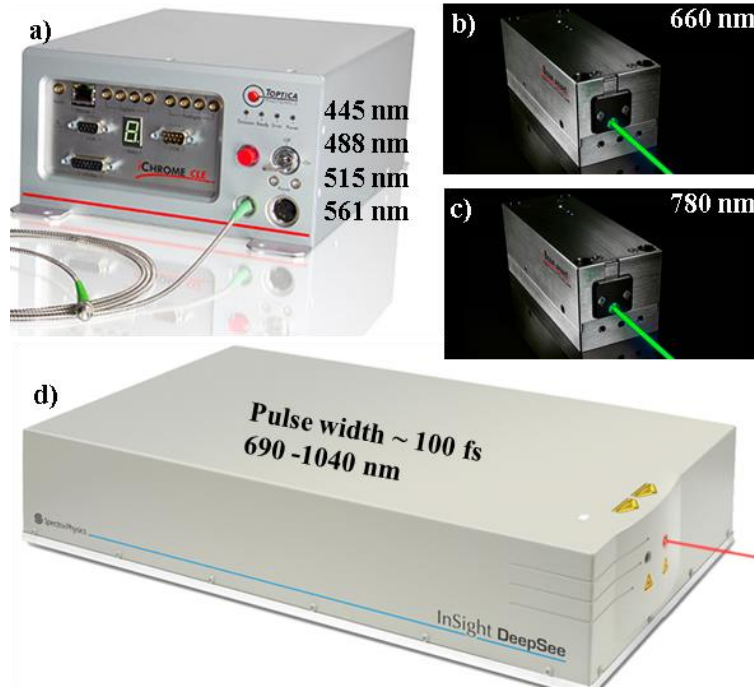


Fig. 2.2. Lasers sources for endomicroscope systems. a) Multi laser engine with four laser lines: 445, 488, 515 and 561 nm. Single wavelength diode lasers with b) 660 nm and c) 785 nm. d) Femtosecond pulsed laser for two-photon imaging, with tunable laser wavelength from 690 to 1040 nm and pulse width of 100 fs. Images retrieved from <http://www.toptica.com/> and <https://www.newport.com>.

We chose multiple laser sources to be integrated into our imaging system, as shown in **Fig. 2.2**. For confocal endomicroscopy, we chose a multi laser engine (iChrome MLE, Toptica, **Fig. 2.2a**) and two single wavelength diode lasers (iBeam Smart 660-s and 785-s, Toptica, **Fig. 2.2b,c**), with wavelength of 445, 488, 515, 561, 660 and 785 nm. This wavelength range covers most of the fluorescent dyes and proteins used in our lab. For multiphoton endomicroscopy, we have an ultrafast Ti-Sapphire laser (Mai Tai Deepsee HP

DS, Spectra Physics) with 100 fs pulse width, 80MHz repetition rate and a tunable output wavelength from 690 to 1040nm.

2.2 Optical fibers for light delivery

To direct a laser beam into a small imaging probe while maintaining flexibility, optical fiber is a key element for an endomicroscope system. With the use of optical fibers, laser beam property, including spatial profile, intensity and polarization, could be preserved even when the distal probe is moving along curved lumen of animal or human organ [32]. Here we limit our discussion to optical fibers for confocal and multiphoton endomicroscopy.

2.2.1 Optical fibers for confocal endomicroscope

Single-mode fiber has a very small inner core surrounded by an outer cladding such that the light is constrained only in the core by total internal reflection. Since the small core size only allows for a single spatial mode to be transmitted, the output beam can be collimated and focused to a diffraction-limited spot for high resolution imaging [32]. The small core ($< 10\mu\text{m}$) can also be used as a confocal pinhole to reject out-of-focus reflectance or fluorescence emission [95]. These properties make single-mode fiber ideal for light delivery for a confocal endomicroscope.

One of the issues arises when using a single-mode fiber for confocal imaging is that background noise can be generated from the back reflection of the illumination light from both ends of the fiber. A strong reflection of the excitation laser beam can partially pass

through the fluorescence detection filter. This is even more problematic when imaging in the reflective mode since the reflected signal from biological tissue is much weaker than the back reflection from the fiber tip. There are three ways to suppress the back reflection: angle polishing of fiber ends, index matching of the fiber core, or a layer of anti-reflection (AR) coating. We chose to use angle polishing such that the reflected beam is directed out of the detection beam path.

2.2.2 Optical fibers for multiphoton endomicroscope

Ultrafast laser pulses with ~ 100 fs pulse width and nanojoule (nJ) pulse energy are commonly used in multiphoton imaging [12]. Maintaining the pulse width after fiber-optic light delivery is critical for constructing a fiber based multiphoton endomicroscope. However, light transmission through an optical fiber is usually accompanied by group velocity dispersion and self-phase modulation, both of which will broaden the laser pulse.

The group velocity is defined by velocity of the envelope of a pulse propagates through a medium. Group velocity dispersion, or GVD, of light occurs when different optical frequency components have different group velocities in a wave guide or an optical fiber. GVD can be quantified by the derivative of the inverse group velocity with respect to the angular frequency:

$$GVD = \frac{\partial}{\partial \omega} \frac{1}{v_g} = \frac{\partial}{\partial \omega} \frac{\partial k}{\partial \omega} = \frac{\partial^2 k}{\partial \omega^2} \quad (2.1)$$

In most cases, group velocity decreases for increasing optical frequency or decreasing wavelength, and this is called normal dispersion. Normal dispersion generates positive GVD while anomalous dispersion generates negative GVD. Optical fiber manufacturers report GVD as a derivative with respect to wavelength, with units of ps/(nm km). The quantity is called dispersion parameter:

$$D_\lambda = -\frac{2\pi c}{\lambda^2} GVD = -\frac{2\pi c}{\lambda^2} \frac{\partial^2 k}{\partial \omega^2} \quad (2.2)$$

For an optical fiber with length L , the frequency dependent delay of the different spectral components of the pulse is quantified using group dispersion delay (GDD):

$$GDD = L \cdot GVD = -\frac{\lambda^2 L}{2\pi c} D_\lambda \quad (2.3)$$

To compensate GDD introduced by optical fibers, a sequence of prisms or gratings with angular dispersion could be used to produce negative GDD [96] [97]. Negatively pre-chirped pulses could exit the fiber with zero dispersion by properly adjusting the pulse compressors. However, self-phase modulation (SPM), which distorts the pulse in a nonlinear manner, is difficult to compensate. Due to the optical Kerr effect, intense ultra-short pulses could induce a varying refractive index when interacting with the fiber silica core [98]. This leads to a phase shift and spectral distortion which depends on the pulses' temporal profile and intensity. Because of this nonlinear effect, SPM is very difficult to compensate and should be avoided for ultra-short pulse delivery.

Recently, photonics crystal fibers (PCFs) have been developed which can help reduce the effect of SPM [99]. Conventional fibers rely on total internal reflection principle to confine the light in the guiding material. In contrast, by controlling the hole size and distribution in PCFs, exact effective refractive index of the cladding can be achieved and results in the development of PCFs with larger mode area [100]. Since the efficiency of SPM in fibers strongly depends on the peak power, it is reduced greatly by distributing laser power to a larger effective area in the fiber [101].

We mainly considered two fibers which have been adopted in several studies: a double clad photonic crystal fiber (DC-165-16-Passive, NKT Photonics) and a hollow core photonic bandgap fiber (HC-800-02, NKT Photonics).

2.2.2.1 Double clad photonic crystal fiber (DCPCF)

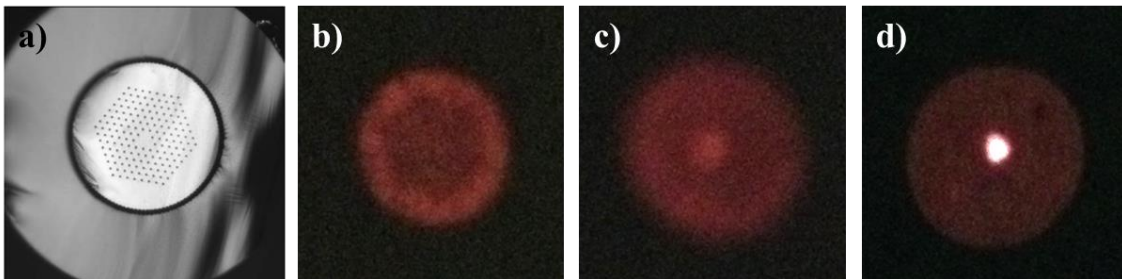


Fig. 2.3. Double clad photonic crystal fiber. a) End face of the fiber, showing the core, the large area inner cladding and the outer cladding. Figure adapted form NKT Photonics website. b) Light mainly coupled in the inner cladding. c) Light in both inner cladding and the core. d) Light mainly in the core.

This fiber was first demonstrated for multiphoton microscopy in [102] [103]. It can use the core to deliver the excitation beam and use the inner cladding to collection fluorescence signal. As shown in Fig. 2.3a, the fiber has a large core with 16 μm in diameter

and an inner clad diameter of 163 μm . It provides single mode operation in the core for wavelength longer than 700 nm. Compared to traditional small core single mode fiber, its large core diameter helps reduce the nonlinear effect. The inner cladding has a high NA of about 0.6 for high collection efficiency of the back scattered light. The detection efficiency of the fiber used in a microscope setup is shown to be 40 times more than that of the normal single-mode fiber [104]. A one meter long fiber was used in our experiment setup and the wavelength is 750 nm throughout the following experiments.

To match the NA and core size of the fiber, we used an objective with $f = 18$ mm (RMS 10X, Thorlabs) for coupling. Special care needs to be taken during the coupling of the DCPCF. For traditional single mode fiber coupling, coupling efficiency is measured at the fiber output using a power meter. However, this is not sufficient for the DCPCF, since coupling in the inner cladding could also give high coupling efficiency. Therefore, a telescope is constructed to magnify the output fiber tip and project onto a screen, as shown in **Fig. 2.3b-d**. Although the coupling efficiencies are very similar, the light is coupled into different regions of the fiber. For **Fig. 2.3b**, the light is only coupled in the inner cladding. For **Fig. 2.3c**, the light is coupled in both the inner cladding and the core. While in **Fig. 2.3d**, the light is mainly in the core, which is the desired coupling mode.

At a wavelength around 750 nm, longer wavelength parts propagate with higher speed in the material, generating a positive dispersion. Dispersion of the laser pulse is observed after transmission through 1 meter of the DCPCF. The laser has a minimum of 100 fs pulse width, and it is measured to be 150 fs at the laser output, due to a built-in

prechirp unit in the laser, **Fig. 2.4a**. At the fiber output, the pulse width is stretched and it is measured to be around 1080 fs, **Fig. 2.4b**.

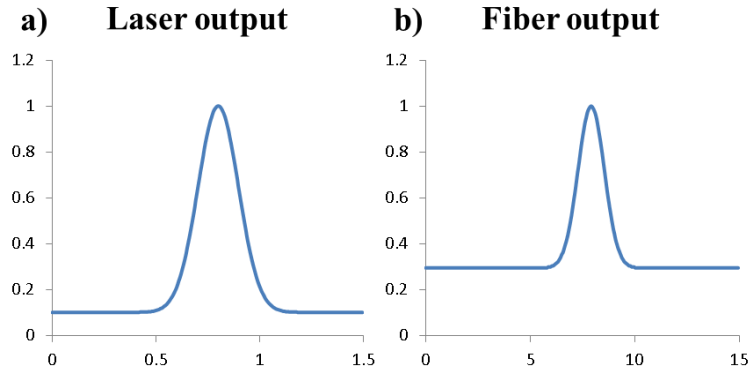
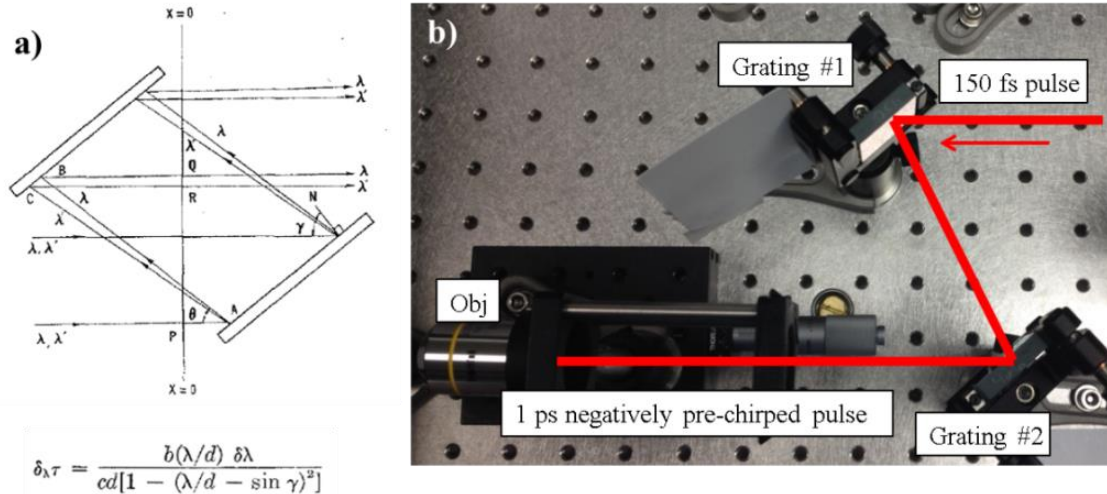


Fig. 2.4. Pulse stretching by the DCPCF. Autocorrelation traces of the laser pulse measured at a) the laser output and b) the fiber output, showing the pulse width is stretch from 150 fs to 1080 fs.

Since the built in prechirp unit in the laser unit is designed only to compensate the dispersion in the beam path of a microscope, it doesn't have sufficient range to compensate the positive chirp introduced by the fiber. An additional prechirp unit using a pair of gratings is inserted between the laser output and the fiber. The light reflected off the gratings has a wavelength dependent diffractive angle, resulting in difference path length between the two gratings. Long wavelength components travel a longer distance compared to shorter wavelength components, generating a negative chirp in the laser pulse, as shown in **Fig. 2.5a** [97]. The amount of chirp depends on parameters of the gratings, distance between the two gratings and spectral distribution of the incoming laser pulse.



$$\delta_{\lambda\tau} = \frac{b(\lambda/d) \delta\lambda}{cd[1 - (\lambda/d - \sin \gamma)^2]}$$

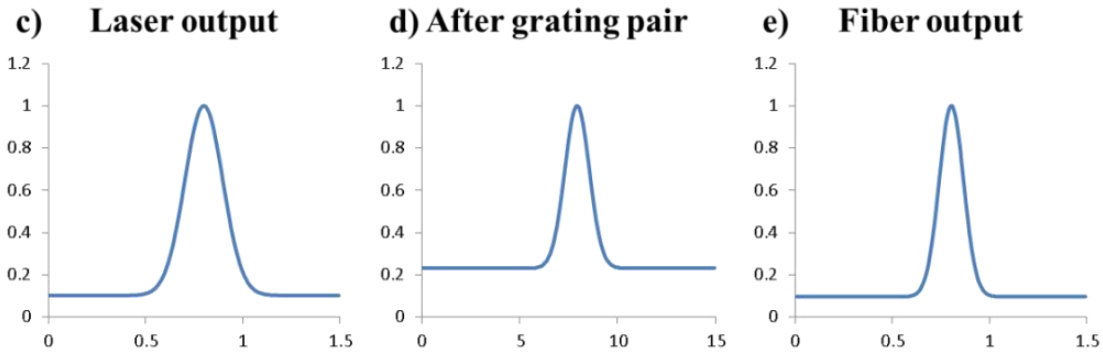


Fig. 2.5. Grating pair pulse compression. a) Working principle of a grating pair pulse compressor. Figure adapted from [97]. b) Grating pair inserted before the fiber for prechirp. Autocorrelation traces for the laser pulse c) at the laser output d) after the prechirp unit and e) at the fiber output, with pulse width of 150 fs, 1040 fs and 105 fs, respectively.

We used a pair of gratings with 600 groves/mm, a blaze angle of 13° and blaze wavelength of 750 nm. To compress a 1 ps laser pulse back to its minimum pulse width, we used the following parameters in our setup: $d^{-1} = 600$ lines/mm, $\lambda = 750$ nm, $\gamma = 45$ degrees, $\theta = 60$ degrees, $\delta\lambda = 10$ nm. For $b = 10$ cm, 1 ps pulse can be compressed to its minimal pulse width. The pulse width measurement for the laser beam before gratings, after gratings and after fiber output is shown below. We can see that by using the prechirp unit, the pulse width is compressed back to about 100 fs at the fiber output.

2.2.2.2 Hollow core photonic bandgap fiber

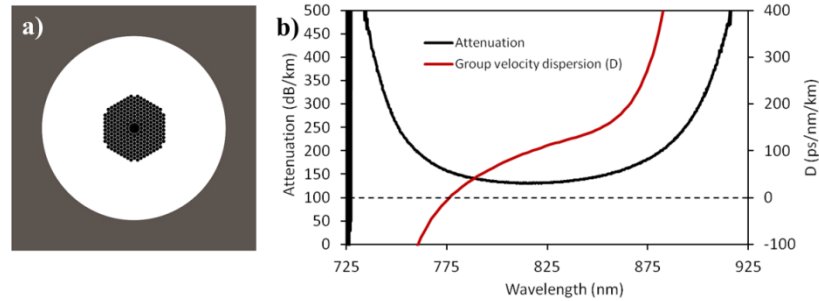


Fig. 2.6. Hollow core photonic bandgap fiber. a) Schematic of the cross-section, showing the air core surrounded by a microstructured cladding. b) Attenuation and dispersion parameter of this fiber. Figure adapted from NKT Photonics website.

A grating pair is still needed to pre-compensate the dispersion from the photonic crystal fiber, which reduces the laser throughput by about 50%. Furthermore, self-phase modulation was observed at increase laser power [105]. From our experiment we also observed broadened pulse width when increasing laser power. To address these issues, a hollow core photonic bandgap fiber has been developed earlier with a core surrounded by a microstructured cladding [106]. Using this fiber, light can be considered to be traveling in air, thus material dispersion is zero and the chromatic dispersion is dominated by waveguide dispersion. For our study, we chose a fiber (HC-800-02, NKT Photonics) with zero-dispersion wavelength at around 780 nm. The schematic of the fiber cross-section is shown in **Fig. 2.6a** and the dispersion parameter is shown in **Fig. 2.6b**.

2.3 MEMS based 2D scanner

Both confocal and multiphoton endomicroscopy rely on miniature actuators for high speed laser scanning. Our group has been working on 2D MEMS scanner based on

electrostatic actuation and the principle of parametric resonance, where large mechanical scan angles when operating in resonance [107] [108]. All the MEMS scanners used in this thesis are designed and fabricated by a MEMS expert in our group, Dr. Haijun Li. All the fabrication was done in the Lurie Nanofabrication Facility (LNF) of the University of Michigan. The first generation of the 2D MEMS mirror that we plan to integrate into the endomicroscope is shown in Fig. 2.7a. The mirror was designed with a 1.8 mm diameter circular reflector with overall chip size of 3x3 mm². A gimbal frame is used to minimize cross-talk between the X (inner) and Y (outer) axes. The mirror rotates in the XY plane using two orthogonal sets of electrostatic comb-drive actuators.

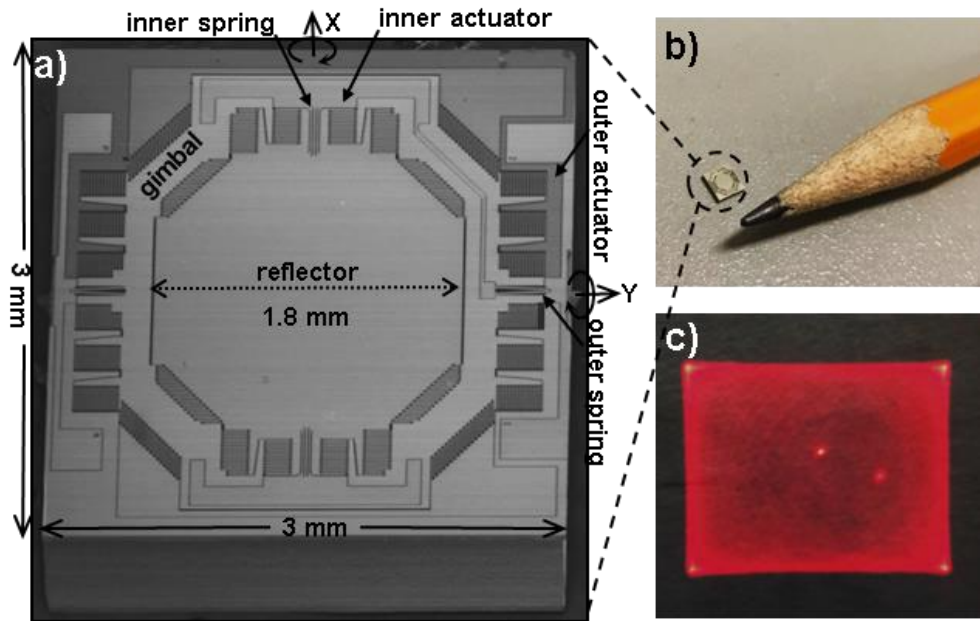


Fig. 2.7. First generation electrostatic MEMS scanner developed by our group. a) Schematic shows dimensions of the 2D MEMS scanner. Image courtesy of Dr. Haijun Li. b) Side comparison of a MEMS chip and a pencil tip. c) When both axes are actuated to scan a laser beam, a very dense 2D scan pattern can be visualized.

The scanner was fabricated using a 3 step deep reactive-ion etch (DRIE) process with 3 masks. Aluminum was sputtered on the front-side silicon surface to improve reflectivity. Both inner and outer axes operate in resonance with resonant frequencies of around 3 kHz and 1 kHz. To demonstrate the small size of the MEMS scanner, a device was put on the tip of a finger, as shown in Fig. 2.7b. To show that the MEMS scanner can be used form a dense 2D scan pattern for imaging, we shot a laser beam onto the mirror and actuated both axes at the corresponding driving frequencies. A very dense scan pattern can be visualized, Fig. 2.7c. The scan pattern can cover 400x400 pixels with 5 Hz repetition rate.

2.3.1 MEMS scanner characterization

In **Fig. 2.8**, an automatic MEMS testing platform was constructed to accurately measure the frequency response of MEMS scan mirrors. To measure the performance of a MEMS scanner with tilt motion, **Fig. 2.8a**, a laser beam with 1 mm beam diameter was directed to a beam splitter (BS004, Thorlabs). 50% of the light is reflected and travels to the MEMS mirror at a 90° incidence angle. The beam reflected by the MEMS mirror goes through the same beam splitter and hit the center of a position sensing detector (PSD) (PSM 2-10, On-Trak Photonics). When the MEMS mirror is actuated, the deflected beam will hit different positions on the PSD. We can calculate the optical scan angle from the beam location on the PSD and the distance from the MEMS scanner to the PSD. In this setup, the mechanical scan angle of the MEMS scanner will be half of the optical scan angle. For a MEMS mirror with out of plane axial motion, **Fig. 2.8b**, a high speed laser based

displacement sensor was used. As shown in **Fig. 2.8c**, a LabVIEW program is developed which sends out a frequency sweep to drive the MEMS scanner while reads the PSD or displacement sensor output at the same time, using a high-speed data acquisition board (DAQ) (PCI 6115, National Instruments). For each frequency, the scan angle is calculated and plotted against different frequencies.

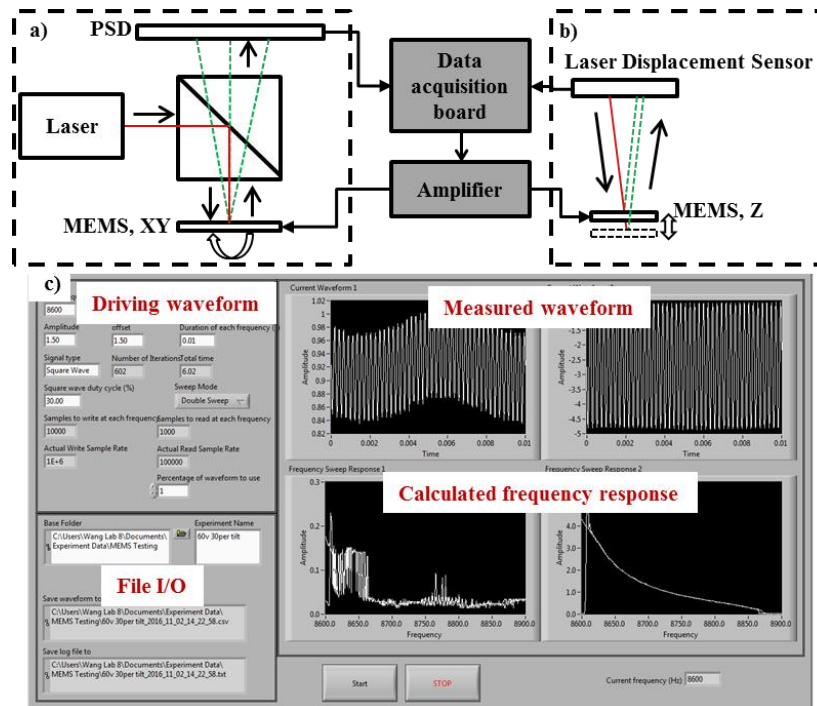


Fig. 2.8. Laser based MEMS testing platform. Optical setup for a) tilting angle and b) axial displacement measurement. c) LabVIEW program interface for automatic frequency response measurement.

2.3.2 2D scan pattern generation

For high speed 2D beam scanning, there are three types of commonly used scan patterns: raster scan, spiral scan and Lissajous scan. In raster scan, as shown in **Fig. 2.9a**, the rectangular FOV is divided into a sequence of scan lines and the beam sweeps

horizontally from left to right at a constant speed for each line. Then the beam rapidly moves back to the left and starts to scan the next line. The vertical position is also increasing at the same time at a much lower rate. A 2D scanner with one fast axis and one slow axis is needed, while the frame rate equals to the scanning frequency of the slow axis and the line scan rate equals to the frequency of the fast axis. For the case of spiral scan, **Fig. 2.9b**, beam is rotated out from the center and in a circular motion and covers a round FOV. Lissajous scan pattern is the most complex among the three, **Fig. 2.9c**. The shape and coverage of the pattern are determined by the ratio of frequencies of the two axes. Example scan patterns with maximum scan frequency of 20 Hz and 1 Hz repetition rate are shown in **Fig. 2.9a-c**.

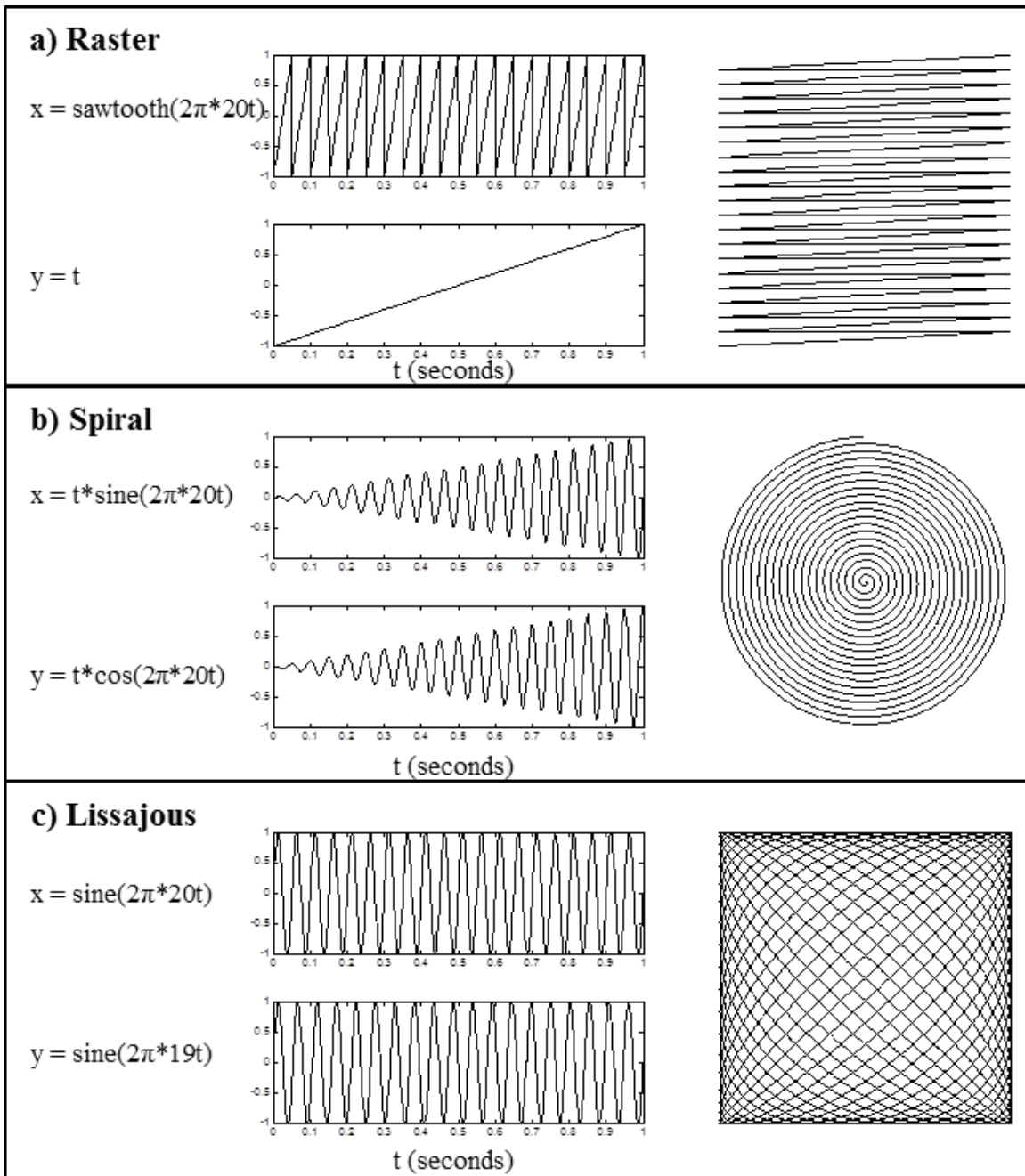


Fig. 2.9. Three commonly used scan patterns. a) Raster. b) Spiral. c) Lissajous.

2.3.3 Image reconstruction

Path distortions of the laser beam occur in any beam scanning system, whether it is a two-mirror configuration or a single mirror with two rotational degrees of freedom (DOF) [109]. In order to correctly reconstruct the image, it is important to characterize the distortion profile of the 2D MEMS scanner used in our system. The reflected beam path can be analytically calculated using reflection and rotation matrix transformations.

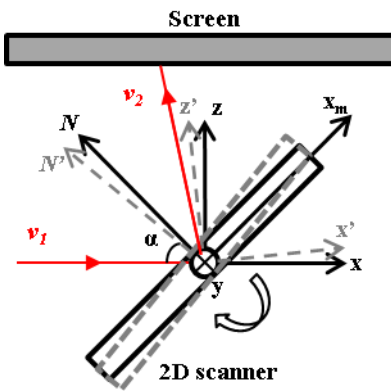


Fig. 2.10. Schematic of beam scanning with a 2D scanner.

As shown in **Fig. 2.10**, the incoming laser beam is denoted by \mathbf{v}_1 and the reflected beam is denoted by \mathbf{v}_2 . The world reference frame is given by $\mathbf{F} = (x, y, z)$. After the mirror rotates about its two axes x_m and y_m , the reference frame is given by $\mathbf{F}' = (x', y', z')$. The incoming beam \mathbf{v}_1 is represented as \mathbf{v}_1' in reference frame \mathbf{F}' , where \mathbf{v}_1' is given by:

$$\mathbf{v}_1' = (R_{x_m}(\theta_x)R_{y_m}(\theta_y))^{-1}\mathbf{v}_1 \quad (2.4)$$

$R_u(\theta)$ is the rotation matrix when a vector or a reference frame is rotated about an axis \mathbf{u} by angle θ , where $\mathbf{u} = [u_x, u_y, u_z]$. The rotation matrix is given by:

$$R_u(\theta) = \begin{bmatrix} \cos\theta + u_x^2(1 - \cos\theta) & u_x u_y(1 - \cos\theta) - u_z \sin\theta & u_x u_z(1 - \cos\theta) + u_y \sin\theta \\ u_y u_x(1 - \cos\theta) + u_z \sin\theta & \cos\theta + u_y^2(1 - \cos\theta) & u_y u_z(1 - \cos\theta) - u_x \sin\theta \\ u_z u_x(1 - \cos\theta) - u_y \sin\theta & u_z u_y(1 - \cos\theta) + u_x \sin\theta & \cos\theta + u_z^2(1 - \cos\theta) \end{bmatrix} \quad (2.5)$$

To reflect a vector \mathbf{v}_I through a plane defined by $ax + by + cz = 0$, the reflection matrix is given by

$$A_N = I - 2NN^T = \begin{bmatrix} 1 - 2a^2 & -2ab & -2ac \\ -2ab & 1 - 2b^2 & -2bc \\ -2ac & -2bc & 1 - 2c^2 \end{bmatrix} \quad (2.6)$$

Where $N = [a, b, c]$ is a unit vector normal to the plane. If the incidence angle of the beam onto the MEMS mirror is α , $N = [-\cos \alpha, 0, \sin \alpha]$. The reflected beam \mathbf{v}_2 can be calculated as follows:

$$\begin{aligned} \mathbf{v}_2 &= \left(R_{x_m}(\theta_x) R_{y_m}(\theta_y) \right) \mathbf{v}'_2 \\ &= \left(R_{x_m}(\theta_x) R_{y_m}(\theta_y) \right) (A_N \mathbf{v}'_1) \\ &= \left(R_{x_m}(\theta_x) R_{y_m}(\theta_y) \right) A_N \left(R_{x_m}(\theta_x) R_{y_m}(\theta_y) \right)^{-1} \mathbf{v}_1 \end{aligned} \quad (2.7)$$

To calculate scan pattern on the screen after the 2D scanner, a Matlab program is written which is included in the appendix. Here we show the distortion profiles from two different optical configurations: 45° and 90° incidence angles, as shown in **Fig. 2.11a** and **Fig. 2.11b**. The calculated distortion profiles are shown in **Fig. 2.11c** and **Fig. 2.11d**, when the MEMS mirror tilts $\pm 10^\circ$ in both axes. A severe distortion can be observed in **Fig. 2.11c** compared to **Fig. 2.11d**.

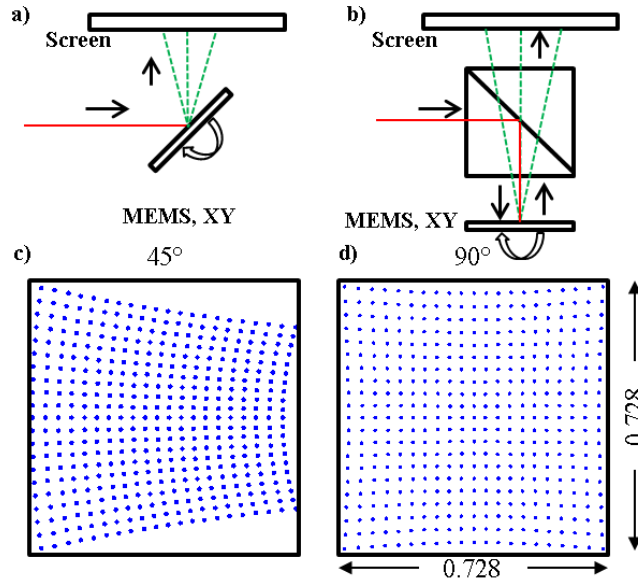


Fig. 2.11. Distortion profile of a 2D beam scanner. The scanner is orientated with incidence angles of a) 45 degrees and b) 90 degrees. Scan pattern on a screen for c) 45 degrees and d) 90 degrees incidence angles with mechanical scan angle of ± 10 degrees.

2.4 Optical system design

2.4.1 Numerical aperture

The numerical aperture (NA) is an important parameter of a microscopic imaging system because it is measure of its ability to resolve fine details and collect light. By Rayleigh's criterion [17], the lateral resolution of a confocal microscope is given by:

$$r_{xy} = \frac{0.44\lambda}{NA} \quad (2.8)$$

And the axial resolution is given by:

$$r_z = \frac{1.5n\lambda}{NA^2} \quad (2.9)$$

For multiphoton microscopy, NA also affects the efficiency of two photon absorption. When a fluorophore is illuminated by laser pulsed through a focusing lens, the probability that a fluorophore will undergo two-photon excitation is given by the following equation [110]:

$$n_a \propto \frac{\delta_2 P_{ave}^2}{\tau_p f_p^2} \left(\frac{NA^2}{2hc\lambda} \right)^2 \quad (2.10)$$

2.4.2 Beam scanning configurations

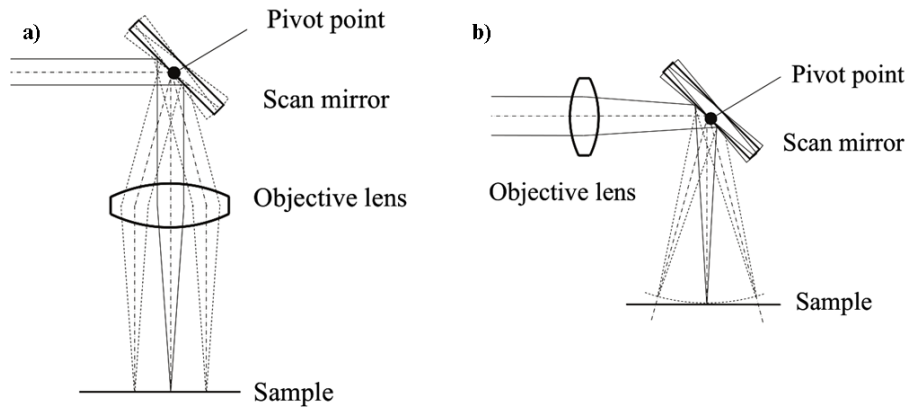


Fig. 2.12. Beam scanning configurations. a) Pre-objective scan. b) Post-objective scan. Figure adapted from [86].

For a pre-objective scan configuration, as shown in **Fig. 2.12a**, the scan mirror is placed before the objective lens. This is the most commonly used method, especially in commercial table-top microscopes. A high NA and a flat image field can be achieved. **Fig. 2.12b** shows a post-objective scan configuration, where the scanner is located between the objective and the imaging sample. A long working distance objective is needed and the

system will have lower NA. The imaging field is curved due to the scanning. The advantage of this approach is that the beam is always on axis with respect to the objective.

2.4.3 Scanner parameters and optical performance

Two important indicators of optical performance are the field of view (FOV) and the lateral resolution, r_{xy} . These two parameters can be combined into one performance metric: the maximum number of resolvable spots [111], N . This metric indicates how much information is contained inside the image. N is given by:

$$N = \frac{FOV_{xy}}{r_{xy}} \quad (2.11)$$

θ_{obj} is the scan angle entering the objective, and θ_{mirror} is the scan angle of the MEMS mirror. M is the magnification between the MEMS aperture and the objective aperture. D_{mirror} and D_{obj} are diameters of the mirror aperture and the objective. The FOV is given by:

$$FOV_{xy} = f\theta_{obj} = f \frac{\theta_{mirror}}{M} = f\theta_{mirror} \frac{D_{mirror}}{D_{obj}} \quad (2.12)$$

We also have the following:

$$NA = \frac{D_{obj}}{2f} \quad (2.13)$$

And from equation 2.4, we have:

$$N = \frac{\theta_{mirror} D_{mirror}}{0.44\lambda} \quad (2.14)$$

We show that the maximum number of resolvable spots only depends on the mirror diameter and the maximum tilting angle.

2.5 Data acquisition and image reconstruction

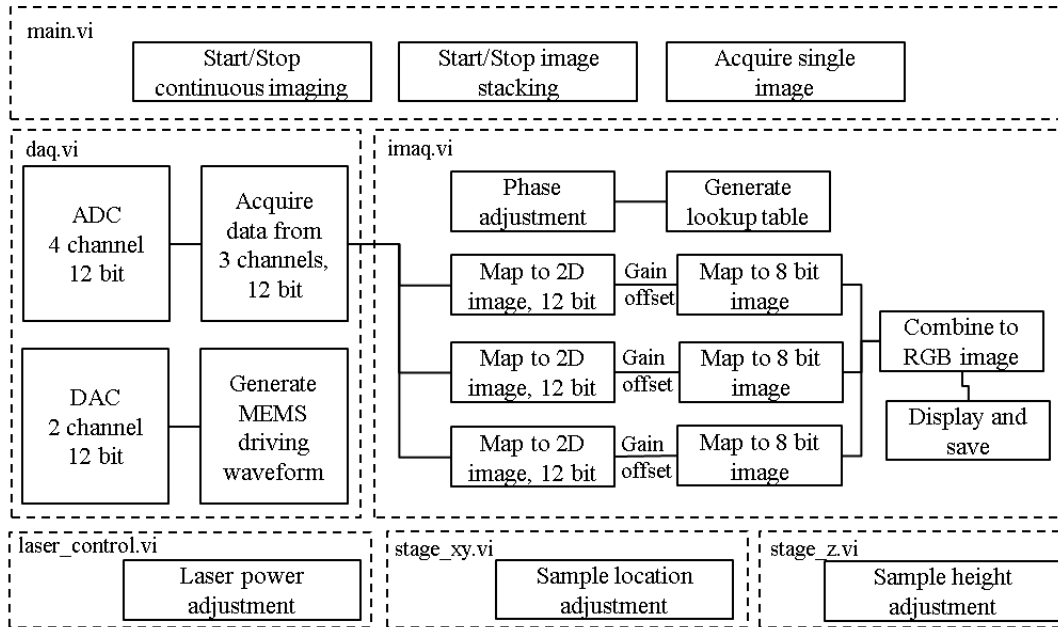


Fig. 2.13. LabVIEW program flow.

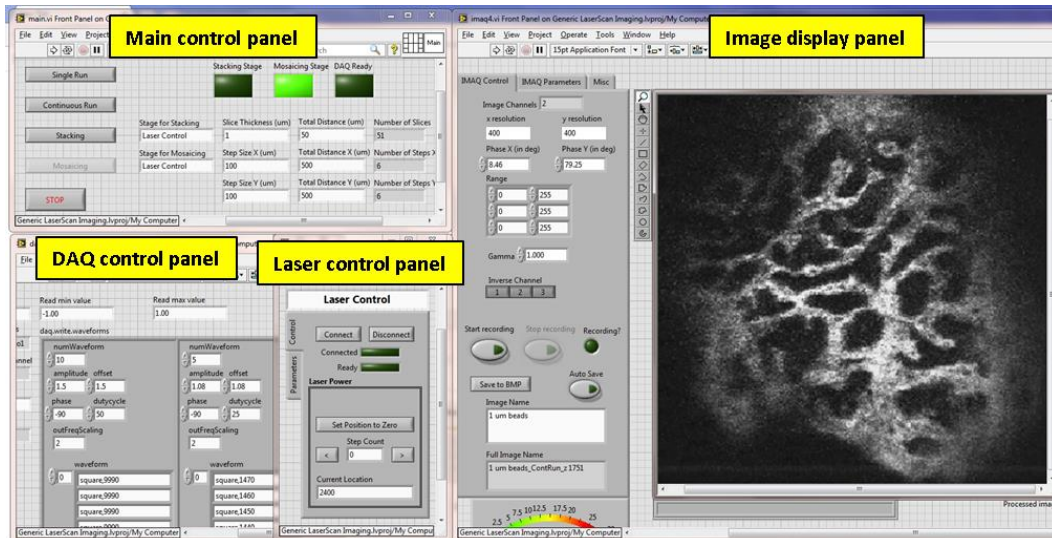


Fig. 2.14. LabVIEW program interface.

A LabVIEW program is developed to interface with the DAQ board for synchronized Lissajous scan pattern generation, data acquisition and real-time image

reconstruction. The program flow is shown in **Fig. 2.13**. The program interface is shown in **Fig. 2.14**. There are mainly four panels: main control, data acquisition (DAQ) control, image reconstruction and laser control. Details of the program is included in the appendix.

2.6 Design flow of an endomicroscope probe

Fig. 2.15 shows a typical design flow of a laser scanning endomicroscope probe based on a MEMS scanner. The contribution of the thesis is marked in red.

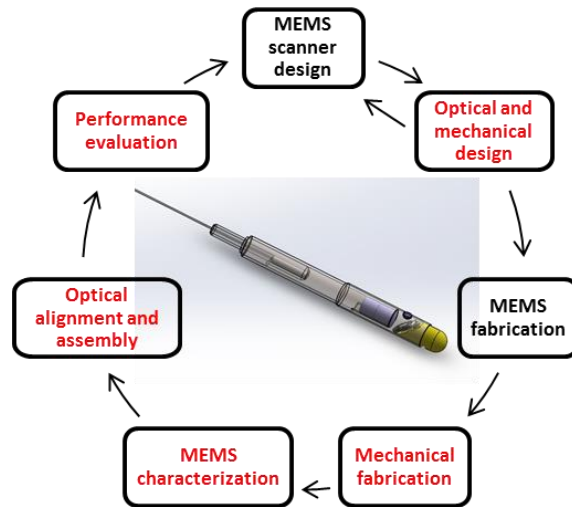


Fig. 2.15. Design flow of a MEMS based endomicroscope.

Chapter 3 Multiphoton endomicroscope

Part of this work has been published in [67].

3.1 Introduction

Improved imaging methods are needed to visualize the epithelium in genetically-engineered mouse models of human disease. This thin layer of tissue lines hollow organs, such as colon, and is the origin of a number of human cancers. Multiphoton microscopy is a powerful imaging tool for visualizing biological tissues with sub-cellular resolution and provides excellent depth, minimal photodamage, and reduced scattering [110]. Intravital microscopy is an emerging methodology for performing real time imaging in live animals. This technology is playing a greater role in the study of cellular and molecular biology because in vitro systems cannot adequately recapitulate the microenvironment of living tissues and systems. Conventional intravital microscopes use large, bulky objectives that require wide surgical exposure to image internal organs and result in terminal experiments [1]. If these instruments can be reduced sufficiently in size, biological phenomena can be observed in a longitudinal fashion without animal sacrifice.

A fast, compact scanner is needed to perform real time imaging with high performance in a miniature instrument. Previously, multiphoton endomicroscopes based

on fiber scanning have been demonstrated [43] [41] [42] [44]. This approach can introduce extra off-axis aberrations, and scanning performance is fiber dependent. Alternatively, beam scanning can be performed using tiny mirrors developed with microelectromechanical systems (MEMS) technology. MEMS scanners have been developed previously [112] [62] [113], but the overall size of the endomicroscope was not adequately small to perform repetitively imaging in mice. We aim to demonstrate a handheld multiphoton endomicroscope with a small distal diameter using a compact high speed MEMS scanner to perform repetitive imaging in the colon of a live mouse with “histology-like” performance.

3.2 Background

3.2.1 Two-photon microscopy

Two-photon microscopy is a powerful imaging tool for visualizing biological tissues with sub-cellular resolution and provides excellent depth, minimal photodamage, and reduced scattering [110].

Unlike traditional fluorescence microscopy which uses shorter wavelength for longer emission wavelength, two-photon microscopy uses longer wavelength for excitation. During the process of two-photon absorption, two photons with longer wavelength are absorbed simultaneously by the same molecule, resulting in the emission of a photon with shorter wavelength. In two-photon microscopy, near-infrared light can be used to excite

commonly available dyes with visible range emission, improving the penetration depth due to less scattering.

Two-photon microscopy has a similar optical architecture compare to confocal microscopy. Both techniques use galvo scanner for laser beam scanning, an objective for a tight focus and have capability of optical sectioning. Two-photon microscopy relies on the fact that two-absorption only occurs at the focal spot, while confocal microscopy uses a pinhole to reject out of focus fluorescence. In this sense, two-photon microscopy has less photo-toxicity for regions not at the focal spot. It's also easier to separate the excitation light from the emission since two-photon microscopy uses much longer wavelength, while confocal microscopy uses excitation wavelength close to emission wavelength.

3.3 Methods

3.3.1 2D MEMS scanner

3.3.1.1 Scanner design and fabrication

Our group has previously developed a 2D MEMS scanner based on the principle of parametric resonance, where large mechanical scan angles can be achieved by driving the structure at $2\omega_0/n$, where ω_0 is the natural frequency of the scanner structure and n is an integer ≥ 1 [107] [114] [108]. The mirror was designed with a 1.8 mm diameter circular reflector to accommodate the 1.2 mm width of the excitation beam at 45° incidence, **Fig. 3.1**. When scanning at large mechanical angles up to $\pm 4.5^\circ$, this mirror reflects $>95\%$ of the beam. A gimbal frame is used to minimize cross-talk between the X (inner) and Y

(outer) axes. Orthogonally oriented inner and outer electrostatic comb-drives actuators are coupled to torsional springs to rotate the mirror about either axis. In this design, the resonant frequencies of the inner and the outer axes were chosen to be ~ 1 and ~ 3 kHz, respectively, to image in vivo at ≥ 5 frame/sec using Lissajous scanning. Custom software was developed in LabView to drive the MEMS scanner and to reconstruct the image by remapping the time series signal to a 2D image using calibrated motion profiles from the scanner to generate a lookup table. The scanner was fabricated using a 3 step deep reactive-ion etch (DRIE) process with 3 masks [108]. Aluminum was sputtered on the front-side silicon surface to improve reflectivity. The mirror curvature and surface roughness were measured using an optical surface profiler (NewView 5000, Zygo).

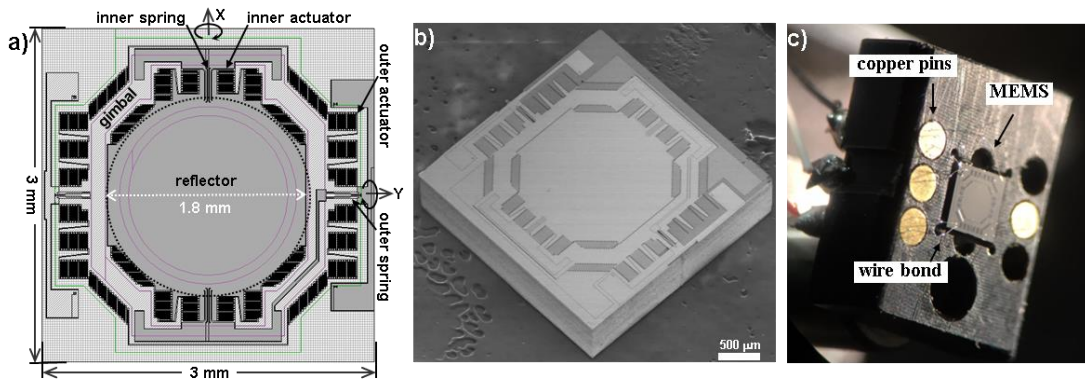


Fig. 3.1. 2D MEMS scanner. a) Schematic shows dimensions of the 2D MEMS scanner. b) SEM of fabricated scanner. c) MEMS scanner mounted onto a custom design fixture.

Fig. 3.1a shows a schematic of the 2D MEMS scanner. A 1.8 mm diameter reflector is supported by a gimbal frame on a chip with overall size of $3 \times 3 \text{ mm}^2$. The mirror rotates in the XY plane using two orthogonal sets of electrostatic comb-drive actuators. The mirror is coated with a ~ 50 nm layer of Al to achieve high reflectivity from 450-780

nm. We measured a reflectivity $> 80\%$ using a 488 and 780 nm laser. We did not increase the thickness of the coating because increased stress can deform the reflective surface and change the curvature of the MEMS mirror. We haven't observed any damage to the mirror from the laser after using this single MEMS mirror for our animal imaging experiments. We found the mirror surface to have a radius of curvature of ~ 1.7 meter and a root mean square (RMS) roughness of ~ 2 nm. **Fig. 3.1b** shows a scanning electron micrograph (SEM) of the fabricated scanner. In **Fig. 3.1c**, a custom designed fixture was fabricated using Delrin, a non-conductive material with high strength and stiffness. Copper pins were used as contacts for wire bonding the electrical connections.

3.3.1.2 MEMS scanner performance

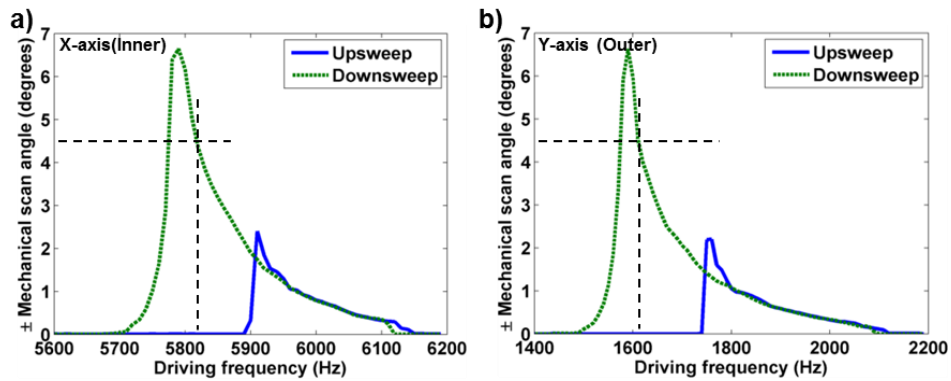


Fig. 3.2. MEMS scanner characterization. Frequency response shows mechanical scan angles of the c) inner and d) outer axes with drive voltage of 40 V_{pp} with either an upsweep (low-to-high) or downsweep (high-to-low) in frequency.

Fig. 3.2a and **Fig. 3.2b** shows the frequency response of the scanner to a sine-wave input at 40 V_{pp} for the X and Y axes, respectively. When sweeping from high-to-low frequency in a downsweep (green), we found a larger scan angle compared to sweeping

from low-to-high frequency in an up-sweep (blue). This phenomenon has been previously demonstrated with parametric resonance scanners [114] [108]. This device can achieve $\pm 4.5^\circ$ mechanical scan angle at $40 V_{pp}$ with a drive frequency close to $2\omega_0$ of 5.82 and 1.61 kHz for the X and Y axes, respectively, to produce images at 5 frames/sec with 400x400 pixels.

Applying these drive frequencies to our parametric resonance scanner, we achieved actual tilting frequencies of 2910 Hz and 805 Hz in the X and Y axes, respectively. This forms a dense Lissajous scan pattern which repeats itself at 5 Hz to encompass images with dimensions of 400x400 pixels with 100% coverage. Since there is a phase difference between the driving waveform and the actual mirror location, we need to find this phase information for image reconstruction. This process is done by imaging a standard target and manually iterating through different phases for both channels. The optimal phases are chosen when we can get a sharp image. The phase is adjusted manually during imaging with step size of 0.01 degrees. We identified these parameters using a custom Matlab program.

3.3.2 Optical design

We performed ray-trace simulations (ZEMAX, ver. 13) to identify commercially-available optics to achieve diffraction-limited resolution on axis, **Fig. 3.3**. We used achromats for L_3 and L_4 in a telescope configuration to expand the excitation beam to a width of 1.8 mm to fill the back aperture of the focusing optics L_5 and L_6 to maximize the effective numerical aperture (NA) and hence photon flux to generate the fluorescence

signal. **Fig. 3.3a** shows the ray tracing simulation of the optical design using Zemax. We identified commercially-available achromats with OD 3 mm for L_3 with $f = 6$ mm (45-089, Edmund Optics) and L_4 with $f = 9$ mm (45-090, Edmund Optics) to produce a telescope configuration. For focusing, we identified an aspheric lens L_5 with OD 3 mm and $f = 2$ mm (352150-B, Thorlabs) and a plano-convex lens L_6 with OD 2 mm and $f = 2$ mm (65-265, Edmund Optics). We measured a distance of 0.34 mm between L_5 and L_6 by using a reflectance image to bring a standard USAF target (R3L1S4N, Thorlabs) into focus. This optical configuration has an effective NA = 0.63 and a working distance of $Z = 60$ μm . At this depth, the nuclei in the epithelium of mouse colon can be visualized. We obtained a field-of-view (FOV) of 300×300 μm^2 with a lateral mechanical scan angle of $\pm 4.5^\circ$. Zemax simulation results for spot sizes are shown in **Fig. 3.3b-d**. A diffraction-limited spot size with radius $R = 0.33$ μm was found on the optical axis at $X=0$ μm that increased to $R = 2.17$ μm at $X=150$ μm , the lateral extent of the image FOV. With these optics, the frontal focus shifts <30 μm over the wavelength range 450-780 nm used to excite and collect fluorescence. The difference in focus between the excitation and fluorescence wavelengths has little effect on the coupling efficiency of our system because we use a separate, large multi-modal fiber for collection.

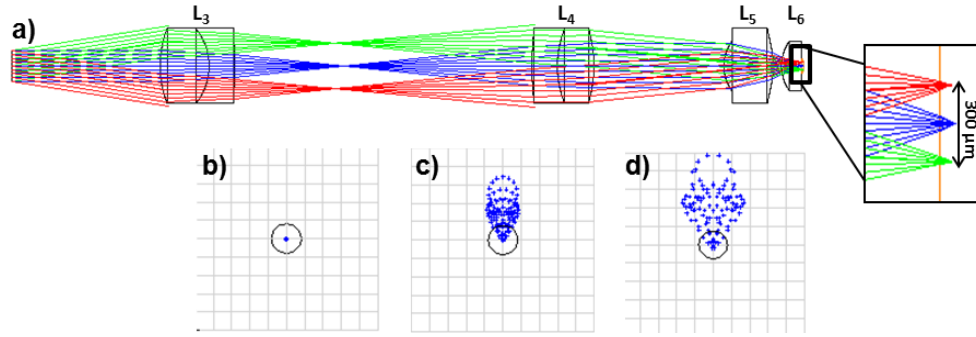


Fig. 3.3. Zemax Simulation. a) Ray-trace simulation for design of the distal optics (L₃-L₆). A field-of-view (FOV) of 300×300 μm² can be achieved with a lateral mechanical scan angle of ±4.5°. b), c), d) Spot size (RMS radius) of 0.33, 1.265 and 2.168 μm can be achieved at a distance of 0, 70 and 150 μm away from the center of the FOV.

3.3.3 System architecture

We used a Ti-Sapphire laser (Mai Tai DeepSee HP DS, Spectra-Physics) with a tunable spectral range of 700-1040 nm to deliver excitation (red arrows) with ~100 fs pulse width at 80 MHz, **Fig. 3.4**. The pulse duration was minimized using a dispersion pre-compensation unit located inside the laser housing. A half wave plate (HWP) and linear polarizer (LP) were used in combination to adjust the power. The beam is focused into a 1 meter long hollow core photonic bandgap fiber (PBF) with NA = 0.2 (HC-800-02, NKT Photonics) using a 10X objective lens L₁ with f = 18 mm (RMS 10X, Thorlabs). The PBF fiber transmits light at 780 nm with zero dispersion, thus prechirp was not performed. This fiber can achieve a bend diameter of <1 cm without loss of optical transmission. An aspheric lens L₂ with f = 3 mm (355660-B, Thorlabs) collimates the beam coming out of the fiber to a diameter of 1.2 mm. The beam is reflected by an aluminum (Al) coated mirror M₁ (48-405, Edmund Optics), and passes through a dichroic mirror M₂ (62-634, Edmund Optics) with transmission efficiency >95% at 780 nm onto a custom 2D MEMS scanner

M_3 at 45° incidence. The distal optics consists of four miniature lenses L_3 - L_6 that focus the excitation beam into the tissue and collect the fluorescence generated.

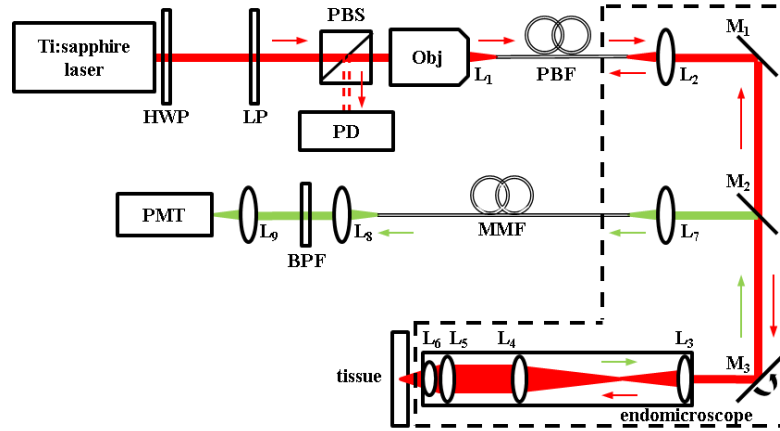


Fig. 3.4. Schematic. Handheld multiphoton endomicroscope shown in dashed box. Details provided in text.

Fluorescence (green arrows) travels in the opposite direction along the same optical path, is descanned by M_3 , is reflected by M_2 with reflectivity $>90\%$ from 425–650 nm, and is focused by lens L_7 with $f = 3$ mm (355660-B, Thorlabs) into a 1 meter long multimode fiber (MMF) (FT400UMT, Thorlabs) with a large core size of 400 μm to maximize light collection. Fluorescence is collimated by L_8 with $f = 15$ mm (LA1540-A, Thorlabs), passes through a band pass filter (BPF) (FGB39, Thorlabs) that transmits from 360-580 nm with $\sim 80\%$ transmission efficiency, and is focused by lens L_9 with $f = 60$ mm (LA1134-B, Thorlabs) onto a photomultiplier tube (PMT) detector (H7422-40, Hamamatsu). The PMT signal is amplified by a high-speed current amplifier (59-178, Edmund Optics). Reflectance that passes through M_2 is reflected by M_1 and focused back into the PBF for delivery to a photo diode (PD) detector (2051-FC, Newport).

For laser excitation, the transmission efficiency from the input of the PBF to the output of the endomicroscope at L_6 is ~20%. The PBF has ~50% transmission through the 1 meter length, and the MEMS mirror provides ~70% reflection, which includes a slight overfilling of the mirror and insertion losses from the optics. For fluorescence collection, the transmission efficiency from distal end of the endomicroscope at L_6 back to the PMT is ~50%, resulting from ~70% reflection at the MEMS mirror, ~95% transmission through the multimode fiber (MMF), and ~80% transmission efficiency of the bandpass filter (BPF) before the PMT.

We used a high-speed multi-function data acquisition board (National Instruments, PCI-6115) to digitize the fluorescence signal from the PMT and the reflectance signal from the photodiode. The same board was used to generate control signals to drive the 2D MEMS scanner. The data acquisition board was controlled by a pc running custom developed Labview programs.

3.3.4 Mechanical design and packaging

We used CAD software (Solidworks, ver 2013) to design the housing to package the optics and scanner, **Fig. 3.5a**. We used an uncoated stainless steel tube with an outer diameter (OD) of 3.4 mm and an inner diameter (ID) of 3 mm to center and align the distal focusing optics. The MEMS scanner was then mounted onto a 3-axis linear stage to align the optics, which was then fixed in place with epoxy (G14250, Thorlabs). Fig. 4a shows a CAD drawing of the mechanical package used for the handheld multiphoton endomicroscope. **Fig. 3.5a** shows the stainless steel tube with 3.4 mm diameter and 26

mm length used to align the distal focusing optics. **Fig. 3.5c** shows the instrument held by hand for in vivo imaging.

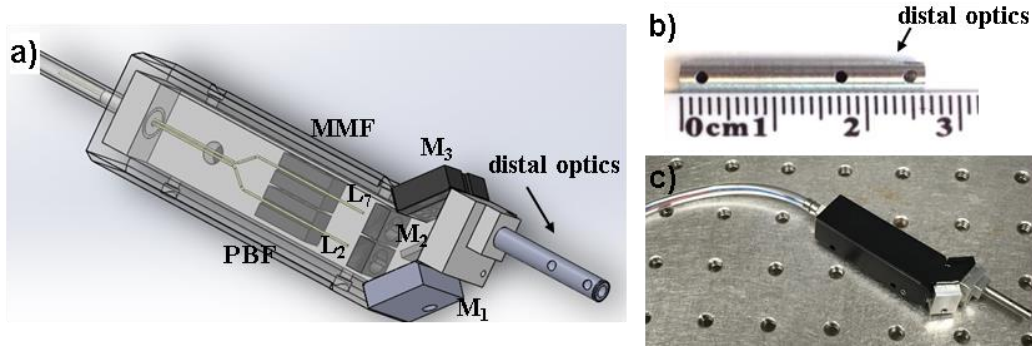


Fig. 3.5. Endomicroscope packaging. a) CAD drawing. b) Distal focusing optics. c) Handheld instrument can be used to perform repetitive imaging in small animal models of human disease. d) MEMS scanner.

3.3.5 System resolution

We used 100 nm diameter latex beads (F-8803, Life Technologies) to generate fluorescence for measuring the lateral and axial resolution of the imaging system. These dye-coated microspheres produce peak fluorescence emission at $\lambda_{em} = 515$ nm. The lateral resolution was measured from the horizontal fluorescence intensity profile across a single bead in the image, Fig. 5. The axial resolution was determined by scanning the beads in the axial direction using a translational stage. We aimed to achieve an image with a FOV of $300 \times 300 \mu\text{m}^2$ by sampling with 400×400 pixels. To satisfy the Nyquist theorem, we need at least 300×300 pixels to sample the FOV with lateral resolution of 2 μm .

3.3.6 Imaging of mouse colon

The study was approved by the Michigan University Committee on the Use and Care of Animals (UCUCA). We evaluated $n = 5$ *CPC;Apc* and $n = 5$ *Cdx Cre* mice. The *CPC;Apc* mice spontaneously develop colonic polyps in the distal colon that are accessible to the endomicroscope. These mice are genetically engineered to sporadically delete the APC gene, which is mutated in human disease [82]. The *Cdx Cre* mice do not develop polyps, and were used for imaging normal colonic mucosa. During imaging, the mice were anesthetized with inhaled isoflurane. We first used a small animal wide-field endoscope (27030BA, Karl Storz Veterinary Endoscopy) with white light illumination to exam the colon for presence of polyps. For use as landmarks, we measured 1) the distance between the endoscope tip and the anus and 2) the clockwise location of the polyp. Water was delivered through the instrument channel of the endoscope to remove stool, debris, and mucous. Hoechst 33342 (H1399, Life Technologies) at a dose of 10 mg/kg diluted in 200 μ L of PBS was delivered intravenously via a tail vein injection to stain the cell nuclei. After 30 min, the distal tip of the endomicroscope was placed in contact with the polyp. Images were collected at 5 frames/sec with a laser power of 50 mW exiting the probe. After completion of imaging, the mice were euthanized. The endomicroscope was oriented perpendicular to the specimen to optimize contact. Images were collected with the same power as that used in vivo. We used the previously identified landmarks to confirm the location of the polyp. The tissues were fixed in 10% buffered formalin and processed for

routine histology (H&E). We identified individual frames from the video streams with minimal motion artifacts.

3.4 Results

3.4.1 System resolution

Fig. 3.6a shows a reflectance image of a standard resolution target (USAF 1951) collected with the handheld multiphoton endomicroscope used to adjust the distance between L_5 and L_6 . The smallest set of bars (group 7, element 6) can be distinguished (dashed red oval), which represents a dimension of $\sim 2 \mu\text{m}$. **Fig. 3.6b** shows a representative fluorescence intensity profile from a 100 nm diameter bead (inset) plotted in the lateral dimension (blue line). The FWHM (full-width at half-maximum) of $\Delta X = 2.03 \mu\text{m}$ confirms the lateral resolution result. **Fig. 3.6c** shows a representative fluorescence intensity profile of a bead plotted in the axial dimension with FWHM of $\Delta Z = 9.02 \mu\text{m}$.

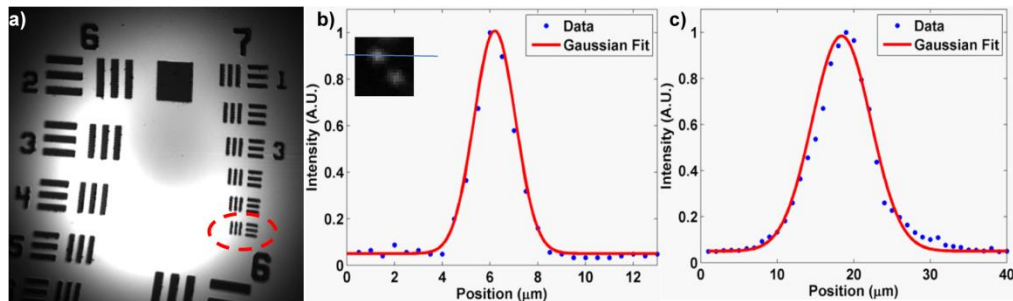


Fig. 3.6. Image resolution. a) Reflectance image of standard target (USAF 1951). Fluorescence intensity profiles of 100 nm beads show full-width at half maximum (FWHM) of b) $2.03 \mu\text{m}$ in lateral and c) $9.02 \mu\text{m}$ in axial directions.

3.4.2 Imaging of mouse colon

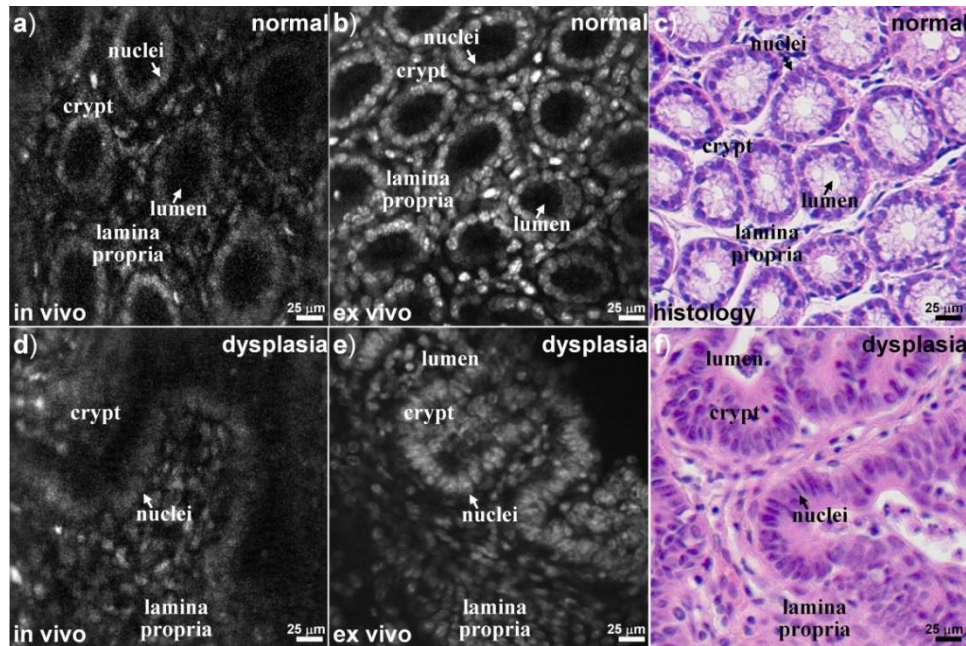


Fig. 3.7. Imaging results. a) Single frame from multiphoton excited fluorescence video (Media 1) of normal colonic mucosa collected in vivo at 5 frames/sec. b) Ex vivo image from normal averaged over 5 frames. c) Corresponding histology (H&E) of normal colon. Single frame from video of dysplastic crypts from colon of CPC;Apc mouse collected d) in vivo (Media 2) at 5 frames/sec and e) ex vivo (averaged over 5 frames). f) Corresponding histology (H&E) of dysplasia

We repetitively imaged the colon in live mice three days apart up to five times without any physical signs of trauma, including rectal bleeding, change in activity, and altered behavior. We could identify individual cell nuclei in crypt structures and in the lamina propria. **Fig. 3.7a** shows a representative image of normal mouse colon collected in vivo at 5 frames/sec. The nuclei (arrow) are circular in shape, and the crypts have an oval appearance with similar dimensions and a central lumen (arrow). **Fig. 3.7b** shows these features more clearly on an ex vivo image of normal averaged over 5 frames. Representative histology (H&E) is shown for normal, **Fig. 3.7c**. **Fig. 3.7d** shows a

representative image of dysplasia from a *CPC;Apc* mouse collected in vivo. The dysplastic nuclei (arrow) appear enlarged and elongated, and the dysplastic crypts are larger in size and distorted in shape. **Fig. 3.7e** shows these features more clearly on an ex vivo image of dysplasia averaged over 5 frames. Histology (H&E) is shown for dysplasia, **Fig. 3.7f**.

3.5 Discussion

Here, we present a handheld multiphoton endomicroscope with a 3.4 mm distal diameter that can be used to perform repetitive imaging in the colon of genetically-engineered mice. We used a high speed Al-coated MEMS scanner with large mirror surface to maximize the effective NA and photon flux to generate the fluorescence signal. We achieved a mechanical scan angle of ± 4.5 degrees at high frequencies with low drive voltages ($< 40 V_{pp}$) to produce a large FOV of $300 \times 300 \mu\text{m}^2$ at 5 frames/sec. Decoupling of the tilt motions between the inner and outer axes of the MEMS scanner allows for use of Lissajous scanning at high frame rates. The small distal diameter provides flexibility for use in intravital imaging compared with conventional microscopes that use bulk optics. We found this instrument to have stable operation with minimal interference from mechanical vibrations during in vivo imaging.

Imaging the epithelium of mouse colon with conventional optics and scanners increases experimental complexity and study invasiveness [115]. Surgery is often performed to improve exposure and immobilize organs using custom holders and stages, which can cause bleeding and tissue damage. Coverslips used to flatten and immobilize tissues can cause spherical aberrations. By reducing the distal diameter to 3.4 mm, we

achieved “histology-like” images in vivo that could distinguish between pre-malignant and normal colonic mucosa in a mouse model of colorectal cancer. This instrument can be broadly applied to a large number of sophisticated genetically-engineered mouse models of epithelial cancers. A miniature instrument can minimize the number of animals needed, better time the onset of disease, use each animal as its own control, and improve statistical rigor.

Previous multiphoton endomicroscopes have been demonstrated that using miniature scanning technologies. Fu et al reported a 5 mm diameter instrument with 10 μm axial resolution using a 2D mirror based on electrothermal actuation [62]. Fluorescence images were collected ex vivo from rat colon using raster scanning with individual frames collected at 7 lines per sec, a speed that is too slow for in vivo imaging. Hoy et al demonstrated a $10 \times 15 \times 40 \text{ mm}^3$ handheld instrument with 16.4 μm axial resolution using a 2D MEMS scanner based on electrostatic actuation [112]. Given the large size of this instrument, fluorescence images with a FOV of 310 μm were collected ex vivo from cells embedded in a collagen matrix using Lissajous scanning with individual frames averaged over 5 sec. By comparison, our MEMS scanner has a larger diameter (1.8 mm versus 500 μm) with comparable scan angle, resulting in a >3-fold larger number of resolvable focal spots [62]. Other multi-photon endomicroscopes have used GRIN lenses for focusing [116] [117]. These objectives are limited by chromatic aberration for fluorescence imaging. We used a compound lens because our MEMS mirror can achieve high reflectivity over a broad spectral range from 450 to 780 nm.

We used commercially-available lens to demonstrate this approach. Imaging performance can be improved in the future with custom optics. Chromatic aberrations can be reduced to increase fluorescence excitation and collection efficiency. A side rather than front viewing configuration can improve contact with the mucosal surface in hollow organs, such as colon. The MEMS scanner can be designed to perform raster scanning to improve the frame rate and reduce motion artifacts. As a future direction, we are incorporating the MEMS scanner into the distal end of the instrument to increase the length and to adjust the axial imaging depth using a remote fast scanning actuator [118].

3.6 Summary

We have developed a novel multiphoton endomicroscope that uses a fast MEMS scanner with 3.4 mm distal optics to perform repetitive in vivo imaging in mouse colon to distinguish between normal and dysplastic crypts. This instrument can be further developed for broad use as a general purpose intravital imaging instrument to perform longitudinal studies in genetically-engineered mouse models of human disease.

Chapter 4 Side-view multiphoton endomicroscope

4.1 Introduction

A front-viewing endomicroscope was demonstrated in the last chapter for in vivo imaging in the mouse colon. The instrument should be oriented perpendicular to the mucosal surface to achieve contact. However, there is very limited room for maneuver in hollow organs of small animals. From our previous experience of using the front-viewing probe for mouse colon imaging, we found that it is extremely challenging to maintain contact and acquire stable images. For hollow organ imaging, a side-viewing design is preferred over the previously developed front-viewing instrument. Therefore, in this chapter we explore the feasibility of developing a side-viewing probe based on the previously developed front-viewing instrument.

4.2 Methods

4.2.1 Side-view objective design

The most straightforward way to achieve a side-viewing imaging orientation is to add a reflective mirror at the end of the objective with 45° angle of incidence, such that the beam is reflected to the side, as shown in **Fig. 4.1a**. However, the required working distance of the objective lens L_3 will be very long such that the focused beam can reach out of the

probe even after the reflection. This approach has been demonstrated by Yun's group that a tabletop system was developed with a long GRIN lens and a reflective prism [119]. However, because of the size limitation of the probe, the long working distance objective will have a low NA (≤ 0.4), which will affect the efficiency of two photon excitation. Another optical configuration is shown in **Fig. 4.1b**, in which the collimated beam is reflected by the 45° mirror first and then focused by the objective lens L_3 . This approach will significantly increase the diameter of the probe. Chen's group used this approach to develop a probe with outer diameter of 10 mm [120]. Here we propose a new configuration, as shown in **Fig. 4.1c**. The beam is focused by a long working distance objective L_3 , reflected by the mirror and focused by another lens L_4 . Therefore, a higher NA can be achieved at the sample plane. When designing this side-view lens and mirror combination, **Fig. 4.1d**, it can be reduced to a two-lens configuration in **Fig. 4.1e**. The working distance of L_3 will need to be larger than 2.7 mm.

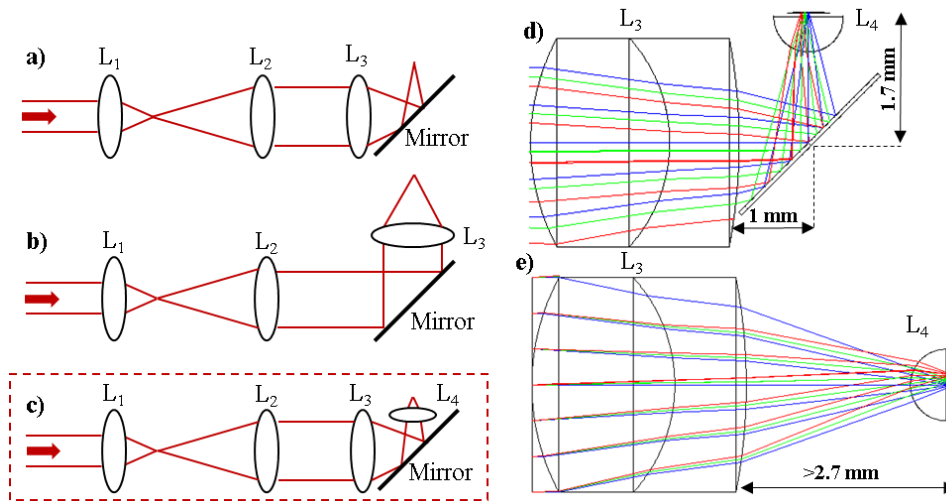


Fig. 4.1. Side-view optical configurations. a-c) Three different optical designs for side-view configuration. d-e) Side-view objective design.

We performed Zemax simulations to identify two potential designs to realize the side-view optical configuration. The design criteria are as follows: imaging $NA \geq 0.5$, working distance $\geq 80 \mu\text{m}$ and $FOV \geq 200 \times 200 \mu\text{m}^2$.

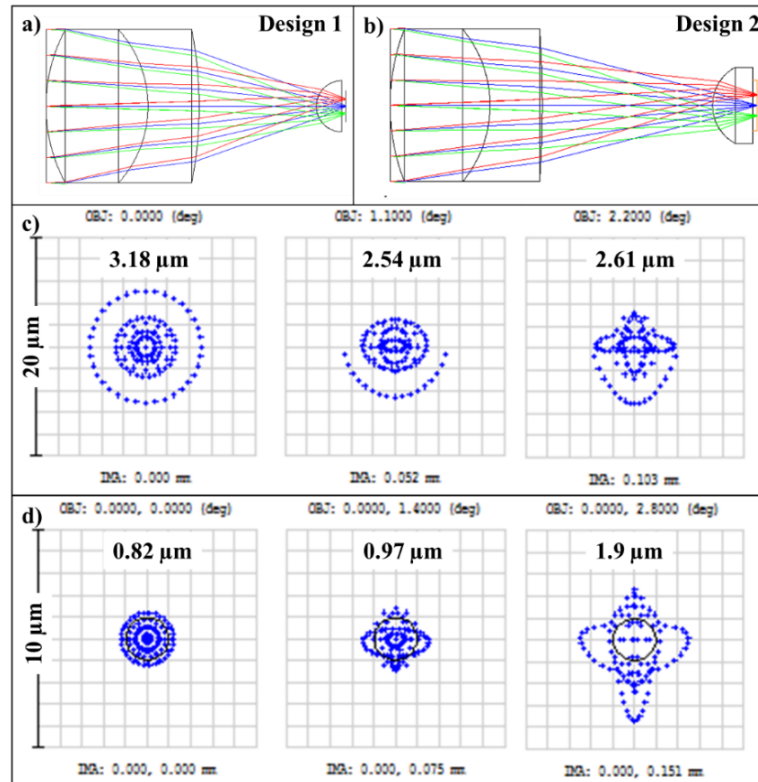


Fig. 4.2. Zemax simulation of two side-view objective designs. a, b) Ray-trace simulation for design 1 and design 2 of the side-view focusing optics (L_3 and L_4). c) RMS spot size of design 1 at 0, 50 and 100 μm away from the center of the FOV are 3.18, 2.54 and 2.61 μm . d) RMS spot size of design 2 at 0, 75 and 150 μm away from the center of the FOV are 0.82, 0.97 and 1.9 μm .

Design 1 is shown in **Fig. 4.2a**, where L_3 is an achromatic doublet with a working distance of 3 mm ($f = 4.5 \text{ mm}$, $NA = 0.33$, $OD = 3\text{mm}$, #47-721, Edmund Optics) and L_4 is a half ball lens ($f = 0.6 \text{ mm}$, $NA = 0.9$, $OD = 1\text{mm}$, #49-568, Edmund Optics). An FOV of $200 \times 200 \mu\text{m}^2$ can be achieved with a field angle 2.2° before L_3 . RMS spot sizes at 0, 50 and 100 μm away from the center of the FOV are 3.18, 2.54 and 2.61 μm , **Fig. 4.2c**.

Design 2 is shown in **Fig. 4.2b**, where L_3 is also an achromatic doublet with a working distance of 4.33 mm ($f = 6$ mm, $NA = 0.25$, $OD = 3$ mm, #45-089, Edmund Optics) and L_4 is a plano-convex lens ($f = 1$ mm, $NA = 0.75$, $OD = 1.5$ mm, #65-261, Edmund Optics). An FOV of $300 \times 300 \mu\text{m}^2$ can be achieved with a field angle 2.8° entering L_3 . RMS spot sizes at 0, 50 and 100 μm away from the center of the FOV are 0.82, 0.97 and 1.9 μm , **Fig. 4.2c**.

A comparison of the two designs is given in Table 4.1. Design 2 has slightly lower NA than design 1, but there is a larger FOV and much less aberration. The following discussion will be focused on the second design. The point spread function (PSF) at each field angle is shown in **Fig. 4.3**.

Table 4.1. Performance comparison of two optical designs

	Design 1	Design 2
NA	0.55	0.5
FOV (μm^2)	200 x 200	300 x 300
Working distance (μm)	100	100
Spot sizes (μm)	3.18 @0 μm	0.82 @0 μm
	2.54 @50 μm	0.97 @75 μm
	2.61 @100 μm	1.9 @150 μm

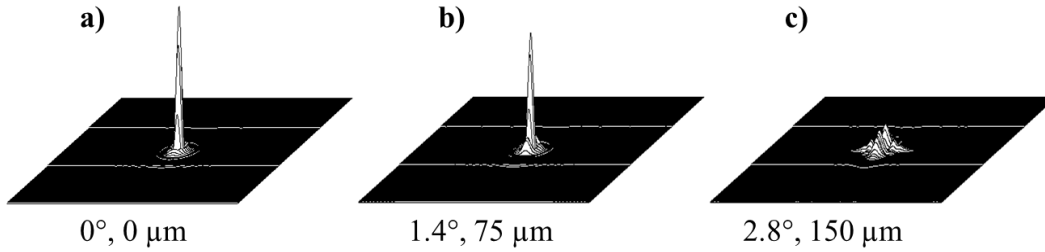


Fig. 4.3. PSFs of the two-lens objective. a-c) PSFs at field angles of 0° , 1.4° , 2.8° with focal spot location at 0, 75 and 150 μm away from center of FOV. PSFs are calculated using the Huygens diffraction integral.

4.2.2 Optical design of the distal probe

The distal optics consists of four miniature lenses L_1 - L_4 and a reflective mirror M that reflects the beam to the side into the tissue, **Fig. 4.4**. We identified commercially-available achromats with OD 3 mm for L_1 with $f = 4.5$ mm (47-721, Edmund Optics) and L_4 with $f = 12$ mm (63-692, Edmund Optics) to produce a telescope configuration. The beam is expanded to 3.2 mm to slightly overfill L_3 (45-089, Edmund Optics). The focused beam is reflected by a 45° rod mirror with OD 3 mm (54-094, Edmund Optics) onto a plano-convex lens L_4 (65-261, Edmund Optics). This optical configuration has an effective NA of 0.5 and a working distance of 100 μm . We obtained a field-of-view (FOV) of $300 \times 300 \mu\text{m}^2$ with a lateral mechanical scan angle of $\pm 3.7^\circ$.

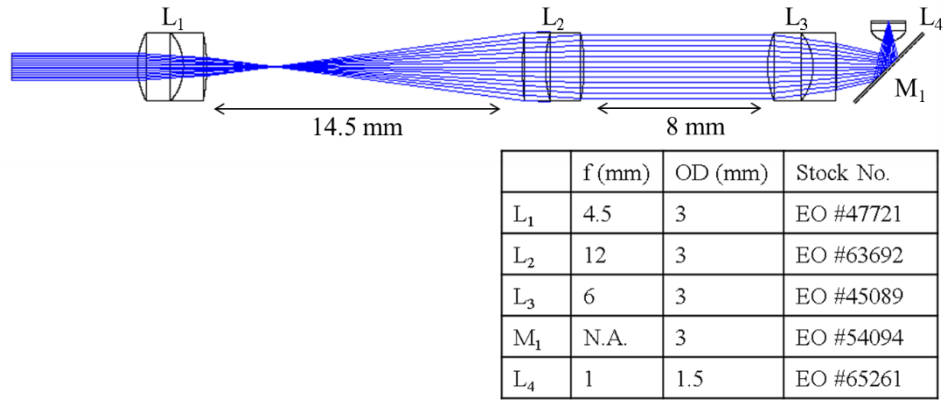


Fig. 4.4. Optical design and lens selection for the distal probe.

4.2.3 Mechanical design and packaging of side-view probe

We used CAD software (Solidworks, ver 2013) to design the housing to package the optics, **Fig. 4.5a,b**. There are mainly three mechanical parts housing the optics: relay and focusing lens (L₁₋₃) holder, distal lens (L₄) holder and rod mirror (M₁) holder. Using this design, the distance between L₃ and L₄ can be controlled to adjust the working distance out of L₄. Also, the M₁ can be rotated and translated to control the direction of the reflected beam. We used a stainless-steel tube with an outer diameter (OD) of 3.4 mm and an inner diameter (ID) of 3 mm to fabricate the holders for L₁₋₃ and M₁, **Fig. 4.5c,e**. L₁ and L₂ were installed into the tube first and the spacing was adjusted to create a collimate beam after the telescope. Then L₃ was installed at the end. Optics were fixed in position using a UV epoxy (NOA61, Norland Products). A stainless-steel tube with an outer diameter (OD) of 3.8 mm and an inner diameter (ID) of 3.4 mm was used to fabricate the distal lens holder which also connects the other two tubes, **Fig. 4.5d**. The alignment fixture can be screwed onto the mirror holder, and the other end can be fixed on a 5-DOF precision stage for

alignment. The location of the rod mirror has to be adjusted such that the reflected beam is aligned with the optical axis of L_4 , **Fig. 4.5f**. After alignment, a circular diverging beam at the exit of L_4 is shown in **Fig. 4.5g**.

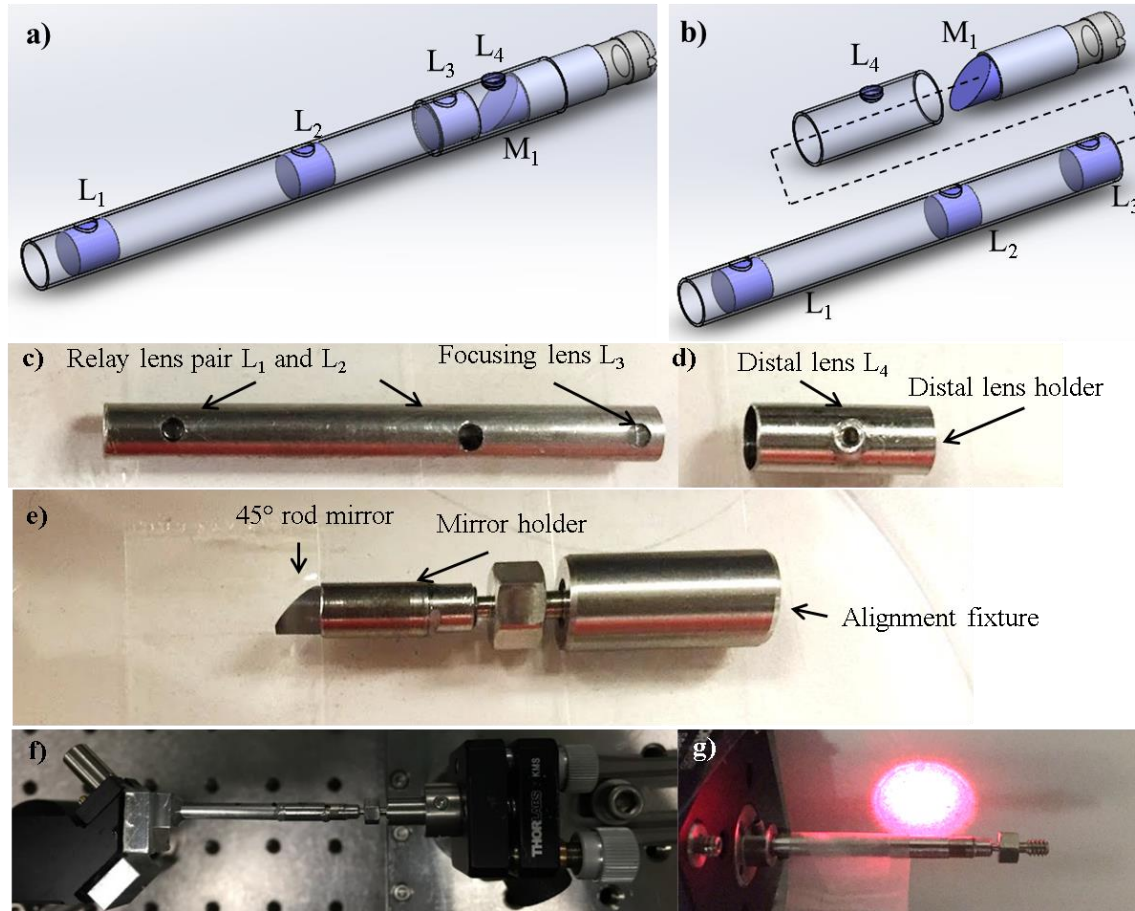


Fig. 4.5. Distal probe design and packaging. a) CAD drawing of the probe assembly and b) the exploded view. c) Fabricated stainless tube for relay lens pair and focusing lens. d) Distal lens holder. e) Rod mirror holder and alignment fixture. f) Alignment of the rod mirror using a 2DOF rotational stage and a 3DOF translational stage. g) Beam profile after alignment.

4.2.4 Mechanical design and packaging of the handheld instrument

The complete CAD design of the handheld side-view probe is shown in **Fig. 4.6a**.

The distal probe is mounted onto the same handheld part presented in chapter 3. Assembled

instrument is shown in **Fig. 4.6b**. In order to control the imaging location in vivo in the mouse colon, the probe is mounted onto a rotational (488, Newport) and translational stage (562F-XYZ, Newport) such that it can navigate easily in the mouse colon, **Fig. 4.6c**. The optical axis of the distal probe is aligned with the axis of rotation for the rotational stage.

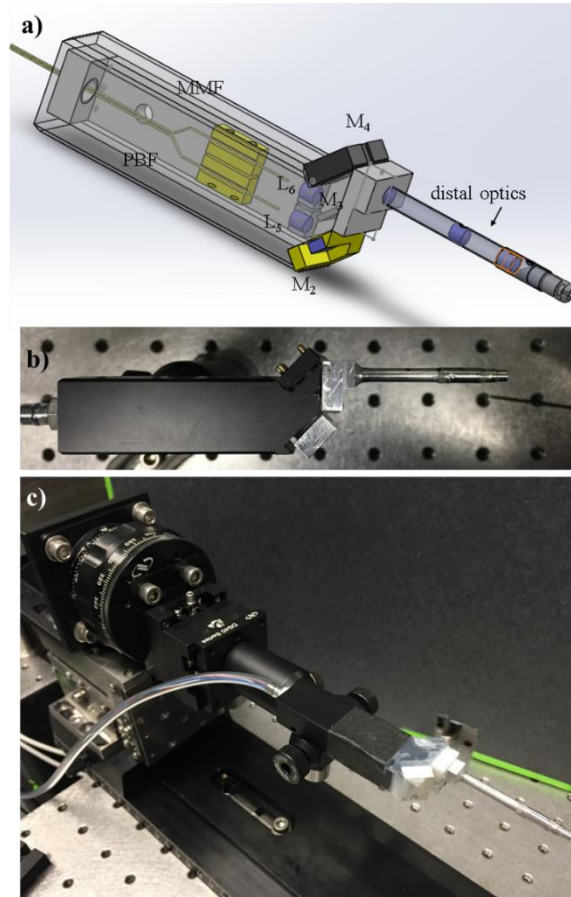


Fig. 4.6. Handheld probe mechanical design and packaging. a) Solidworks design of the probe. b) Assembled probe. c) Probe mounted onto a rotational and translational stage such that it can navigate in the mouse colon.

4.2.5 Ex vivo imaging of mouse colon tissue

The *CPC;Apc* mice spontaneously develop colonic polyps in the distal colon that are accessible to the endomicroscope. For ex vivo tissue imaging, the mouse was

ethanized and the colon tissue was harvested. The tissue was stained with Hoechst 33342 (H1399, Life Technologies) for 5 min and washed by PBS. Then the side of the distal probe was placed in contact with the tissue. Images were collected at 5 frames/sec with a laser power of 30 mW on the mucosa. During imaging, we used the translational stage to move the probe along the colon tissue such that a mosaic image can be acquired.

4.2.6 In vivo imaging

The study was approved by the Michigan University Committee on the Use and Care of Animals (UCUCA). During imaging, the mouse was anesthetized with inhaled isoflurane. We first used a small animal wide-field endoscope (27030BA, Karl Storz Veterinary Endoscopy) with white light illumination to exam the colon for presence of polyps. Hoechst 33342 (H1399, Life Technologies) at a dose of 10 mg/kg diluted in 200 μ L of PBS was delivered intravenously via a tail vein injection to stain the cell nuclei. After 30 min, the endomicroscope probe was placed inside the distal colon and L₄ can be in direct contact with the side walls. Images were collected at 5 frames/sec with a laser power of 50 mW on the mucosa.

4.3 Results

4.3.1 System resolution

Fig. 4.7 shows a reflectance image of a standard resolution target (USAF 1951) collected with the side-view multiphoton endomicroscope. The smallest set of bars (group

7, element 6) can be distinguished (dashed red oval), which represents a dimension of ~2 μm .

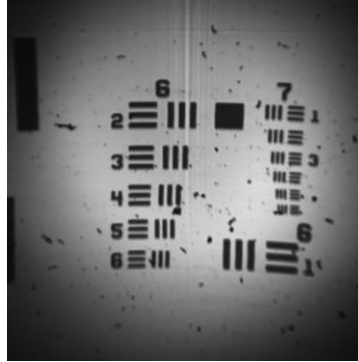


Fig. 4.7. Image resolution. Reflectance image of standard target (USAF 1951).

4.3.2 Lens paper imaging

Lens paper stained with DEAC and added green fluorescent beads, **Fig. 4.8.**

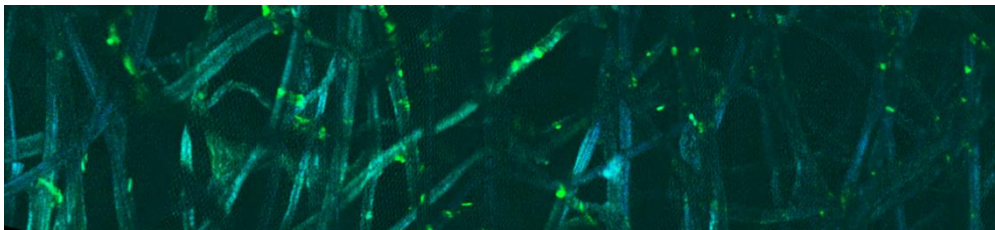


Fig. 4.8. Lens paper imaging. Mosaiced image created by moving the probe along the dye stained lens paper

4.3.3 Ex vivo imaging of mouse colon tissue

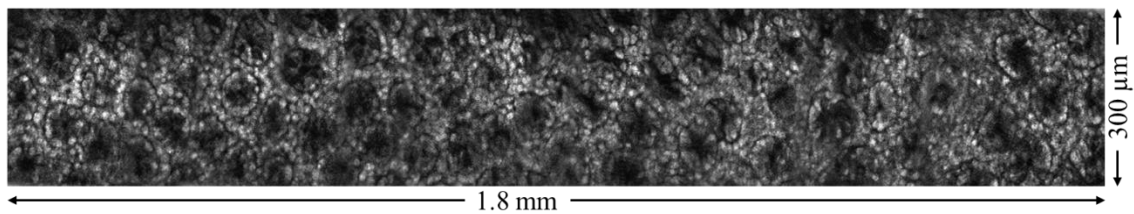


Fig. 4.9. Ex vivo imaging of mouse colon tissue. Mosaiced image created by moving the probe along the mouse colon sample

4.3.4 In vivo imaging of mouse colon

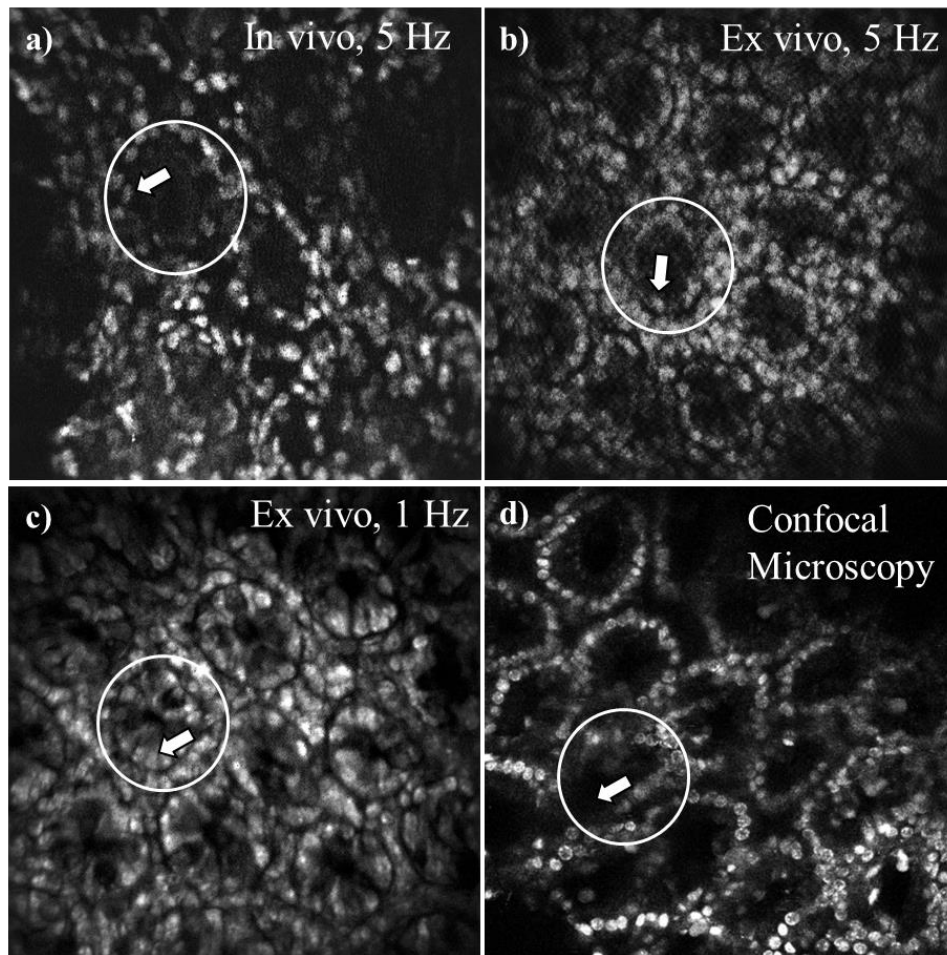


Fig. 4.10. In vivo and ex vivo imaging of mouse colon. a) In vivo image collected inside the mouse colon with 5 Hz frame rate. b) Ex vivo image collected from excised colon tissue with 5 Hz frame rate. c) 5-frame average of ex vivo images. d) Image of the same tissue collected using a commercial confocal microscope.

We could identify individual cell nuclei in crypt structures and in the lamina propria.

Fig. 4.10a shows a representative image of normal mouse colon collected in vivo at 5 frames/sec. The nuclei (arrow) are circular in shape, and the crypts have an oval

appearance with similar dimensions and a central lumen (circle). **Fig. 4.10b** shows a representative image mouse tissue collected ex vivo with 5 Hz frames/sec. **Fig. 4.10c** shows a 5-frame average of the ex vivo images. The same tissue was imaged under a commercial confocal microscope, as shown in **Fig. 4.10d**. These images show that our instrument can be used to collect in vivo and ex vivo images with similar performance of a commercial confocal microscope.

4.4 Discussion

Here, based on the instrument presented in chapter 3, we developed a side-view multiphoton endomicroscope with a 3.8 mm distal diameter that can be used to image the hollow organs of small animals. We used a mechanical scan angle of ± 4 degrees at high frequencies with low drive voltages ($< 40 V_{pp}$) to produce a large FOV of $300 \times 300 \mu\text{m}^2$ at 5 frames/sec. Compared to the front-viewing probe previously developed, this side-viewing architecture made it much easier to create stable imaging in the mouse colon because the distal lens is in direct contact with the side walls. We also found that it is much easier to pinpoint to different locations in the colon with the use of the rotational and translational mechanisms.

Previous side-view multiphoton endomicroscopes have been demonstrated in a tabletop setup where a long GRIN lens was used [121]. Here we used a MEMS scanner and miniature lenses to demonstrate a handheld endomicroscope with better optical performance. However, due to the use of commercially available optics, aberration is not corrected when the MEMS scans in large angles. Also, the numerical aperture is limited by

the choice of optical components, which affects two photon excitation efficiency. Imaging performance can be improved in the future with custom optics.

4.5 Summary

We have developed a novel side-view multiphoton endomicroscope that uses a 3.8 mm distal probe to perform repetitive in vivo imaging in mouse colon.

Chapter 5 Side-view confocal endomicroscope

5.1 Introduction

In last chapter we reported a side-view multiphoton probe for in vivo imaging in the mouse colon. The beam was scanned by a 2D MEMS actuator, expanded a telescope, and focused by the side-viewing optics. This is called pre-objective scan in which the beam scanner is placed before the imaging objective. This architecture is used in most laser scanning microscopes. Another type of scanning architecture is called post-objective scan where the scanner is placed after the objective. This allows for much larger scan angle and places lower requirement for the objective since incoming beam is always on-axis. But the imaging field will be curved and a longer working distance objective is needed. Based on our previous design, we can change the rod mirror to a MEMS scanner and then we are performing post-objective scan. The advantage of this design is that we can develop an ultra-compact endomicroscope probe, without handheld part. This allows for the use of the probe not only in small animals but also in human. Also, we will expect to have improved resolution and field of view. However, there will be a lot of technical challenges in integrating the scanner into the distal tip of the probe. In this chapter, we demonstrate the development process and imaging performance of a side-view confocal endomicroscope.

Confocal endomicroscopy is an emerging technology that can be used to collect high resolution images in vivo. [52] Front-viewing instruments are currently being used in the clinic to provide instantaneous “optical biopsies” with histology-like quality. [52] [27] They are oriented perpendicular to the mucosal surface to achieve contact. However, some clinical applications, such as imaging in the biliary and pancreatic duct, and hollow organs of small animals, have limited room for maneuver. From our previous experience of using a front-viewing multiphoton probe for mouse colon imaging, we found that it is challenging to maintain contact and pinpoint different locations. Therefore, a side-viewing design will be useful for these applications.

For real time imaging with high performance, a fast, compact scanner that can be packaged into a miniature instrument is needed. We have previously developed a 2D MEMS scanner to performs resonant scanning in orthogonal axes in a front-view endomicroscope. [67] We have now modified the mirror geometry to achieve a reduced chip dimensions to accommodate the limited space in a side viewing optical design and a higher resonant frequency for faster imaging speed.

Contrast agents that are specific for overexpressed molecular targets can help define biological activity in cancer. Peptides are promising for systemic use because they are small in size and low in molecular weight, thus have improved pharmacokinetic properties for imaging compared with bulky monoclonal antibodies. [122] Advantages include greater extravasation from leaky tumor vasculature, enhanced tissue diffusion, and deeper tumor penetration. [123] Peptides clear more rapidly from non-target tissues for reduced

background. [124] We have previously demonstrated a peptide specific for EGFR that was used to collect wide field fluorescence images of pre-malignant mucosa in mouse colon. [75] To demonstrate one of the use cases of the side-view probe, we aim to use it to validate specific peptide binding *in vivo* at the cellular level.

5.2 Methods

5.2.1 System architecture

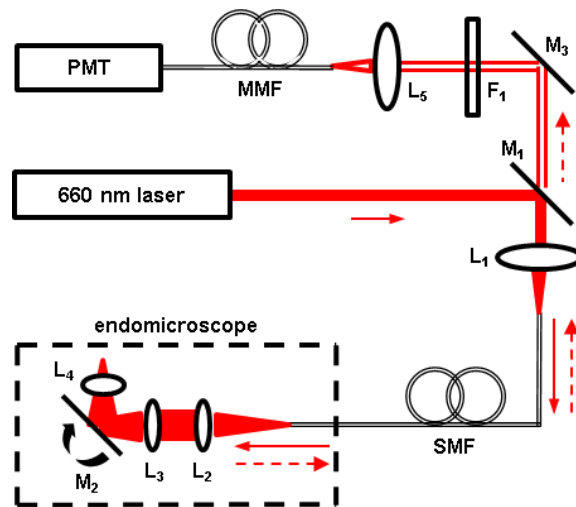


Fig. 5.1. Optical system schematic. Optical configuration of side-viewing endomicroscope. Details provided in text. Key: PMT – photomultiplier tube, MMF – multi-mode fiber, SMF – single mode fiber, L – lens, F – filter, M – mirror.

A schematic for the system design of the side-view endomicroscope is shown, **Fig. 5.1**. We used a solid-state diode laser (660-S, Toptica Photonics) to deliver excitation at $\lambda_{ex}=660$ nm. The beam is reflected by a dichroic mirror M_1 (FF685-Di02-25x36, Semrock) and focused by lens L_1 (C220TMD-B, Thorlabs) into a 2-meter long single mode optical fiber (SMF, SM600, Thorlabs). The light coming out of the fiber is collimated by lens L_2 with $f = 12$ mm (45-262, Edmund Optics) to a beam diameter of 3 mm and focused by lens

L_3 with $f = 6$ mm (45-089, Edmund Optics). L_2 and L_3 have a common diameter of 3 mm. The focused beam is reflected 90 degrees by a 2D resonant MEMS mirror M_2 into a solid immersion lens L_4 with $f = 1$ mm and OD 1.5 mm (65-261, Edmund Optics). Fluorescence (dashed red arrows) travels in the opposite direction along the same optical path, is descanned by M_2 , and focused into the same single mode fiber (SMF). After exiting the fiber, fluorescence is collimated by L_1 , passes through the dichroic M_1 , reflected by M_3 , and passes through a band pass filter F_1 (FF01-716/40-25, Semrock) that transmits from 696 – 736 nm with >93% transmission efficiency, and is focused by lens L_5 (C110TMD-B, Thorlabs) with $f = 6.24$ mm into a 1-meter long multimode fiber (MMF, FT400UMT, Thorlabs). The multimode fiber transmits fluorescence to a photomultiplier tube (PMT) detector (H7422-40, Hamamatsu). The PMT signal is amplified by a high-speed current amplifier (59-178, Edmund Optics). We used a high-speed multi-function data acquisition board (National Instruments, PCI-6115) to digitize the amplified PMT signal. The same board was used to generate control signals to drive the 2D MEMS scanner. The data acquisition board was controlled by a PC running custom LabVIEW software.

5.2.2 Optical design

We performed ray-trace simulations (ZEMAX, ver 13) to design the optics, **Fig. 5.2a**. Our design criteria included diffraction-limited resolution in the center $100 \times 100 \mu\text{m}^2$ of the image with a field-of-view (FOV) of $\sim 400 \times 400 \mu\text{m}^2$, working distance of 100 μm , and $\text{NA} > 0.5$. Only lenses with outer diameter < 3 mm were considered so that the

instrument will be small enough for in vivo imaging. Commercially available lenses were chosen to demonstrate proof-of-concept. **Fig. 5.2b-d** show that spot size (RMS radius) of 0.632, 0.794 and 1.944 μm can be achieved at 0, 75 and 150 μm away from the center of the FOV.

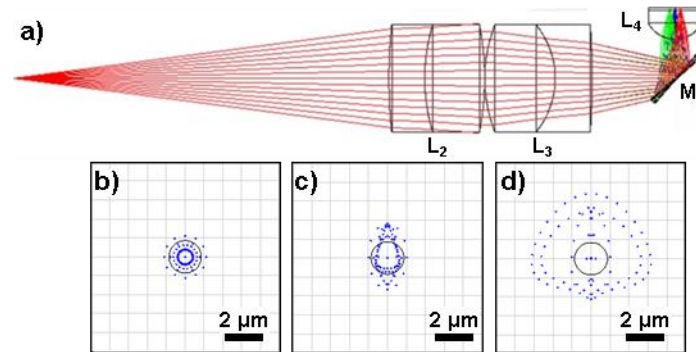


Fig. 5.2. Optical design. a) Ray-trace simulation for design of the distal optics (L2-L4). A field-of-view (FOV) of $400 \times 400 \mu\text{m}^2$ can be achieved. b-d) Spot size (RMS radius) of 0.632, 0.794 and 1.944 μm can be achieved at 0, 75 and 150 μm away from the center of the FOV.

5.2.3 MEMS scanner

Our group have previously developed a compact 2D MEMS scanner with a chip size of $3 \times 3 \text{ mm}^2$ and a 1.8 mm diameter circular reflector. [67] The geometry of the MEMS mirror has been modified to fit the small probe diameter, **Fig. 5.3a**. In order to achieve two-dimensional scanning, orthogonally oriented inner and outer electrostatic comb-drives actuators are coupled to torsional springs to rotate the mirror about either axis. A gimbal frame is used to minimize interference between the two axes. The scanner was fabricated using a 3 step deep reactive-ion etch (DRIE) process with 3 masks. Aluminum was sputtered on the front-side silicon surface to improve reflectivity. For this instrument, the resonant frequencies of the inner and the outer axes were designed to be ~ 1 and ~ 4 kHz,

respectively, to create a Lissajous scanning pattern that covers 400 x 400 pixels with a frame rate of 5 Hz or 600 x 800 pixels with a 1 Hz frame rate. A MEMS holder with OD 3.8 mm was 3D printed and 3 copper pins were inserted for wire bonding, **Fig. 5.3b**.

We measured the angular deflection of the MEMS scanner in either axis to characterize the frequency response. **Fig. 5.3c, d** show the frequency response of the scanner to a sine-wave input at 60 V_{pp} for the X and Y axes, respectively. This device can achieve >5.5° mechanical scan angle at 60 V_{pp} with a drive frequency close to 8.2 kHz and 2 kHz for the X and Y axes, respectively.

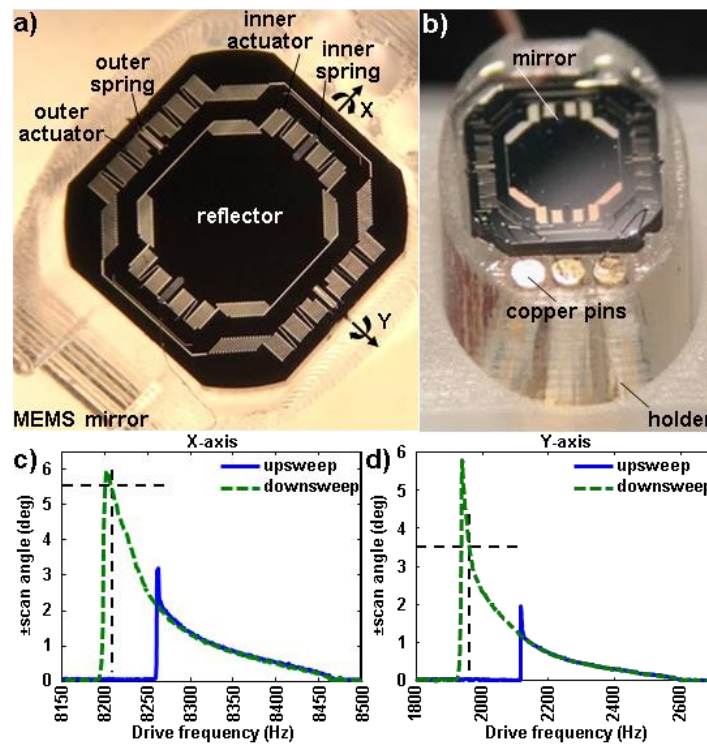


Fig. 5.3. MEMS Scanner. a) Photo shows dimensions of 2D MEMS scanner with locations of inner and outer springs and actuators. b) Mirror is secured in custom holder with copper pins used as contacts for wire bonding electrical connections. Frequency response shows mechanical scan angles of the c) inner and d) outer axes with drive voltage of 60 V_{pp} with either an upswep (low-to-high) or downswep (high-to-low) in frequency.

To achieve a FOV of $300 \times 300 \mu\text{m}^2$, the inner and outer axes were driven at 8210 Hz and 1960 Hz for a mechanical deflection of 5.5 and 3.5 degrees.

At the center of the FOV of the endomicroscope, we measured a lateral resolution of $\sim 0.90 \mu\text{m}$. To satisfy the Nyquist sampling criteria, we must sample with spacing $< 0.45 \mu\text{m}$ between pixels. For in vivo and ex vivo imaging, we used different scanning parameters to our parametric resonance scanner to achieve different frame rates and FOVs. For in vivo imaging, we used drive frequencies of 8210 Hz and 1960 Hz, resulting in actuating frequencies of 4105 Hz and 980 Hz in the X and Y axes. This forms a dense Lissajous scan pattern which repeats itself at 5 Hz to encompass images with dimensions of 400×400 pixels with 100% coverage for a FOV of $300 \times 300 \mu\text{m}^2$. The pixel spacing is $0.75 \mu\text{m}$, and we are under sampling a little bit to maintain a higher frame rate to incur less motion artifact. For ex vivo imaging and optical performance characterization, we used 8210 Hz and 1952 Hz for a frame rate of 1 Hz, a FOV of $300 \times 400 \mu\text{m}^2$ and 600×800 pixels. The pixel spacing is $\leq 0.4 \mu\text{m}$, and meets the Nyquist sampling criteria.

5.2.4 Mechanical design and packaging

We used CAD software (Solidworks, ver 2015) to design the housing to package the optics and scanner, **Fig. 5.4a**. A stainless-steel pin with a diameter of 3 mm was used to fabricate a 1.25 mm fiber ferrule holder, **Fig. 5.4b**. We used a stainless-steel tube with an OD of 3.8 mm and an inner diameter ID of 3 mm to center and align the lenses L_2 and L_3 , **Fig. 5.4f**, and a second stainless steel tube with OD 4.2 mm and ID 3.8 mm to enclose the MEMS scanner and lens L_4 , **Fig. 5.4e**. The MEMS mirror assembled on the 3D printed holder is shown in **Fig. 5.4d**. The distance between L_3 and the MEMS mirror was adjusted

to achieve a working distance of 100 μm . The position of the MEMS mirror was adjusted using a 6-axis precision manipulator to ensure that the reflected beam was at normal incidence to L₄. **Fig. 5.4g** illustrates the assembly and alignment process where the focusing lens holder and the MEMS holder are mounted on high precision stages. After assembly, the probe was sealed using epoxy (G14250, Thorlabs). Before imaging, the endomicroscope was soaked in water overnight to ensure adequate seal. For in vivo imaging, the endomicroscope was mounted onto a motorized rotational and translational platform to precisely control positioning in mouse colon.

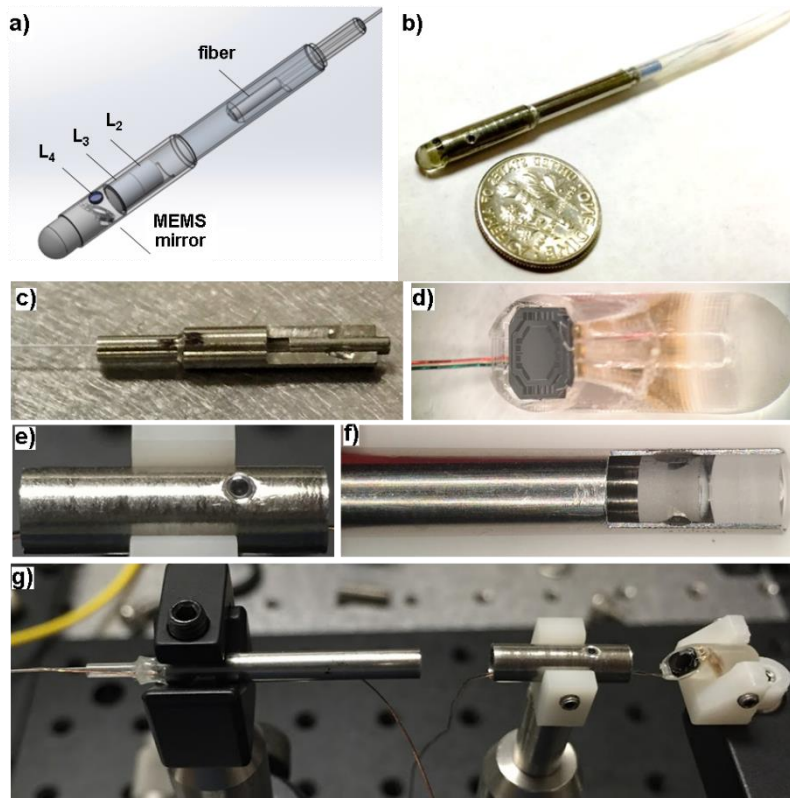


Fig. 5.4. Packaging and alignment. a) CAD drawing shows how instrument is packaged. b) Assembled endomicroscope c) Fabricated fiber ferrule holder. d) MEMS chip mounted on a 3D printed holder. e) Fabricated side-view lens holder. f) Fabricated focusing lens holder. g) Assembly and alignment process.

5.2.5 Imaging performance characterization

We collected reflectance images from a standard USAF resolution target, and plotted the intensity profile in the transverse direction across an edge. The lateral resolution was defined by measuring the width of transition from 10% - 90% of maximum value. The axial resolution was determined by measuring the full width at half-maximum (FWHM) of the signal reflected from the surface of a chrome coated mirror surface. The field of view and distortion were characterized by imaging a grid target (R1L3S3P, Thorlabs) with 100 μm spacing.

5.2.6 Peptide

Our lab has previously developed a peptide that is specific for domain 2 of EGFR. [75] QRH*-Cy5.5 was synthesized by coupling QRH* with water soluble sulfo-Cy5.5- N-hydroxysuccinimide ester (Lumiprobe LLC) respectively overnight with N,N-diisopropylethylamine, followed by HPLC purification. The final purity was confirmed by analytical C18-column. Further characterization was performed with exact mass measurement by Q-TOF (Agilent Technologies) mass spec with ESI (Waters Inc) detection. After lyophilization, the peptides were stored at -80°C and redissolved in water at a concentration of 300 μM before injection.

5.2.7 In vivo imaging

We used a *CPC;Apc* mouse that spontaneously develops pre-malignant (dysplasia) lesions in the distal colon where they are accessible by the side-view endomicroscope.

These mice are genetically engineered to sporadically delete the APC gene, which is mutated in >80 of human colorectal carcinomas. [82] During imaging, 12-week-old *CPC;Apc* mice were anesthetized with 2% isoflurane (Fluriso; MWI Veterinary Supply Co.). We first used a wide-field small animal endoscope (27030BA, Karl Storz Veterinary Endoscopy) with white light illumination to examine the colon for presence of grossly visible adenomas. For use as landmarks, we measured the distance between the endoscope tip and the anus and the clockwise location of the adenoma.

We waited 90 min after intraperitoneal injection of 300 μ M of QRH*-Cy5.5 solution in a volume of 600 μ L to allow the peptide to bind to the target. The distal tip of the endomicroscope was placed into the colon of anesthetized mice. The insertion depth and angle were controlled using the translational stage and the rotational fixture in order to image normal colonic mucosa and adenomas at the same locations as first detected on the wide-field endoscope. Live video streams were collected ~100 μ m below the mucosa surface at 5 frames/sec with a laser power of 1.5 mW. Individual frames with minimal motion artifacts were identified subsequently. After completion of imaging, the mice were euthanized, and the colon was harvested for ex vivo imaging. The optical window of probe was positioned directly en face over the exposed lumen of resected colon to optimize contact. Images were collected with the same laser power as that used in vivo. Previously identified landmarks were used to confirm the locations of the adenomas. The colon was fixed in 10% buffered formalin and paraffin embedded for routine histology (H&E). Images and tissues were collected and analyzed in a total of n = 6 mice. One representative

image was selected from either dysplasia or normal for each mouse. We quantified each image by measuring the average fluorescence intensity from $n = 5$ regions of interest with dimensions of 20×20 pixels picked at random.

5.3 Results

5.3.1 Imaging performance

We collected reflectance images from a standard USAF resolution target with the side-view confocal endomicroscope, Fig. 5.5a. The smallest set of bars (group 7, element 6) can clearly be distinguished, suggesting a qualitatively lateral resolution $< 2.2 \mu\text{m}$, Fig. 4A (inset). A reflectance image of a grid target ($100 \times 100 \mu\text{m}^2$ square grids) shows a maximum field-of-view of $300 \times 400 \mu\text{m}^2$, Fig. 5.5b. Fine details can be seen from fluorescence images of Cy 5.5 stained lens paper, Fig. 5.5c, d. For quantitative measurement, we plotted the intensity profile across an edge, and measured a lateral resolution of $0.87 \mu\text{m}$, defined by the width of transition from 10% - 90% of maximum value, Fig. 5.5e. We measured a full-width-at-half-maximum (FWHM) of $13.2 \mu\text{m}$ by translating a reflective surface in the axial direction, Fig. 5.5f.

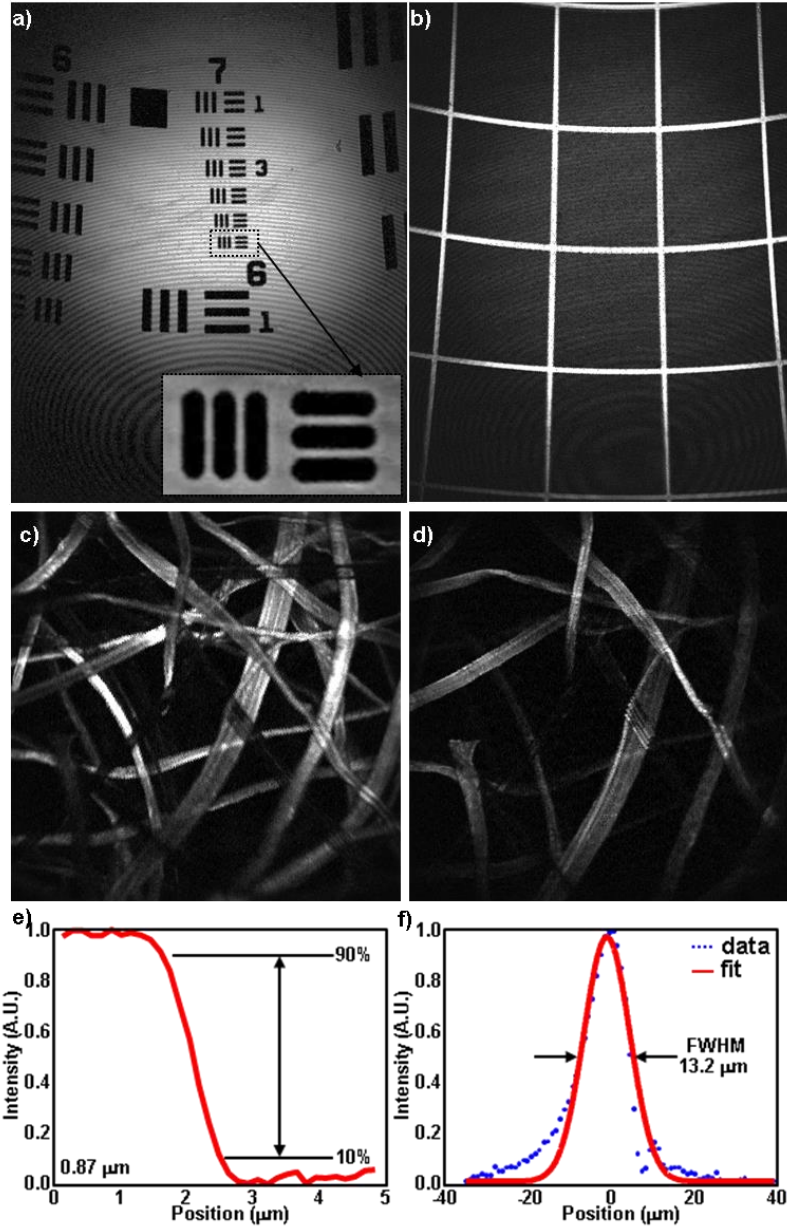


Fig. 5.5. Image resolution. a) Reflectance image of standard target (USAF 1951) can distinguish group 7, element 6 (red box) to support qualitative lateral resolution $<2.2 \mu\text{m}$. b) Reflectance image of grid with $100 \times 100 \mu\text{m}^2$ squares shows a field-of-view of $300 \times 400 \mu\text{m}^2$. c), d) Fluorescence images of a dye stained lens paper. e) Intensity profile across an edge shows quantitative measurement of lateral resolution of $0.87 \mu\text{m}$, defined by the width of transition from 10% - 90% of maximum value. f) We measured full-width-at-half-maximum (FWHM) of $13.2 \mu\text{m}$.

5.3.2 In vivo imaging

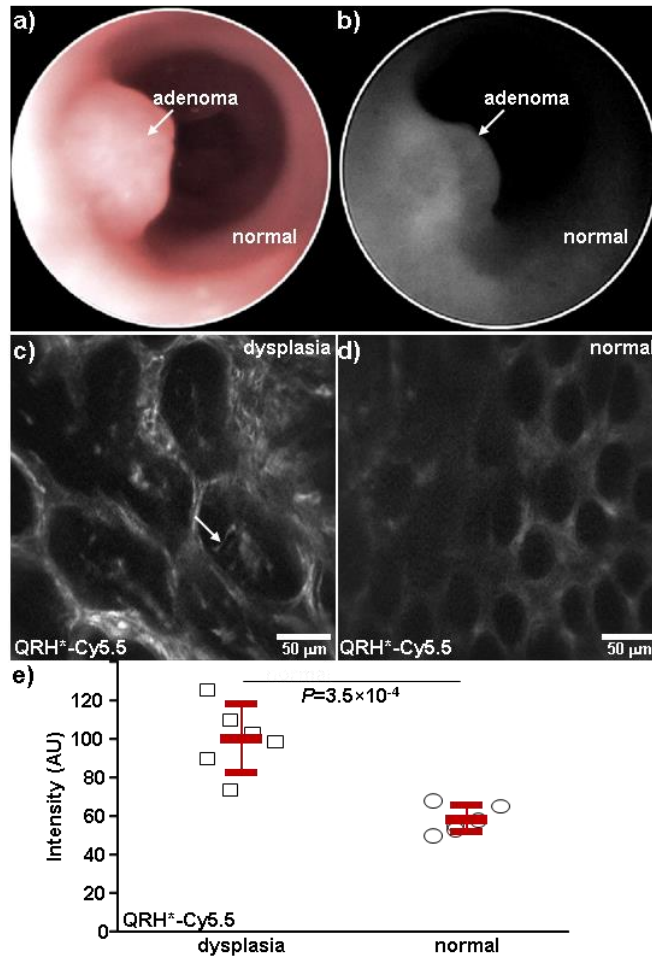


Fig. 5.6. Imaging of mouse colonic dysplasia. a) White light image of *CPC;Apc* mouse colon collected in vivo with wide-field endoscope shows location of spontaneous adenoma (arrow). b) Maximum uptake of the NIR-labeled EGFR peptide QRH*-Cy5.5 is seen from the adenoma 90 minutes after systemic administration. From the in vivo confocal images, c) increased fluorescence intensity is seen from cell surface of dysplastic colonocytes (arrow) while d) minimal staining is seen in normal crypts. e) A significantly greater mean fluorescence intensity was measured from dysplasia compared with that of adjacent normal, 107 ± 19 versus 62 ± 8 AU, from a group of $n = 6$ mice, $P = 3.5 \times 10^{-4}$ by paired two-way t-test.

After injecting QRH*-Cy5.5, we collected in vivo fluorescence images from the distal colon in $n = 6$ *CPC;Apc* mice that spontaneously develop colonic adenomas. **Fig. 5.6a** shows a wide field endoscopic image of the distal colon used to guide placement of

the side view endomicroscope to collect the in vivo images. **Fig. 5.6b** shows a wide field fluorescence image at the same location. Representative in vivo images of dysplasia and normal sections using the side-view endomicroscope are shown, **Fig. 5.6c, d**, respectively. We observed strong cell surface binding within dysplastic crypts (arrow) compared with normal. The mean fluorescence intensities from dysplastic and normal crypts in $n = 6$ mice were quantified, **Fig. 5.6e**. We found a significantly greater result for dysplasia compared to normal, $P = 3.5 \times 10^{-4}$, by paired, two way t-test.

5.3.3 Ex vivo validation

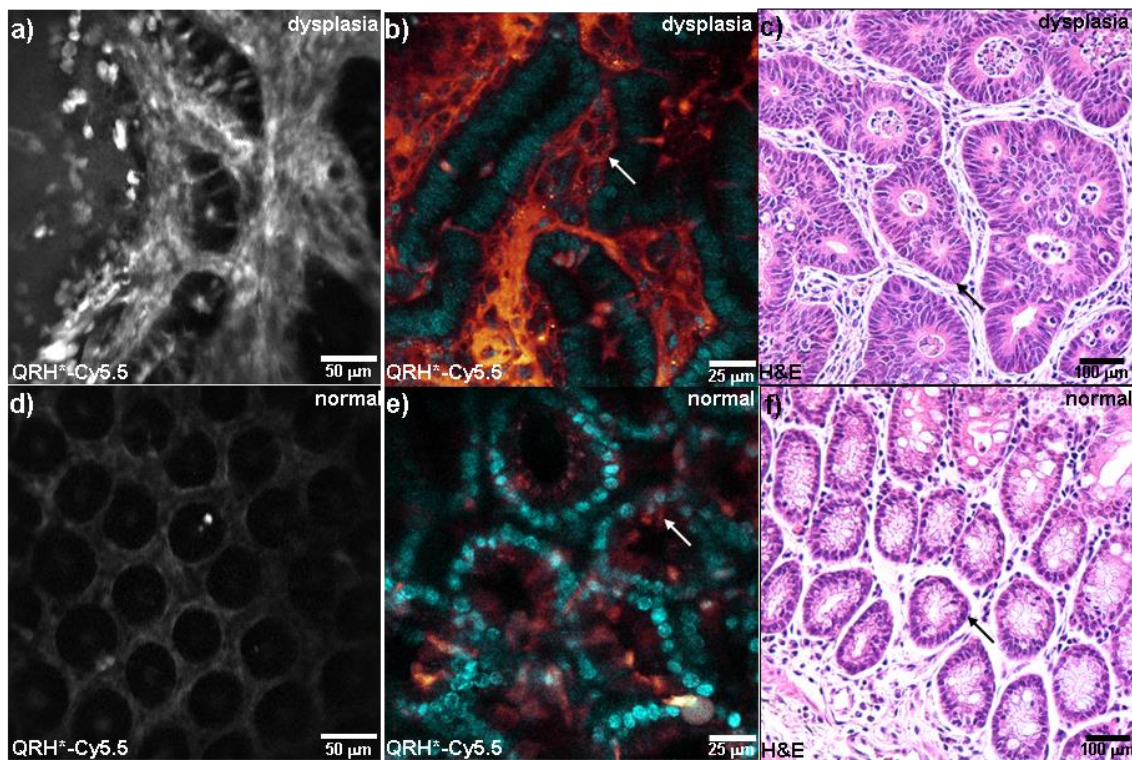


Fig. 5.7. Ex vivo validation. Strong fluorescence intensity is seen from staining of the EGFR peptide QRH*-Cy5.5 to dysplasia in a) the side-view probe and b) a commercial confocal microscope. Minimal uptake of QRH*-Cy5.5 is seen in normal colonic mucosa in d) and e). Representative histology (H&E) of c) dysplasia and f) normal colonic mucosa.

Whole mount tissues were imaged with the side-viewing endomicroscope first, and then stained by DAPI and imaged with confocal microscope (Leica SP5 Upright, Germany) with Cy5.5 and DAPI filters. The colon was then fixed in 10% buffered formalin and paraffin embedded for routine histology (H&E). Sections were cut in the plane parallel to the mucosal surface. Increased intensity (arrow) is seen at the cell surface of dysplastic colonocytes, Fig. 8a,b. We observed greatly reduced staining of both the EGFR peptide to normal colon, Fig. 8d,e. Representative histology (H&E) is shown for dysplasia and normal, Fig. 8c,f.

5.3.4 Mosaic image

The instrument also has the capability to create a mosaic image in the mouse colon. We built a translational and rotational platform using a motorized linear stage (CONEX-LTA-CC, Newport) and a stepper motor (324, Adafruit) to precisely control the position of the probe, **Fig. 5.8a**. Cy5.5 dye was injected into a normal mouse 1 hour before imaging. We first injected Cy5.5, and waited approximately 1 hour for the dye to circulate. We collected images in a video stream of normal colonic mucosa in vivo while translating the endomicroscope a distance of 1 mm and rotating the instrument by 90°. We stitched together individual images to form a mosaic, **Fig. 5.8b**, and warped the composite image to simulated the in vivo anatomy of colon, **Fig. 5.8c**, using custom software (Matlab, Mathworks Inc).

We also created a mosaic image from in vivo images in the colonic dysplasia area after QRH*-Cy5.5 peptide injections, as shown in **Fig. 5.9**. The left side is the normal area,

with low signal intensity. We can clearly see the signal strength increases on the right side, which is the dysplasia area. The morphological change from normal to dysplasia can also be visualized.

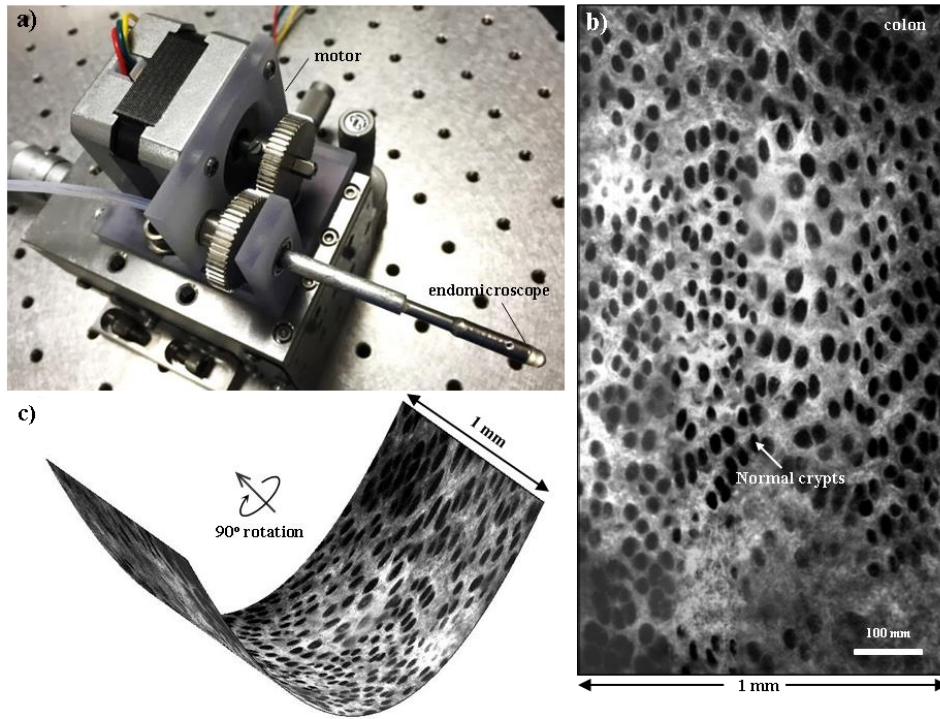


Fig. 5.8. Mosaic image of mouse colon in vivo. a) After systemically injecting Cy5.5 into a normal mouse, imaging was performed 1 hour later. The endomicroscope was axially translated a distance of 1 mm and rotated 90°. b) Mosaicked image. c) Image warped to mimic the geometry of a mouse colon. Mosaic image.

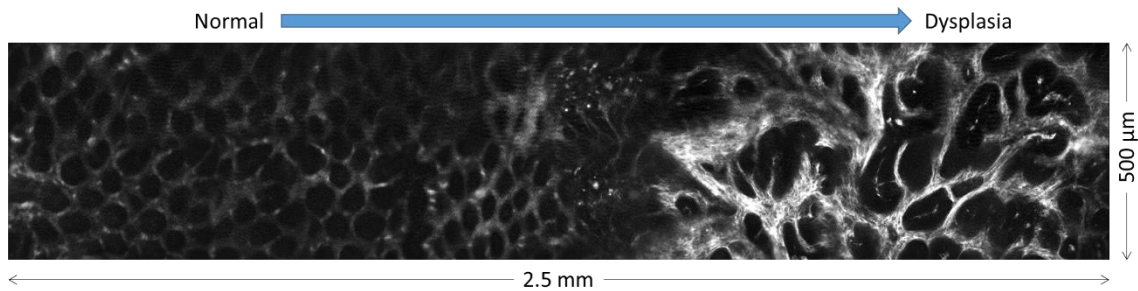


Fig. 5.9. In vivo imaging of colonic dysplasia with QRH peptide.

5.4 Discussion

Here, we present a side-viewing confocal endomicroscope that uses a compact MEMS scanner to collect real time optical sections in mouse colon with high resolution *in vivo*. This instrument exhibited stable operation at 5 frames per second with minimal interference from mechanical vibrations throughout the imaging procedure. We used this endomicroscope to demonstrate *in vivo* binding of a Cy5.5-labeled peptide specific for EGFR expressed in dysplastic crypts that develop spontaneously. Our results illustrate potential for repetitive use of this novel instrument in animals for longitudinal study of molecular patterns expressed during disease development. Also, the small size of this instrument allows for passage through the biopsy channel of a medical endoscope for future clinical translation. Side-viewing is useful for several important clinical applications, such as visualization of molecular expression in the biliary tract and pancreatic ducts to stage early cancer, guide choice for therapy, and monitor therapeutic response.

Confocal endomicroscopy is an emerging imaging technique that can be used to collect histology-like images. In most endoscopic procedures, tissue biopsies are taken at random that result in cumulative pathology charges. The diagnosis is usually unknown until pathology evaluation is completed several days later when the patient has left the clinic and is no longer available to collect any additional biopsies needed. We have developed a novel endomicroscope that provides an instantaneous “optical biopsy”. Physicians can use this instrument to rapidly sample multiple sites, and take physical biopsies only from regions of concern. Furthermore, this technology can be used to stage early epithelial cancers by visualizing below the tissue surface with sub-cellular resolution.

Knowledge of the depth of cancer invasion is needed to determine if local resection is appropriate, and can reduce procedure time and risk for bleeding. Also, we demonstrated images that showed overexpression of EGFR that can be used to guide choice of biologic therapy, such as Cetuximab and erlotinib, FDA approved antibody and small molecule agents, respectively. Physicians can use this enabling technology to determine the best choice of therapy for their patients and to monitor effectiveness.

We have previously demonstrated confocal imaging of a FITC-labeled peptide that binds to human colonic adenomas using a commercial confocal endomicroscope. [71] This instrument uses a coherent optical bundle consisting of ~30,000 individual, multi-mode fibers to collect fluorescence images over a $240 \times 240 \mu\text{m}^2$ field-of-view. The working distance was 50 μm , and the resolution in the lateral and axial dimensions were 1.4 and 7 μm , respectively. The beam was scanned at the proximal end of the fiber bundle by a 4-kHz oscillator for horizontal scanning (lines) and a 12-Hz galvo mirror for vertical scanning (frames). In our current design, we can achieve greater signal and depth with use of bright NIR fluorophores. Also, a Cy5-labeled peptide specific for c-Met has been used to detect colonic adenomas in vivo with fluorescence colonoscopy using intravenous administration. In this clinical study, a clear increase in intensity was observed from adenomas with either polypoid or flat morphology. Our instrument can be complementary by providing optical sections from these localized regions of disease after they have been localized first with wide-field imaging.

Efforts have been made recently to develop side-view endomicroscopes to image hollow organs in small animals. A long graded-index (GRIN) lens based endomicroscopic

system with an outer diameter of 1.25 mm and length of 50 mm was developed to image mouse colon, esophagus, small intestine and trachea. [119] The instrument had a FOV of $250\ \mu\text{m} \times 250\ \mu\text{m}$ and lateral and axial resolution about 1 and $10\ \mu\text{m}$. This approach was later adopted to a multiphoton and OCT imaging system. [121] In vivo imaging results in hollow organs had been demonstrated, showing the great advantage of the side-view confocal architecture. However, this table-top setup required to move the animal in order to target different areas, which may be difficult when imaging certain areas. The use of a long GRIN lens will also present a significant chromatic aberration. A side viewing confocal endomicroscope based on spectrally encoded confocal microscopy (SECM) has been demonstrated, with an outer diameter of 5.85 mm, a 100kHz line-scan rate, lateral and axial resolution about 2 and $10\ \mu\text{m}$, and a FOV of $280\ \mu\text{m}$ [125]. The very high line scan rate is enabled by using a high speed wavelength-swept laser source, but this also limits the instrument to be used only in reflectance mode.

In this work we used a 2D XY MEMS scanner to acquire horizontal sections in the tissue. We have also demonstrated a XY/XZ scanner which enables switchable horizontal and vertical sectioning. [126] We plan to integrate this type of scanner into the side-view probe to collect vertical sections in vivo.

5.5 Summary

We have developed a side-view confocal endomicroscope that capture real time submicron resolution images in the distal colon of a live mouse. We demonstrate in vivo near-infrared fluorescence images at $100\ \mu\text{m}$ depth and 5 frames per second from binding

of a peptide specific for EGFR to dysplastic crypts. This instrument can visualize overexpressed molecular targets, and may be useful for clinical translation to detect disease, guide choice for therapy, and monitor therapeutic response.

Chapter 6 Side-Viewing Confocal Endomicroscope for XY/XZ Imaging

6.1 Introduction

Tremendous advances have been made in technological development of whole body molecular imaging, including PET, SPECT, MRI, bioluminescence, and ultrasound. However, a great unmet need still exists for high resolution imaging of biological processes that occur in the epithelium, the thin layer of tissue where many important cancers originate. Confocal endomicroscopes designed with a fiber bundle are used in the clinic, but they can only create images in the horizontal plane [10]. Imaging in the plane perpendicular to the tissue surface is also important because epithelial cells differentiate in the vertical direction [127]. Subtle changes in normal tissue differentiation patterns can reveal the early expression of cancer biomarkers. We have previously developed a MEMS based endomicroscope for repetitive in vivo imaging in mice, which can be used to collect horizontal images in real time [67]. In this work, we present a side-viewing confocal endomicroscope that can collect images in either horizontal or vertical plane using an integrated monolithic electrostatic 3D MEMS scanner.

Recently several groups have demonstrated endomicroscopes with miniature axial scanning mechanisms. Optiscan Pty Ltd and Pentax Corp developed the first clinical

confocal laser endoscope integrated into a conventional video endoscope. Depth of imaging plane can be adjusted from the surface to 250 μm below the tissue, using an electrically actuated shape memory alloy (SMA) [128]. Piyawattanametha et al developed a dual axes confocal endomicroscope using a 2D MEMS scanner for lateral scanning and a micro motor for axial scanning [57]. Both of the systems used slow and bulky actuators to change the focal plane for horizontal imaging, which are not practical to be used for real time vertical sectioning. Recently several groups have demonstrated MEMS actuators with axial scanning capability. A 3D confocal microscope using two separate electrostatic MEMS mirrors for lateral scan and depth scan was reported by Jeong et al. [129], but it had a very small axial displacement of 10 μm at 200 V and ± 27.5 μm at resonance. Liu et al also developed a 3D confocal endomicroscope using two electrothermal MEMS devices, one for 2D lateral scanning and one for axial scanning of a micro objective [58]. A depth scan range of 400 μm was demonstrated at only 2 V driving voltage. However, the frame rate is too low for in vivo imaging due to the slow response time of electrothermal actuators.

Previously we have demonstrated a monolithic 3D MEMS scanner in a dual-axis confocal endomicroscope for switchable horizontal/vertical cross-sectional imaging. Here, we integrate a similar 3D scanner into our previously developed side-viewing confocal endomicroscope to collect either horizontal or oblique plane images in vivo.

6.2 Methods

6.2.1 System architecture

The system schematic, as shown in **Fig. 6.1**, is modified from the one presented in the previous chapter. We added a second laser (iChrome MLE LFG, Toptica Photonics), which is a multi-laser engine, with 445, 488, 515 and 561 nm excitation wavelength, in addition to the 660 nm laser. A flip mirror (FM) is used to switch between these two lasers. We used a dichromatic mirror (Di01-R442/514/561, Semrock) and a band pass filter (FF01-485/537/627), for fluorescence signal separation and filtering. This upgraded illumination and collection system would allow the use of fluorophores with excitation peaks at 445, 515, 561 and 660 nm.

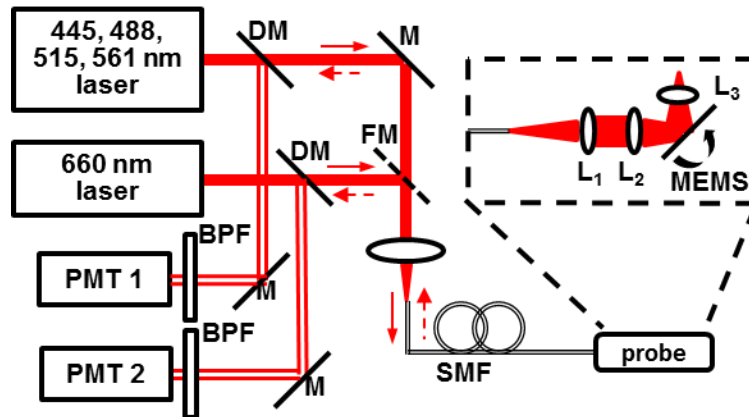


Fig. 6.1. Schematic. Optical configuration of side-viewing endomicroscope. Details provided in text. Key: PMT – photomultiplier tube, MMF – multi-mode fiber, SMF – single mode fiber, L – lens, F – filter, M – mirror.

6.2.2 Optical design

The optical design and ray-trace simulations (ZEMAX, ver 13) are shown in **Fig. 6.2a**. The light coming out of the fiber is collimated by lens L_1 with $f = 12$ mm (45-262,

Edmund Optics) to a beam diameter of 3 mm and focused by lens L_2 with $f = 6$ mm (45-089, Edmund Optics). L_1 and L_2 have a common diameter of 3 mm. The focused beam is reflected 90 degrees by a 2D resonant MEMS mirror into a distal imaging lens L_3 with $f = 2$ mm and OD 1.5 mm (65-263, Edmund Optics). When the outer axis of the scanner operates in rotational mode around the Y axis with $\pm 8^\circ$, as shown in **Fig. 6.2b**, the focal spot moves laterally over a FOV of 760 μm . When it operates in out-of-plane translational mode, as shown in **Fig. 6.2c**, the focal depths change as well as the lateral spot location, generation an oblique scan line. **Fig. 6.2d-f** show the focus location when the MEMS scanner is at +105, 0 and -105 μm with respect to the neutral position. The corresponding focal depths are +90, 0 and -110 μm with lateral shift of -101, 0 and 112 μm . With an axial displacement of 210 μm , we can achieve depth scanning over a range of 200 μm .

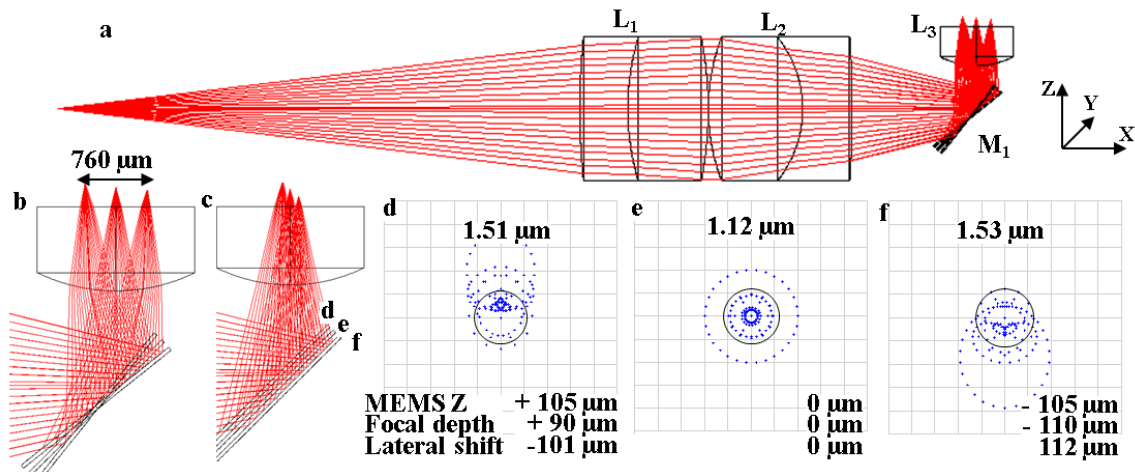


Fig. 6.2. Optical design and Zemax simulation. a) Ray-trace simulation for design of the distal optics. b) Horizontal plane imaging mode. c) Oblique plane imaging mode. d-f) Spot size and focal depth when the MEMS mirror is at +105, 0 and -105 μm with respect to the neutral position.

6.2.3 Geometry of the MEMS chip

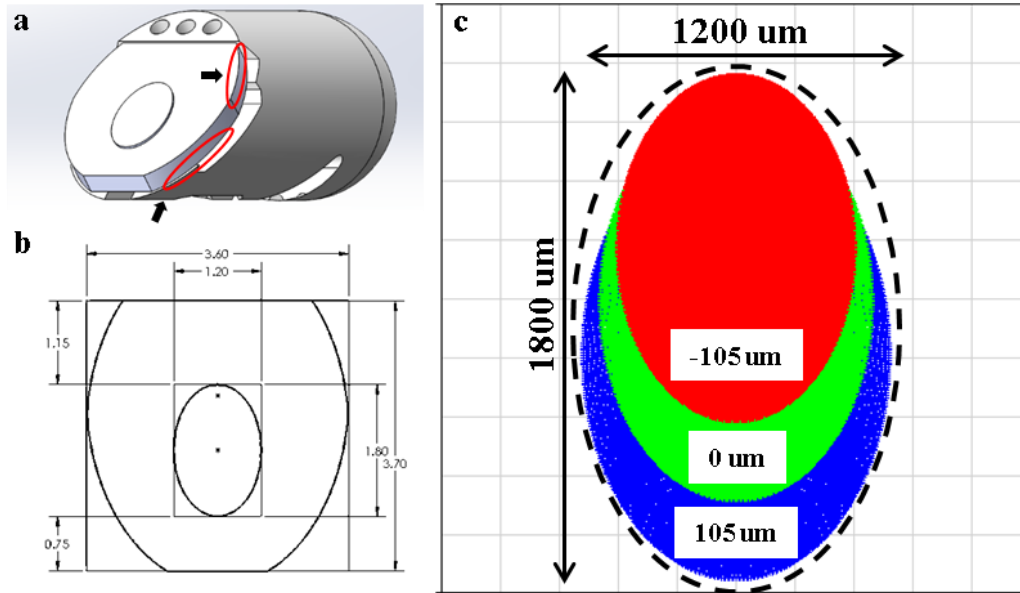


Fig. 6.3. Geometry of the MEMS chip and the reflective mirror. a) Solidworks model of the MEMS chip inside the housing. b) Optimal MEMS chip geometry. c) Zemax model of the beam spots on the reflective mirror.

To make sure the MEMS chip can fit inside the tubing with an ID of 3.8 mm, the optimal geometry was determined in the Solidworks model, as shown in **Fig. 6.3a**. Since the MEMS chip has a thickness of 550 μm , both the upper edge and the lower edge (marked by arrows) should be considered. A clearance of 100 μm was incorporated in the design to allow for misalignment during MEMS assembly. The resulting MEMS geometry is shown in **Fig. 6.3b**. To determine the required reflective mirror size to cover the beams spot, a Zemax model was constructed, as shown in **Fig. 6.3c**. The beam spot on the mirror was measured when the mirror is at +105, 0 and -105 μm with respect to the neutral position. An oval shaped reflective mirror with 1800 μm x 1200 μm is needed to cover the beams spots.

6.2.4 3D MEMS scanner

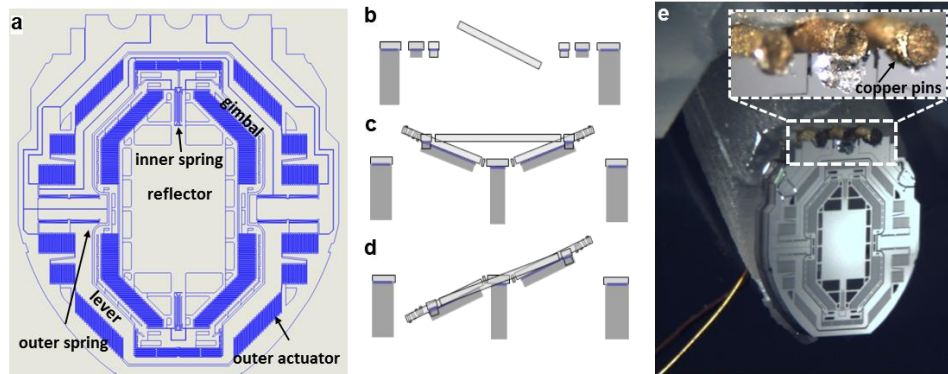


Fig. 6.4. 3D MEMS scanner. a) Schematic of the 3D MEMS scanner, with U-shaped levers for switchable Y/Z actuation. b) X tilting mode. c) Z piston mode. d) Y tilting mode. e) MEMS chip assembled on a custom designed holder with copper pins for electric conduction.

We have previously developed a compact, monolithic electrostatic, 3D micro-electro-mechanical systems (MEMS) scanner for a dual axes confocal endomicroscope [126], based on the principle of parametric resonance. [107] Using a similar design, we developed a MEMS scanner with switchable XY/XZ scanning for a side-view confocal architecture, **Fig. 6.4a**. The mirror is mounted on a gimbal frame to minimize crosstalk between the inner and outer axes. The reflective mirror is linked to the gimbal frame through a pair of multi-beam torsion springs and can rotate around the torsion springs defined as the X-axis, shown in **Fig. 6.4b**. The gimbal is attached to U-shaped suspensions, and it can perform either Z-axis piston motion or Y-axis rotational motion, respectively shown in **Fig. 6.4c** and **Fig. 6.4d**, when driven at different frequencies. This device was fabricated with a deep cavity on the back side of the substrate to allow for large axial displacements using a 3 step deep reactive-ion etch (DRIE) process. A cutting-free SOI micromachining process was employed to fabricate this scanner with irregular shape.

We etched air releasing holes around the large reflective mirror to minimize air damping effects after packaging. The surface is coated with a 70 nm layer of aluminum (Al) for high reflectivity >80% between 400 and 800 nm.

6.2.5 Scanner characterization

The scanner was actuated into resonance by sweeping the driving frequency near twice of the eigenfrequency. The tilt angles for X and Y-axes at different frequencies were measured using a laser beam and a position sensing detector (PSD), as shown in **Fig. 6.5a**, **b**. Both axes were driven by 60Vpp sine waves. Mechanical angles of $\pm 10^\circ$ can be achieved in both axes. To characterize axial scanning performance in Z-axis, we used a laser displacement sensor to measuring the out-of-plane displacement driven by a 60Vpp square wave with 35% duty cycle, shown in **Fig. 6.5c**. A maximum scan range of 300 μm can be achieved. Operating frequencies for X, Y and Z-axes were chosen at 9090 Hz, 1480 Hz and 1100 Hz, with scan range of $\pm 10^\circ$, $\pm 8.5^\circ$ and $\pm 105 \mu\text{m}$. When the scanner operates in XZ mode, an oblique imaging plane was obtained, as shown in **Fig. 6.5d**. An imaging depth of 200 μm and lateral range of 213 μm is achieved at the operating frequency of the Z-axis, generating a scan range of 292 μm in the oblique plane.

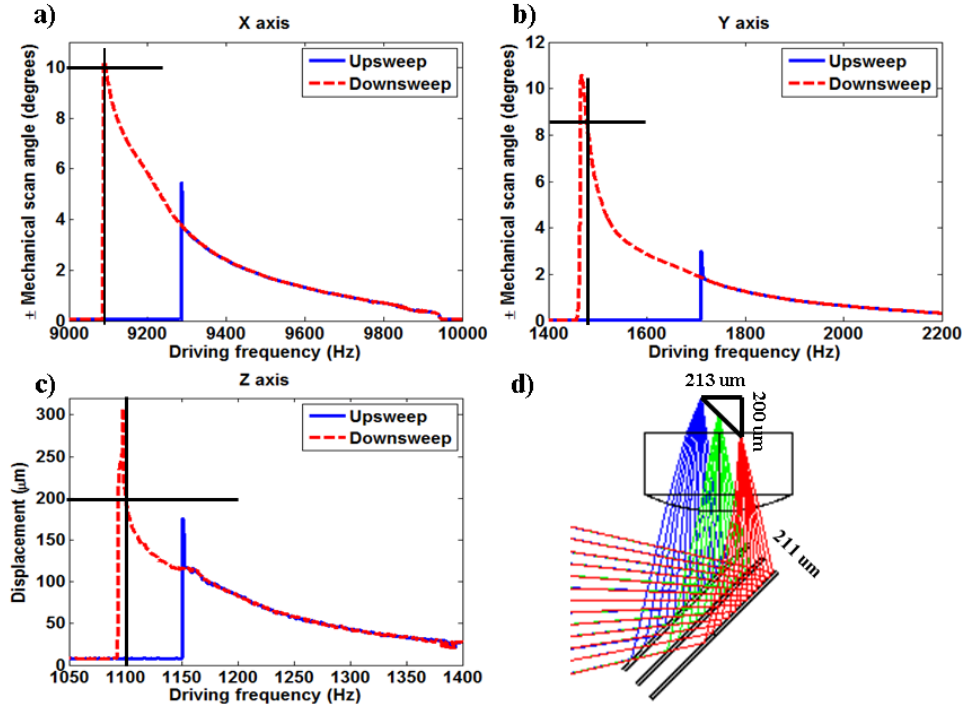


Fig. 6.5. Characterization of the MEMS scanner. a) X-axis rotation motion, b) Y-axis rotation motion, c) Out-of-plane Z-axis translation motion, d) Oblique scanning range at the operating frequency of the Z-axis.

6.2.6 Switchable horizontal/vertical imaging

By applying different driving frequencies, the scanner can alternate between Z-axis piston and Y-axis tilting modes to switch the plane of imaging between vertical and horizontal. We used $60 V_{pp}$ sine waves with 9090 Hz and 1480 Hz to drive the X-axis and Y-axis respectively for horizontal plane imaging, with an FOV of $700 \times 500 \mu\text{m}^2$. For vertical plane imaging, we used a $60 V_{pp}$ sine wave with 9170 Hz for the X-axis and a $60 V_{pp}$ square wave with 35% duty cycle and 1100Hz for the Z-axis, with an FOV of $500 \times 292 \mu\text{m}^2$. A dense Lissajous scan pattern is formed that repeats itself at 10 frames/second, generating images in either the vertical or horizontal plane with dimensions of 400×300 pixels, at 100% coverage.

6.2.7 Packaging and alignment

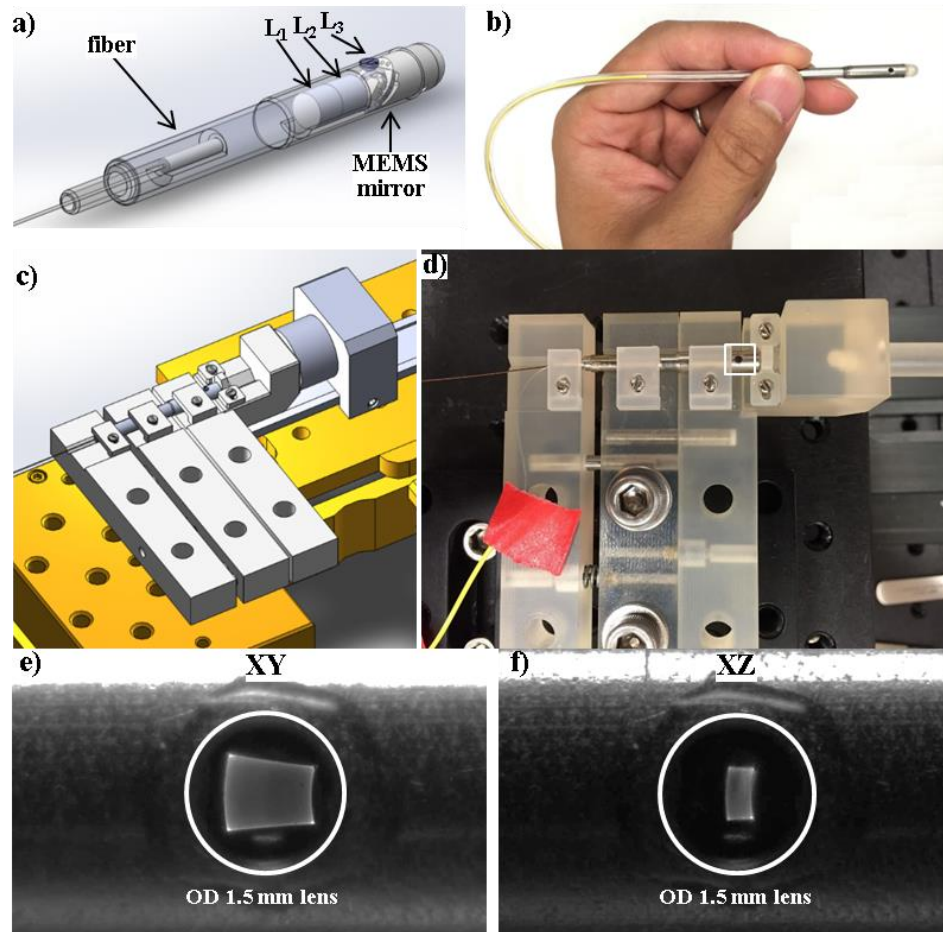


Fig. 6.6. Packaging and alignment. a) Solidworks design. b) Packaged instrument. c) CAD drawing of alignment fixtures. d) Alignment procedure, using the location of 2D scan patterns exiting L_3 . Different scan patterns can be seen when the MEMS operates in e) XY or f) XZ mode.

We used a stainless-steel tube with an outer diameter (OD) of 4.2 mm and an inner diameter (ID) of 3.8 mm to house L_3 and the MEMS mirror holder, and another tube with OD of 3.8 mm and ID of 3 mm to house L_1 and L_2 . The end tube is fabricated using a stainless steel pin with OD of 3mm to fix the fiber ferrule in place. We designed the MEMS holder such that no wire bonding is need for electric conduction. The MEMS chip holder

was fabricated from M3 Crystal, an acrylic based resin with high strength and stiffness, using a high precision 3D printer (ProJet 3500HD MAX, 3DSystems) with 16 μm resolution. We inserted 3 copper pins at for use as electrical contacts to deliver power. The pins were glued to the contact pins of the MEMS chip instead of wire bonding. The Solidworks design of the probe is shown in **Fig. 6.6a** and the actual fabricated probe is shown in **Fig. 6.6b**. Alignment fixtures were designed, as shown in **Fig. 6.6c**, such that the distance between the fiber tip to L_1 , L_2 to MEMS mirror and MEMS mirror orientation can be precisely adjusted. During alignment, the MEMS scanner was actuated to create a laser scan pattern at L_3 , as shown in **Fig. 6.6d-f**. This can be used to actively adjust the MEMS scanner location such that the scan pattern is centered with respect to L_3 .

6.2.8 Resolution and FOV

We measured the lateral resolution using a standard (USAF 1951) resolution target. The field of view and distortion in the horizontal imaging plane were characterized by imaging a grid target (R1L3S3P, Thorlabs) with 100 μm spacing. The imaging depth of the probe was measured using two reflective targets with structures in the Z-axis.

6.2.9 Mouse model of colorectal cancer with tdTomato optical reporter

All animal studies were performed in compliance with University of Michigan regulations and with approval by the University Committee on the Use and Care of Animals (UCUCA). We used a mouse genetically engineered to expresses tdTomato with peak single photon excitation at ~ 560 nm. [130] In the wild-type mouse, a *loxP*-flanked

STOP cassette prevents transcription of the downstream optical reporter gene. When bred with mice that express Cre recombinase under control of the human *CDX2* promoter/enhancer sequence (CPC), the STOP cassette is deleted, and tdTomato is expressed constitutively in the epithelium of adult mouse colon. [93] [131] For both in vivo and ex vivo imaging, we used an excitation wavelength of 561 nm and 1 mW laser power at the sample plane.

6.3 Characterization

6.3.1 Resolution and FOV

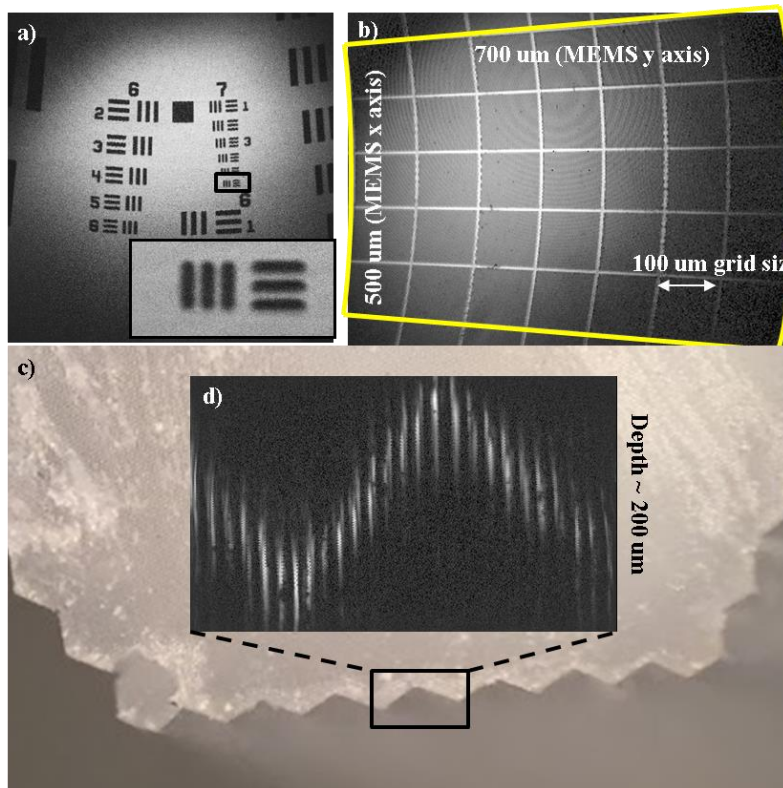


Fig. 6.7. Performance characterization. a) Reflectance image of a USAF target. b) Grid target image showing the FOV. d) XZ image of c) a 3D phantom with micro trenches, showing the imaging depth of $\sim 200 \mu\text{m}$.

The imaging resolution is demonstrated using a standard USAF targeted, from which the smallest element in group 7 can be clearly visualized, **Fig. 6.7a**. Image of a grid target with 100 μm spacing shows a lateral FOV of 700 x 500 μm^2 , **Fig. 6.7b**. We used a 3D phantom with micro trenches to characterize the imaging depth, as shown in **Fig. 6.7c**. The trenches have a depth of around 200 μm . In XZ imaging mode, **Fig. 6.7d**, the trench can be visualized from top to bottom, showing an imaging depth of 200 μm . All the measurements were performed at 660 nm wavelength.

6.3.2 Imaging of 3D fluorescent phantom

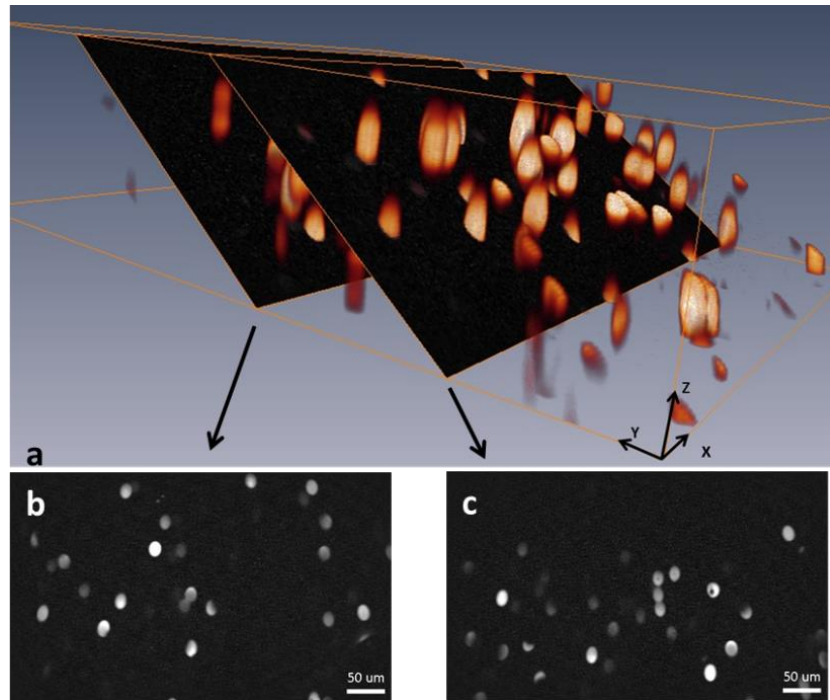


Fig. 6.8. 3D reconstruction of fluorescent beads phantom. a) 3D reconstructed image. b), c), oblique plane images used for reconstruction.

To show the 3D imaging capability of the probe, a fluorescent beads phantom was constructed by mixing 15 μm beads (excitation peak at around 670 nm) with UV curing

epoxy. A series of XZ images were captured while the probe moves along the sample across a 1 mm range using a motorized stage with a step size of 1 μm . Images were post processed using Matlab and a 3D image was constructed using 1,000 oblique plane images, **Fig. 6.8a**. Oblique plane images marked with arrows are shown in **Fig. 6.8b, c**.

6.4 Applications

6.4.1 Imaging of colonic dysplasia with peptide

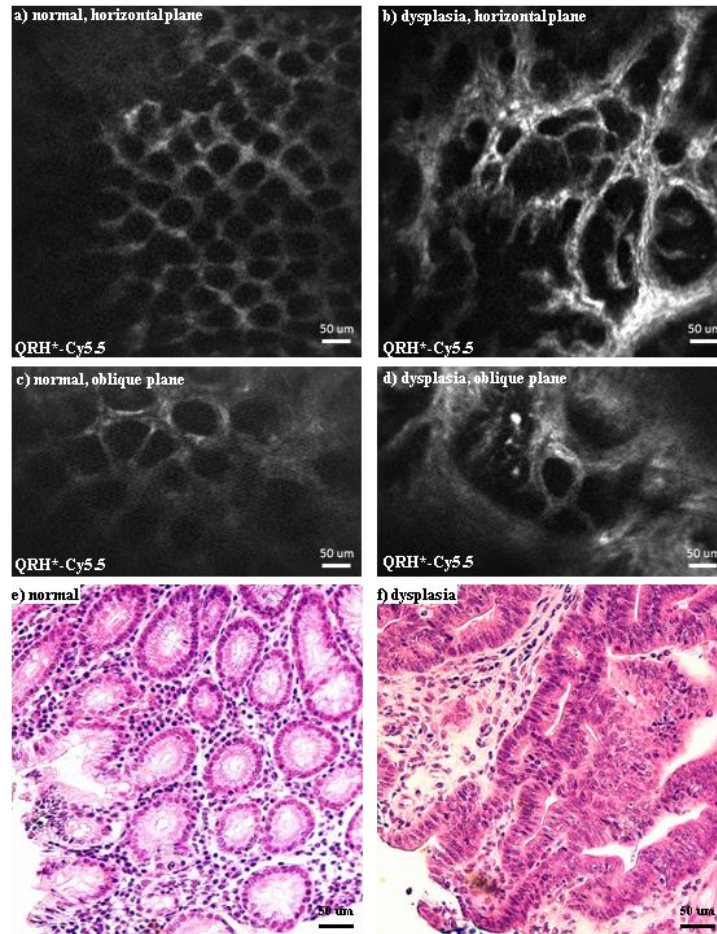


Fig. 6.9. Ex vivo images of mouse colon tissue with EGFP peptide binding. a), b) Horizontal images of normal and dysplastic tissue. c), d) Oblique images of normal and dysplastic tissue. e), f) Corresponding histology.

The probe was placed in direct contact with the surface of resected colon to assess EGFR expression in pre-cancerous crypts. NIR fluorescence images of adenoma and normal colonic mucosa were collected in horizontal and oblique planes, with laser wavelength of 660 nm. “Switching” of the imaging plane was accomplished by tuning the parameters of the drive signals to the scanner. Normal mucosa shows minimal staining of circularly-shaped crypts with relatively uniform dimensions, **Fig. 6.9a**. A horizontal view of dysplasia shows irregular crypt architecture with variable dimensions and a complex branching pattern, **Fig. 6.9b**. We observed the EGFR peptide to intensely stain the entire length of dysplastic crypts in the oblique view, **Fig. 6.9d**, while only faint signal was seen for normal mucosa, **Fig. 6.9c**. Corresponding histology of normal and dysplastic tissue are shown in **Fig. 6.9e, f**.

6.4.2 Imaging of tdTomato optical reporter mouse

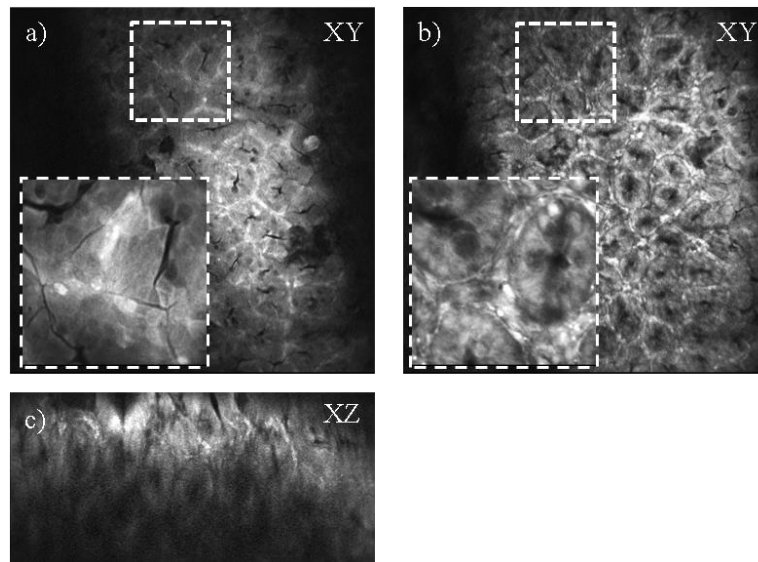


Fig. 6.10. Ex vivo images of tdTomato mouse colon tissue. Horizontal images at a) 20 μm and b) 60 μm . c) Oblique plane image.

Organs of a euthanized tdTomato mouse were imaged using the probe in XY/XZ modes, with laser wavelength of 561 nm. Horizontal plane images of colon tissue at depth of 20 μm and 60 μm are shown **Fig. 6.10a, b**. By changing the driving voltage of the MEMS scanner, electrical zoom is achieved by reducing to a much smaller FOV, as shown in the dashed rectangles in **Fig. 6.10a, b**. Individual goblet cells inside each crypt can be clearly visualized. At the same location, an oblique plane image is shown in **Fig. 6.10c**. Horizontal plane images of ileum, heart, kidney, liver, small intestine and proximal colon are shown **Fig. 6.11a-f**.

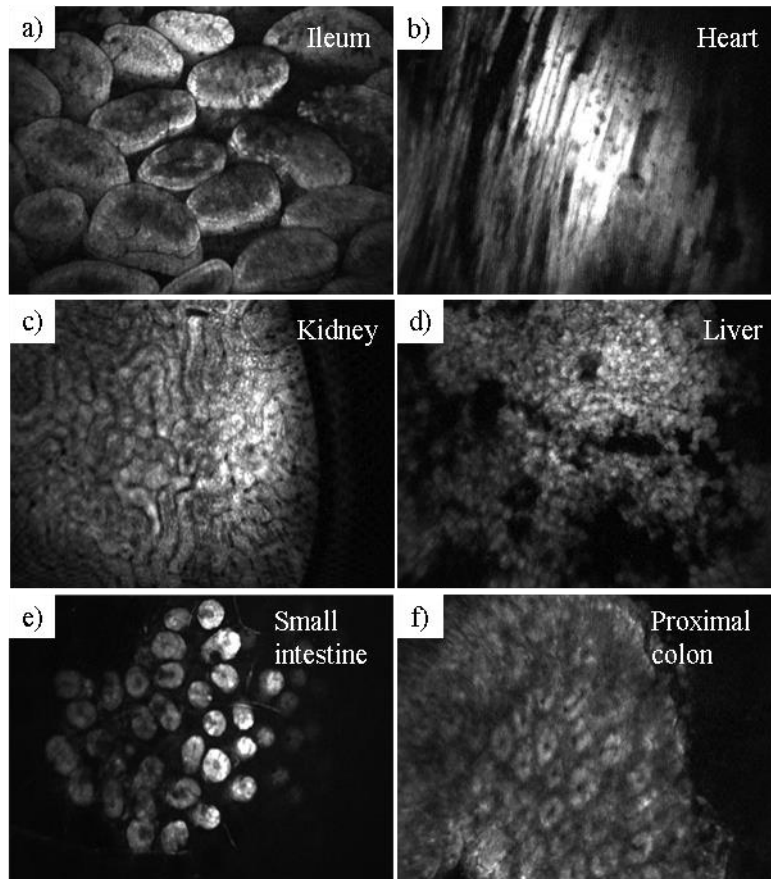


Fig. 6.11. Ex vivo images of different organs of tdTomato mouse. Images of a) Ileum. b) Heart. c) Kidney. d) Liver. e) Small intestine. f) Proximal colon.

In vivo imaging of optical reporter mouse with colonic dysplasia. A wide-field small animal endoscope (27030BA, Karl Storz Veterinary Endoscopy) with white light illumination was first used to examine the colon for presence of grossly visible adenomas. Then the distal tip of the endomicroscope was placed into the colon of anesthetized mice. The insertion depth and angle were controlled using the translational stage and the rotational fixture in order to image normal colonic mucosa and adenomas at the same locations as first detected on the wide-field endoscope. Images were acquired with 5 Hz frame rate using a laser power of 1 mW on the sample plane. Different structures were observed between normal and dysplastic tissue, in both the horizontal and oblique plane images, as shown in **Fig. 6.12**.

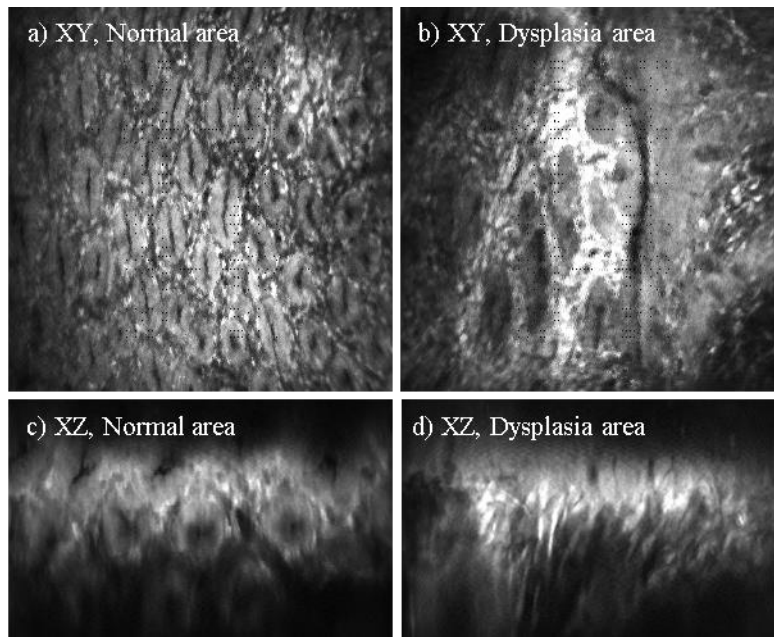


Fig. 6.12. In vivo images of tdTomato mouse colon tissue. Horizontal images of a) normal b) dysplastic tissue. Oblique plane images of c) normal d) dysplastic tissue.

6.4.3 Inflammation monitoring in the mouse colon

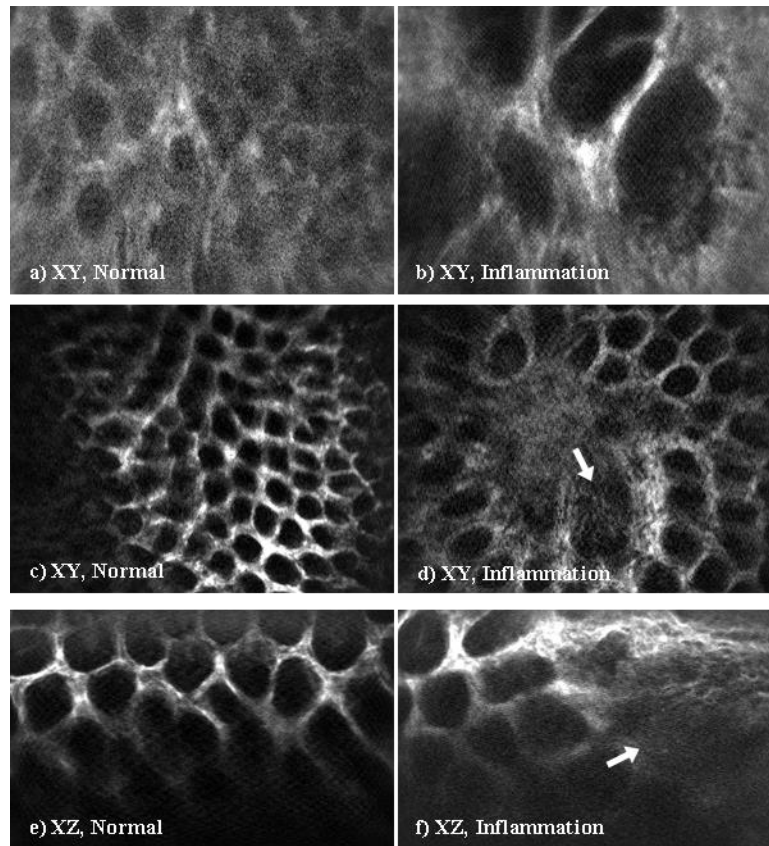


Fig. 6.13. In vivo and ex vivo images of mouse colon with IBD. In vivo images of a) normal and b) inflammatory tissue in the horizontal plane. Ex vivo images of c) normal and d) inflammatory tissue in the horizontal plane. Ex vivo images of e) normal and f) inflammatory tissue in the oblique plane.

A mouse model with inflammatory bowel disease (IBD) was constructed by feeding Dextran Sulfate Sodium (DSS). To monitor the process of IBD development, the mouse was injected with Cy 5.5 dye (concentration of 200 μM) and imaged using the endomicroscope. Horizontal plane images were acquired in vivo, as shown in **Fig. 6.13a, b**. Differences between normal and inflammatory tissue can be observed. The mouse was later euthanized and the colon tissue was harvested for ex vivo imaging. Perfectly round

crypts were observed in the normal area in the horizontal imaging plane, **Fig. 6.13c**. A suspicious area was found in **Fig. 6.13d**. To verify whether this is an inflammatory area, oblique plane images were acquired, **Fig. 6.13f**, showing an abrupt change of structure. This shows that oblique plane imaging can provide extra information to help distinguish between normal and disease areas.

6.5 Summary

We have developed a side-view confocal endomicroscope that can image either horizontal or oblique planes in real time. We demonstrate the potential applications of the probe, including peptide binding validation, tumor development monitoring and IBD disease monitoring. This will be a useful tool for biologists to perform in vivo studies in hollow organs of small animals.

Chapter 7 MEMS-based multiphoton microscopy for vertical sectioning

7.1 Introduction

Conventional multiphoton microscopes can be used to collect 3-dimensional (3D) images in optically thick specimens. Images in the horizontal (XY) plane can be collected easily with lateral beam scanning. Either the objective or specimen must move physically to collect images in the axial (XZ) direction. Many important biological processes, such as normal epithelial development [132], stem cell migration [133], wound healing [134], and neuronal activity [135], are best studied in vivo with images collected in the direction perpendicular to the tissue surface or the vertical plane. This orientation is can be achieved by collecting a stack of horizontal images and performing a reconstruction. However, this approach is not practical because it is time-consuming and prone to motion artifacts from vibrations introduced in the specimen. We aim to demonstrate a new approach to perform beam scanning in the axial direction using a microelectromechanical systems (MEMS) mirror located remotely.

The epithelium of hollow organs, such as colon, is a thin layer of biologically active tissue with depth of $\sim 200 \mu\text{m}$. Imaging in the vertical plane with beam scanning has recently been demonstrated using a remotely located mirror. [136] Two objectives are used

to introduce equal but opposite aberrations in the beam wavefront during axial scanning to achieve diffraction-limited image resolution. [118] A fast moving mirror was constructed using a pair of identical galvanometer motors mounted in opposite directions, with scan rate up to 2.7 kHz. Using this method, aberration free images can be achieved at fast speeds while preserving the high numerical aperture needed to produce multiphoton excited fluorescence images without moving either the objective or specimen. A compact mirror with a small footprint that performs fast axial scanning may further improve performance and extend the applicability of this technique for in vivo imaging.

We demonstrate feasibility to scale down this axial scan strategy by using miniature mirrors and actuators fabricated with MEMS methods. We have previously developed a lateral MEMS-based scanner using the principle of parametric resonance [67], where the drive signal is applied at frequency near $2\omega_o/n$ (ω_o is the natural frequency of vibrational modes and n is an integer ≥ 1) [107]. We have also shown a novel axial actuator based on electrostatic actuation and parametric resonance that can achieve high speeds with large displacements [126]. We combine these two devices in a remote location to collect real time optical sections of multiphoton excited fluorescence in either the horizontal or vertical plane. We must achieve minimal lateral tilt angles to produce distortion free images over the axial scan range at fast speeds.

7.2 Methods

7.2.1 System architecture

A Ti:sapphire (Mai Tai DeepSee HP DS, Spectra-Physics) laser with a tunable spectral range of 690-1040 nm provides excitation (red arrows) with ~100 fs pulse width at 80 MHz, Fig. 1. The pulse duration was minimized with a dispersion pre-compensation unit located inside the laser housing. A half wave plate (HWP, 10RP42-3, Newport) is used in combination with a linear polarizer (LP, 10GL08AR.16, Newport) to adjust power. The beam is initially p-polarized after passing through a polarizing beam splitter (PBS, PBS252, Thorlabs). After passing through a quarter wave plate (QWP, WPQ10M-780, Thorlabs), reflecting off the lateral scanning MEMS mirror M_1 , and passing back through the QWP, the beam becomes s-polarized.

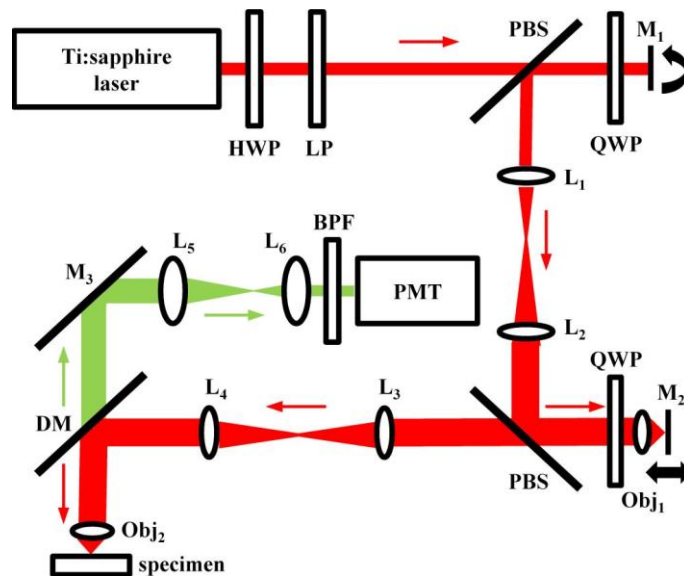


Fig. 7.1. Schematic diagram of the 3D multiphoton microscope. Compact, lightweight MEMS mirrors M_1 and M_2 are located remotely and used for lateral scanning and axial actuation, respectively. The mirrors translate the excitation wavefront between two

objectives (Obj₁ and Obj₂) that introduce equal but opposite aberrations to produce axial scanning below the surface of the specimen. Key: HWP: half wave plate, LP: linear polarizer, PBS: polarizing beam splitter, QWP: quarter wave plate, L₁₋₆: lenses, Obj_{1,2}: objectives, M₁₋₃: mirrors, DM: dichroic mirror, BPF: bandpass filter, PMT: photomultiplier tube.

After reflecting off the PBS at 90°, the excitation beam is expanded by a pair of lenses, L₁ (f = 35 mm, LA1951-B, Thorlabs) and L₂ (f = 100 mm, LA1509-B, Thorlabs) to fill the back aperture of the first objective Obj₁ (NA = 0.4, PLN 20X, Olympus). A second PBS reflects the beam through a QWP onto the axial MEMS mirror M₂. The wavefront passes back through the QWP and PBS. The beam is expanded by a pair of telescope lenses L₃ and L₄ (f = 75 mm, LA1608-B, Thorlabs), reflects off a dichroic mirror (DM, 650DCSPXR, Chroma) at 90°, and fills the back aperture of Obj₂ (NA = 0.9, LUMPlanFL/IR 60X/0.9w, Olympus), a water immersion lens. Translation of M₂ results in axial displacement of the focus below the surface of the specimen with a magnification of ~2:1. Multiphoton excited fluorescence (green arrows) generated from the specimen passes through DM, reflects off the planar mirror (M₃, PF10-03-F01, Thorlabs), and is focused by L₅ (f = 60 mm, LA1134-A, Thorlabs) and L₆ (f = 35 mm, LA1951-B, Thorlabs) through a band pass filter (BPF, FGB39, Thorlabs) that has ~80% transmission from 380–580 nm onto a photomultiplier tube (PMT, H7422-40, Hamamatsu) detector

The PMT signal is amplified by a high-speed current amplifier (59-178, Edmund Optics). We used high-speed data acquisition boards to digitize the fluorescence signal from the PMT (National Instruments, PCI-6115) and to generate control signals to drive the two MEMS scanners (National Instruments, PCI-6711). A personal computer running custom LabVIEW software was used to control and synchronize the boards. By actuating

different axes of the MEMS scanners, we were able to switch the scan direction between the horizontal (XY) and vertical (XZ) planes.

7.2.2 Optical simulation for axial scan

Two photon absorption intensity has a nonlinear relationship with laser power at the focal spot. [23] To create a uniform image during vertical sectioning, it is important to maintain the same laser intensity when M_1 is performing out of plane actuation. In the process of MEMS fabrication, the deep reactive-ion etching (DRIE) and other processes may cause asymmetric spring or mirror structure. Therefore, large stroke out of plane motion may be accompanied by a small tilt. To determine the performance requirements for the axial MEMS scanner and how the tilt angle would affect imaging, we set up an optical simulation using Zemax. Since most commercial objectives are well corrected, we created a simplified model using paraxial lenses with corresponding focal lengths to model L_5 and L_8 . We measured the axial point spread function (PSF) when M_2 is at different displacements, and the axial PSF when there is a tilt during the motion. We used the peak intensity of the axial PSF as a metric to evaluate the change of laser power at the focal spot when there is a tilt during vertical actuation.

Using this model, we were also able to calculate required axial displacement and mirror size for M_2 , and we could use this information to guide the design of the MEMS scanners. The design goal is to achieve a field of view of 250x250 μm in either the horizontal plane or the vertical plane, with a peak intensity variation less than 10% during axial scanning.

7.2.3 Lateral MEMS scanner

We have previously developed electrostatic MEMS scanners for lateral and axial scanning. [67] [126]. We used the principle of parametric resonance where large mechanical scan angles and displacements can be achieved by driving the structure at $2\omega_0/n$, where ω_0 is the natural frequency of the structure and n is an integer ≥ 1 [107]. We designed the lateral dimension of the mirror to accommodate the 1.8 mm width of the excitation beam at normal incidence. The mirror is mounted onto a gimbal frame to minimize cross-talk between the X (inner) and Y (outer) axes. Orthogonal sets of electrostatic comb-drive actuators are coupled to inner and outer torsional springs that are designed to achieve resonance for optimal scanning. On the front-side of the device, we deposited a 70 nm layer of aluminum (Al) to achieve $>85\%$ reflectivity between 200-850 nm to accommodate the range of wavelengths used for multiphoton excitation.

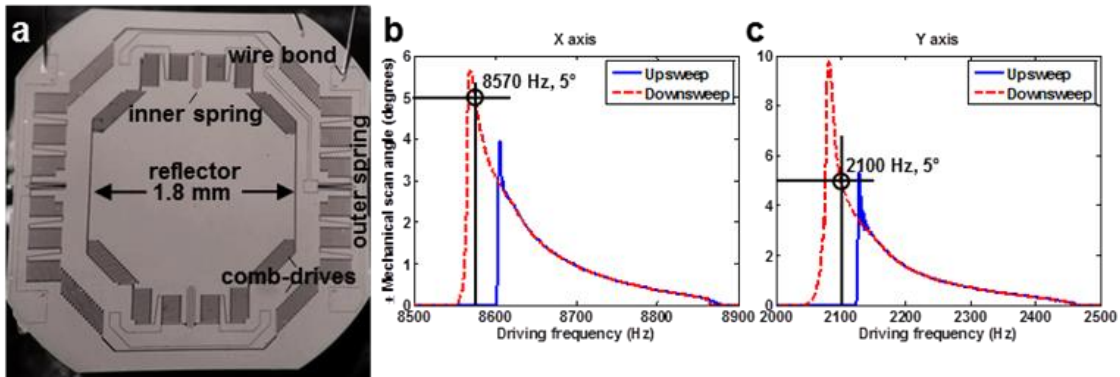


Fig. 7.2. Lateral MEMS scanner. Compact 2D MEMS scanner has a chip size of 3×3 mm² and a reflector with dimensions of 1.8 mm. a) Orthogonal electrostatic comb-drive actuators are coupled to inner and outer torsional springs to produce rapid Lissajous scanning of an aluminum (Al) coated reflector mounted on a gimbal frame. Frequency response shows mechanical scan angles $>5^\circ$ for the b) inner and $>9^\circ$ for the c) outer axes.

The compact lateral MEMS scanner M1 was fabricated with an overall chip size of $3 \times 3 \text{ mm}^2$, and the width of the reflector is 1.8 mm, **Fig. 7.2a**. We measured the angular deflection of the lateral MEMS scanner in either axis, **Fig. 7.2b,c**. The frequency response of the scanner to a sine-wave drive signal at 60 V_{pp} for rotation about the X and Y axes is shown. Large scan angles can be achieved with either a downsweep (red) or an upsweep (blue). We found greater deflection angles with a downsweep, and achieved $>5^\circ$ mechanical scan angle in both the X and Y axes. We used drive frequencies of 8570 Hz and 2100 Hz to produce actual tilt frequencies of 4285 Hz and 1050 Hz in the X and Y axes, respectively, from the parametric resonance effect. Lateral scanning about the X and Y axes forms a dense Lissajous pattern that repeats itself at 5 frames per sec to create an image with dimensions of 400×400 pixels at 100% coverage.

7.2.4 Axial MEMS scanner

For axial scanning, we developed a 1D resonant MEMS scanner that produces an out-of-plane displacement of $>400 \text{ }\mu\text{m}$ at 60 V, providing $>200 \text{ }\mu\text{m}$ axial motion at the focal point within the specimen. The optics is designed with 2:1 magnification. A circular reflector with a diameter of 2 mm is attached on two U-shaped levers via serpentine springs located at each corner. Two rows of comb-drives on each side of the scanner provide large driving forces on each lever, resulting in rotational motion of the lever about the Y axis. By rotating the levers in-phase, the circular reflector is displaced out-of-plane. However, when the levers are rotated out-of-phase, the reflector rotates about the Y axis. The serpentine springs determine the resonant frequency for each actuation mode. The springs

are designed to increase the spacing in frequency between the vertical and rotational modes to avoid crosstalk during actuation. We designed the resonant frequency to be ~ 400 Hz for vertical motion.

We used a laser displacement sensor to characterize the frequency response by measuring the out-of-plane displacement. The scanner performance was determined using an upward (low-to-high frequency) frequency sweep. Unwanted rotational motion of the reflector may occur due to minor differences in the spring dimensions. The tilt angle during axial displacement was also measured at different frequencies using a position sensing detector (PSD).

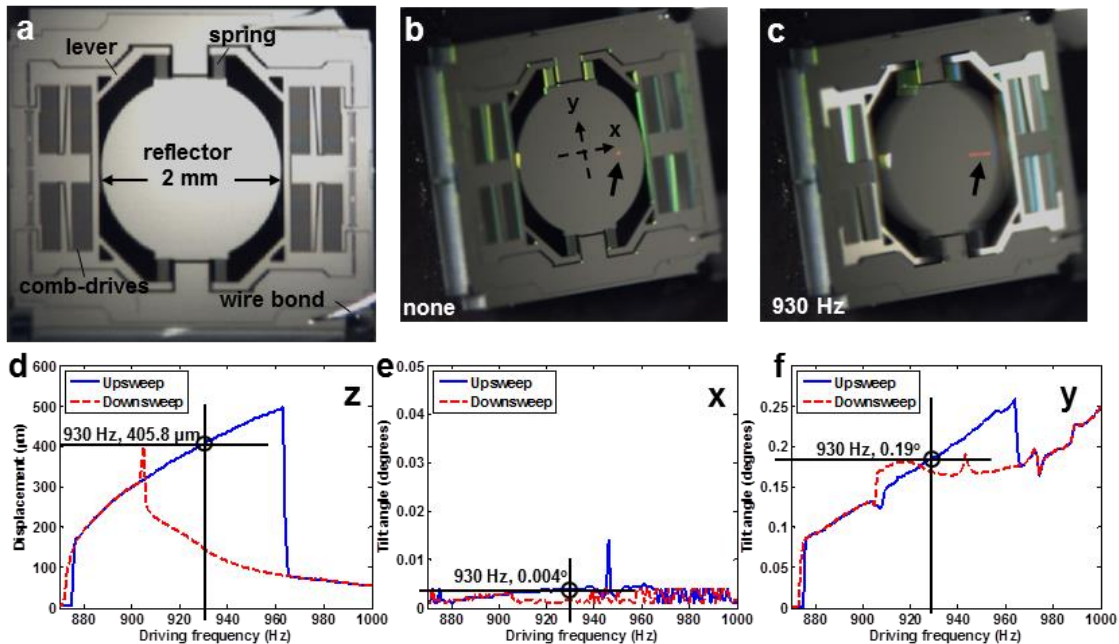


Fig. 7.3. Axial MEMS scanner. a) A 2 mm diameter circular reflector is actuated by U-shaped levers coupled to serpentine springs to produce large out-of-plane displacement. The laser spot from the displacement sensor (arrow) identifies the location of the mirror surface b) at rest and c) at resonance with 930 Hz drive frequency. The frequency response of device shows vertical displacement of $405.8 \mu\text{m}$ d) with tilt angles 0.004° for X axis e) and 0.19° for Y axis f) with 930 Hz drive frequency.

This compact 1D MEMS scanner has a chip size of $3.7 \times 3.2 \text{ mm}^2$ and a reflector with diameter of 2 mm, **Fig. 7.3a**. The axial displacement of the mirror surface is measured using a displacement sensor, and change of the laser spot is shown in **Fig. 7.3b** and **Fig. 7.3c** before and after applying the drive signal, respectively. The frequency response of the scanner is shown by sweeping the drive frequency between 850 Hz and 1000 Hz using a 60 Vpp square wave with 30% duty cycle, **Fig. 7.3d**. The device has a larger displacement during upswEEP (blue curve) compare to downswEEP (red curve). For imaging, we can achieve axial displacements $\sim 400 \text{ }\mu\text{m}$ at a drive frequency of 930 Hz, resulting in actuation at 465 Hz. Measurements of the tilt angles about X and Y axes over this frequency range are also shown in **Fig. 7.3e** and **Fig. 7.3f**. The tilt angle is less than 0.01° for X axis and less than 0.2° for Y axis when driven at 930 Hz. We also observed a rotational mode for this scanner at about 1200 Hz driving frequency which is out of the operating range for axial scanning. This shows that by properly designing the spring parameters, we can adequately separate the frequency range between axial and rotational scan modes. At the operating frequency for imaging, the scanner has very small tilt angles in both axes.

7.2.5 Switchable horizontal/vertical imaging

We can actuate both the inner and outer axes of the lateral scanner to image in the horizontal (XY) plane. Also, we can combine actuation of the inner axis of the lateral scanner with the out-of-plane motion of the axial scanner to produce images in the vertical (XZ) plane. For each imaging mode, a dense Lissajous scan pattern is formed that repeats itself at 5 frames/sec to generate either horizontal or vertical images with dimensions of

400×400 pixels at 100% coverage. Custom software was developed in LabView (National Instruments) to drive the MEMS scanners and reconstruct the image by remapping the time series signal to a 2D image using calibrated motion profiles from the scanner to generate a lookup table (LUT).

7.2.6 Optical properties characterization

First we want to quantify the relationship between the axial scanner displacement and the resulting focus location or imaging depth. The axial scanner was mounted on a motorized stage (TRA12CC, Newport) such that its position can be precisely controlled. A thin layer of fluorescent beads with 1 μm diameter (F13080, Invitrogen) on a microscope slide was used as a imaging sample for this calibration procedure. Under lateral imaging mode, the axial scanner was displaced to differently locations, and the sample was moved accordingly to maintain in focus. The position of the sample is recorded for the corresponding axial scanner position. The axial resolution was also measured at each axial scanner location, by moving the sample about the focal plane to create a vertical section of a 1 μm bead. FWHM of the axial profile was used as the metric for the axial resolution.

We also noticed that the field of view (FOV) in the lateral plane is modulated by the position of the MEMS scanner. To correctly reconstruct the vertical plane images in the X axis, we need to measure the lateral FOV size at different imaging depth. A grid target (R1L3S3P) was placed at the sample plane as an imaging target for FOV measurement. Reflectance images were acquired at different focus locations by translating the axial scanner.

7.2.7 Imaging performance demonstration

We first used autofluorescent pollen (Carolina Biological Supply Inc) with dimensions that range from 30-40 μm to demonstrate the performance of the system. We imaged the grains in both the horizontal (XY) and vertical (XZ) planes. A 3D stack of images collected in the horizontal (XY) plane was taken by moving the sample 50 μm in the axial direction with a 1 μm step size. The vertical projection (XZ) was then reconstructed, and compared with the image collected in the vertical plane (XZ) using the axial MEMS scanner.

7.2.8 Tissue preparation

All animal studies were performed in compliance with University of Michigan regulations and with approval by the University Committee on the Use and Care of Animals (UCUCA). We used a mouse genetically engineered to express tdTomato with peak multiphoton excitation at ~ 700 nm. For ex vivo imaging, mice were euthanized, and the colon was excised, rinsed with PBS to remove debris, and mounted on glass slides. We used an excitation wavelength of 750 nm and 20 mW laser power at the sample plane.

7.3 Results

7.3.1 PSF simulation

We simulated the PSF of the imaging system with the axial scan mirror M_2 located at different positions and with various tilt angles. We determined the relative intensity of the axial PSF at its peak value to evaluate the reduction in laser power at the focus. We show results for the PSF with either a 100 μm upward, **Fig. 7.4a-c**, or 100 μm downward displacement, **Fig. 7.4d-f**, of the axial scanner. Tilt angles of 0° , 0.4° , 0.8° , and 1° were evaluated. We found that tilt angles $<0.5^\circ$ keep the laser intensity stable to $<10\%$ of peak value over the range of axial displacements.

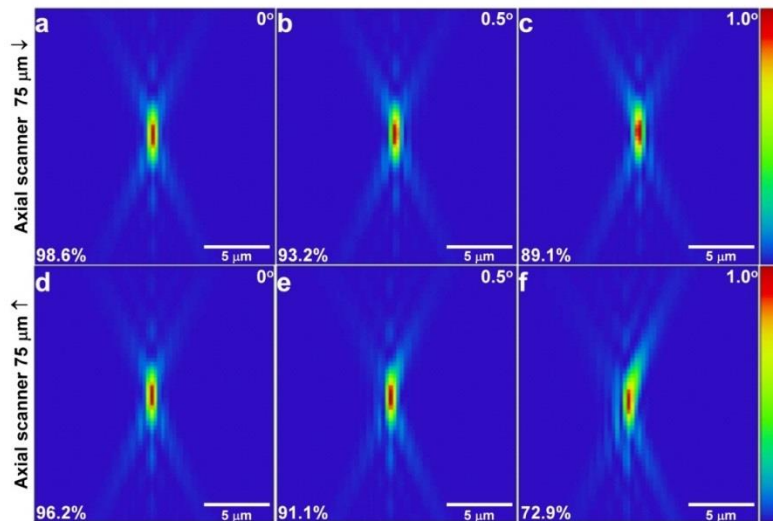


Fig. 7.4. Effect of tilt on PSF. a-c) With a 100 μm downward (\downarrow) scan, a tilt in the axial MEMS scanner of 0° , 0.5° , and 1° reduces the magnitude of the PSF to 98.6%, 93.2%, and 89.1%, respectively. d-f) With a 100 μm upward (\uparrow) scan, a tilt in the axial MEMS scanner of 0° , 0.5° , and 1° reduces the magnitude of the PSF to 96.2%, 91.1%, and 72.9%, respectively.

7.3.2 Optical properties characterization

Fig. 7.5a-c show the ray paths when the axial scanner moves out of the neutral position. When the scanner moves $200\ \mu\text{m}$ away from Obj_1 ($Z_m = -200\ \mu\text{m}$), a converging wavefront is generated and imaged onto Obj_2 , and the resulted focus is about $100\ \mu\text{m}$ closer to Obj_2 ($Z = -100\ \mu\text{m}$). Similarly, when the scanner moves closer to Obj_1 , a diverging wavefront is generated and the focus moves about $100\ \mu\text{m}$ away from Obj_2 . **Fig. 7.5d** shows a linear relationship between focus location or imaging depth with respect to axial MEMS location, with a magnification of about 2 to 1. The axial resolution is also measured at the same time, showing axial FWHMs ranging from $7\ \mu\text{m}$ to $4.5\ \mu\text{m}$ over the axial scanning range. Vertical sections of a $1\ \mu\text{m}$ bead is shown when $Z_m = -150, 0$ and $150\ \mu\text{m}$.

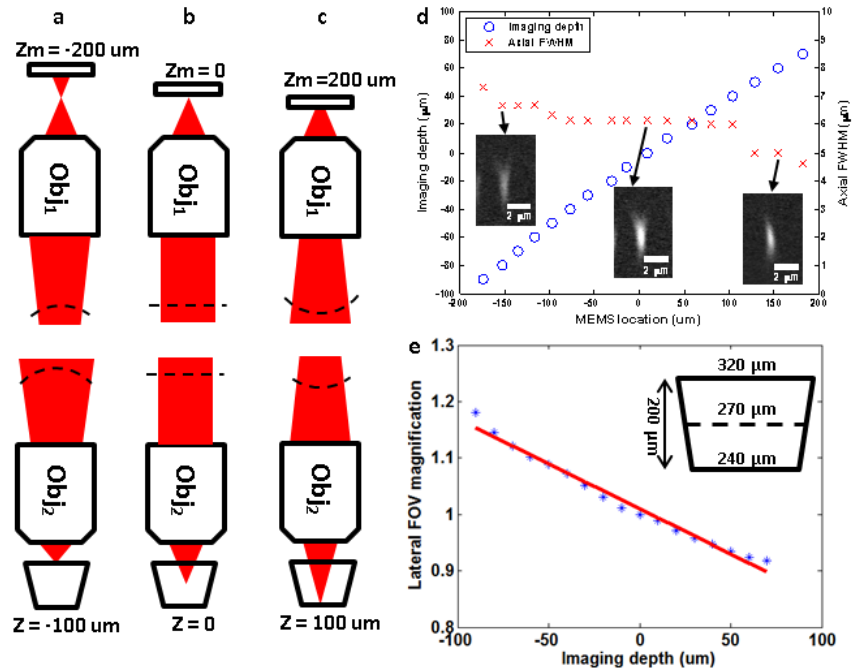


Fig. 7.5. Axial scan performance characterization. a) In the neutral position, the multiphoton excitation wavefront is imaged onto the focal plane at position $Z = 0\ \mu\text{m}$,

defined at a distance of 100 μm below the mucosal surface. b) When the axial MEMS actuator M2 moves away from Obj2, the wavefront converges, and the focal plane moves upward axially to $Z = -100 \mu\text{m}$. c) When M2 moves toward Obj2, the wavefront diverges, and the focal plane moves downward axially to $Z = 100 \mu\text{m}$. d) The position of M₂ and depth of the focal plane has a linear relationship. Axial resolution defined by FWHM varies from 4.5 to 7 μm over scan range. e) Lateral magnification ranges from 0.9 to 1.2 over relevant imaging depths.

The FOV is measured to be $270 \times 270 \mu\text{m}^2$ at the nominal position. During axial scanning, when Z changes from $-100 \mu\text{m}$ to $100 \mu\text{m}$, we found that the FOV changes from $320 \mu\text{m}$ to $240 \mu\text{m}$. This is mainly resulted from the mismatch of Obj₁ and Obj₂. Normalized FOVs are plotted against different imaging depth, **Fig. 7.5e.**

7.3.3 Axial scan performance demonstration

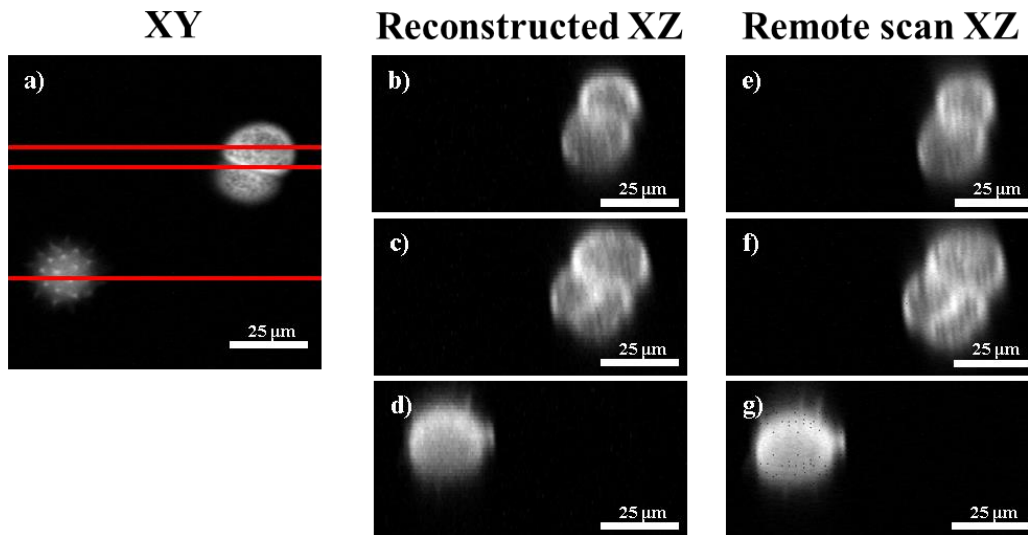


Fig. 7.6. Multiphoton excited fluorescence images of pollen grains. a) XY image using lateral MEMS scanner only. b-d) XZ images are reconstructed along planes marked by red lines in a). e-g) XZ images collected using axial MEMS scanner.

Multiphoton excited fluorescence images of pollen grains were collected to compare vertical images obtained by reconstructing a series of images collected in the horizontal plane with that collected directly in the vertical plane. A set of horizontal images

were collected over a FOV of $100 \times 100 \mu\text{m}^2$, **Fig. 7.6a**. A Z-stack was collected while moving the specimen in the axial direction over a displacement in steps of $50 \mu\text{m}$. XZ images were extracted from the 3D reconstruction along the planes identified by the red lines in **Fig. 7.6a, b–d**. We also collected XZ images directly using the axial MEMS scanner, **Fig. 7.6e–g**. Both sets of XZ images have a FOV of $100 \times 50 \mu\text{m}^2$. No differences are observed in the resolution, intensity, or contrast between these two sets of vertical images collected using either approach.

7.3.4 Tissue imaging

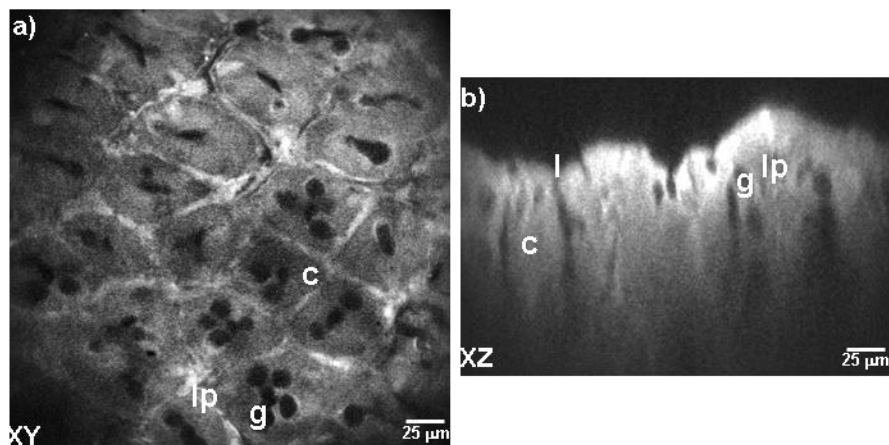


Fig. 7.7. Multiphoton excited fluorescence images of mouse colonic epithelium ex vivo. Representative image collected in the a) horizontal (XY) plane uses the lateral MEMS scanner only, and b) vertical (XZ) plane was collected using both the lateral and axial MEMS scanners. Key: crypt (arrow), lumen (l), goblet cells (g), cytoplasm (c), inflammatory cells (arrowhead), lamina propria (lp).

Multiphoton excited fluorescence images were collected ex vivo from specimens of mouse colonic epithelium that express tdTomato. These images demonstrate the potential for in vivo use to study biological phenomena using a light-weight, compact mirror that performs fast axial scanning. A representative image obtained in the horizontal

(XY) plane over a FOV of $250 \times 250 \mu\text{m}^2$ is shown, **Fig. 7.7a**. Hexagonally packed, circularly-shaped crypts (arrow) surrounding central lumen (l) with uniform dimensions can be appreciated. Goblet cells (g) can be seen with uniform fluorescence in the cytoplasm (c). Individual inflammatory cells (arrowhead) can be identified in the lamina propria (lp). An image of the same specimen was collected in the vertical (XZ) plane over a FOV of $250 \times 200 \mu\text{m}^2$, **Fig. 7.7b**, and shows the vertical anatomy of individual crypts.

7.4 Discussion

Here, we demonstrate a multiphoton microscope that uses compact lateral and axial MEMS scanners to provide fluorescence images in either the horizontal or vertical plane. Using a remote configuration, we demonstrate images from mouse colonic epithelium in the vertical plane with a depth of $\sim 200 \mu\text{m}$ without moving the specimen. These scanners use parametric resonance to achieve fast imaging speeds of 5 frames/sec, sufficient to study biological processes in live animals over time. These devices are mechanically robust, highly reliable, and fabricated at low cost with high yield. These scanners are a promising alternative to large, bulky actuators found in conventional microscopes, and can be used in an ultra-compact intravital microscope or even an endomicroscope to provide real time horizontal and vertical sectioning capabilities.

We showed results to support multiphoton excited fluorescence images collected in the vertical plane using axial beam scanning to be equivalent to reconstructing a Z-stack of horizontal (XY) images acquired by moving the stage. We present fluorescence images

collected from mouse colonic epithelium genetically engineered to express the optical reporter tdTomato with an imaging depth of $\sim 200 \mu\text{m}$ at 5 frames per sec. These results demonstrate feasibility to collecting vertical sections with an endomicroscope. We demonstrated feasibility to develop and use a miniature scanner and actuator located remotely for imaging in either the horizontal or vertical plane. In order to use the full aperture of the lateral scan mirror M_1 , we arranged the PBS and QWP so that the excitation beam is at normal incidence rather than at 45° , Fig. 1. This configuration increases the beam diameter that can be used by a factor of 1.4, and introduces less scanning induced distortion.

Recently, other efforts have been made to integrate different types of axial scanners in remote scan configurations. A commercial piezoelectric motor was used to move a mirror [137], but the speed was not reported. A fast moving mirror was constructed using a pair of identical galvanometer motors mounted in opposite directions, with scan rate up to 2.7 kHz. [118] The scanning performance was excellent with the use of well characterized and feedback controlled galvo scanner, but it is not suitable for constructing a more compact system. A voice coil motor was used to build the z-scan module with scan rate about 100 Hz. [138] Due to the position drift over time in a voice coil motor, a separate sensor and controller is needed for precise motion control. Our method has the most compact actuators for both lateral and axial scanning, and scanning performance is comparable to the above bulky actuators. We believe our technology can potentially be used to build a miniature 3D multiphoton microscope for live animal study.

Despite our promising results, our study has several limitations. In the current configuration, the back aperture of the imaging objective (Obj₂) is slightly underfilled, and partly explains why the theoretical diffraction limit for axial resolution of $\sim 1 \mu\text{m}$ with a 0.9 NA objective was not achieved. This problem can be mitigated by increasing the diameter of the lateral MEMS mirror and expand the width of the excitation beam. Also, the combined use of two resonant scanners limits collection of optical sections in either the horizontal or vertical plane. We can advance image acquisition to full 3D volumetric images by developing an axial scanner that operates in dc mode. In the vertical section, we noticed a rapid reduction in signal with increased imaging depth as a result of tissue absorption and scattering over a long optical path. We can collect more signal at greater depths by modulating the laser power. An electro-optic modulator can be used to provide the speeds needed to match the fast axial scan rate of 465 Hz achieved by our MEMS actuator. Finally, degradation in image resolution and reduced FOV can be mitigated by a better match in the optical parameters between the air and water immersion objectives Obj₁ and Obj₂.

We showed that it is feasible to develop miniature scanners for both lateral and axial plane imaging. However, there are still challenges in terms of building a miniature imaging system with these MEMS scanners. A polarization maintaining fiber with low dispersion is needed for laser pulse delivery. A miniature objective is also desired if we want to access hollow organs in small animals. Special care should be taken for packaging

and alignment since the performance of the remote scan setup is very sensitive to misalignment of the optics [139].

7.5. Summary

We demonstrate the use of compact MEMS scanners in a remote configuration to perform optical sectioning without moving either the optics or specimen. We collect multiphoton excited fluorescence images from mouse colonic epithelium that expresses tdTomato with depth of $\sim 200 \mu\text{m}$ at a frame rate of 5 Hz. This scan strategy can be used to visualize fast biological processes that develop naturally in the direction perpendicular to the tissue surface.

Chapter 8 Future Works

Several types of endomicroscopes have been demonstrated, and we found the side-viewing architecture to be most effective for in vivo imaging of mouse colon. By integrating the MEMS scanner in the distal tip of the instrument in a post-objective scan fashion, an ultra-compact endomicroscope can be developed with wide field of view and submicron resolution. Using a similar architecture, several variations of side-view probes can be developed in the future for improved depth penetration, wider field of view and 3D imaging capability. Here we present some potential designs of side-viewing endomicroscopes in three imaging modalities: multiphoton, dual axes confocal and wide-field.

8.1 Side-view multiphoton endomicroscope with distal MEMS scanning

In chapter 4, a side-view multiphoton endomicroscope was developed based on the previous handheld probe. The MEMS scanner was located in the handheld part of the probe while the reflected beam was expanded a telescope, and focused by the side-viewing optics. Due to beam scanning, the beam won't always be perpendicular to the optical components in the distal probe, therefore complicated optical design is needed to reduce the off-axis aberrations. In chapter 5 and 6, the MEMS scanner was integrated into the distal end of a confocal endomicroscope, with improved optical performance.

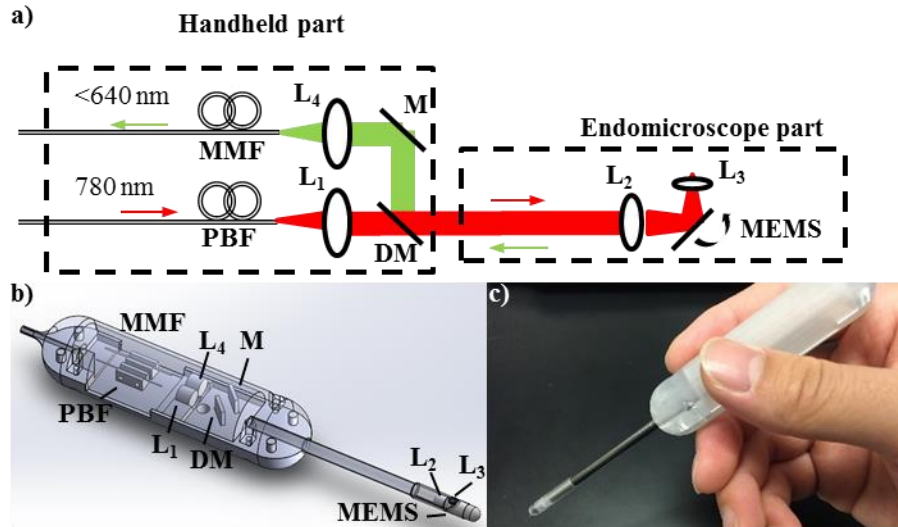


Fig. 8.1. Side-view multiphoton endomicroscope with post-objective MEMS scanning.
a) Schematic. b) CAD drawing of the probe. c) Prototype with 3D printed handheld part.

The same distal optics can be used for a multiphoton instrument with an additional handheld part for separate beam path for illumination and collection, as show in **Fig. 8.1a**. We will use a PBF for short pulse delivery with zero dispersion at 780 nm. The beam coming out of the fiber is collimated by L_1 to a diameter of 3 mm. The beam and passes through a dichroic mirror DM (62-634, Edmund Optics) into the distal imaging probe. The distal optics are the same as the previous confocal probe, with L_2 and L_3 lens combination for focusing and a 45° orientated MEMS mirror to reflect the beam to the side. Fluorescence travels in the opposite direction along the same optical path, is reflected by DM and a reflective mirror M, and is focused by lens L_4 into a multimode fiber (MMF) a large core size to maximize light collection. A CAD drawing for this design is shown in **Fig. 8.1b** and a prototype housing is shown in **Fig. 8.1c**.

8.2 Side-view multiphoton endomicroscope with remote axial scanning

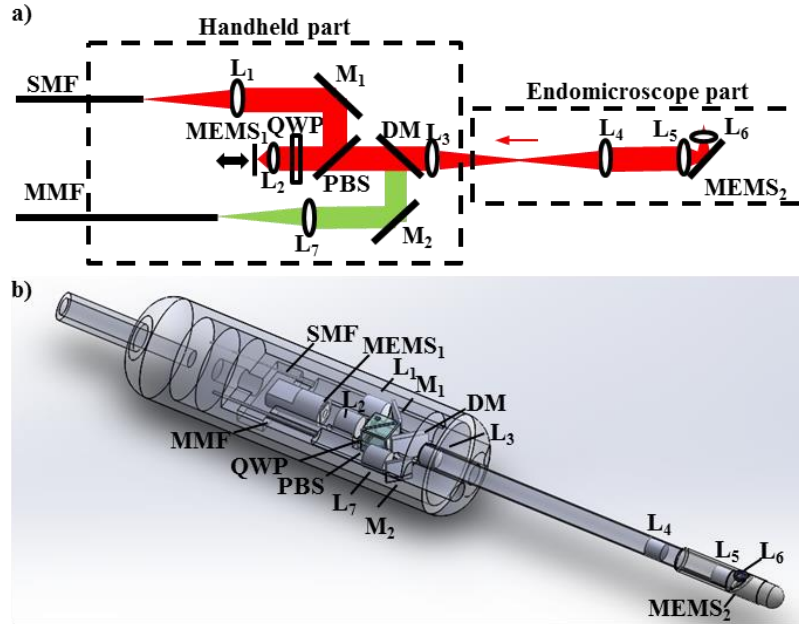


Fig. 8.2. Side-view multiphoton endomicroscope with remote axial scanning for 3D imaging. a) Schematic. b) CAD drawing of the probe.

In chapter 7 we developed a multiphoton microscope using MEMS scanners for both lateral and axial scanning. A remote axial scanning method was demonstrated in a tabletop setup where the axial displacement of the scanner will translate to a change of imaging depth in the tissue. We can incorporate this axial scanning strategy into the side-view multiphoton probe for 3D imaging capability, as shown in **Fig. 8.2a**. The collimated is reflected by a polarizing beam splitter (PBS), passes through a quarter wave plate (QWP), and is focused by the remote objective L₂ into the axial MEMS scanner. The beam passes through the PBS and a dichroic mirror (DM) into the distal imaging probe. The distal optics include a pair of relay lenses L₃ and L₄ and focusing lenses L₅ and L₆. A 2D MEMS scanner is placed in the distal end for lateral scanning. Fluorescence path is the same as the

previous multiphoton probe. In this design, the axial scanner is placed in the handheld part which reduces the size constraint of the MEMS device. A DC scanner using either electrostatic, piezoelectric or electromagnetic actuation can also be used to adjust imaging depth for 3D imaging. A CAD drawing is shown in **Fig. 8.2b**.

8.3 Side-view dual axes confocal endomicroscope

Current laser scanning microscopes use the conventional single axis optical design, shown in **Fig. 8.3a**, where the pinhole (single mode optical fiber) and objective are located along the same optical axis. Much of the light that is scattered by the tissue present between the objective and focal volume (dashed orange lines) is collected with the high NA objective, reducing the dynamic range of detection and signal to noise ratio. The dual axes architecture, shown in **Fig. 8.3b**, is an alternative to single axis confocal microscopy. Here, two fibers and low NA objectives are used for separate illumination and collection of light, using the region of overlap between the two beams (focal volume) to achieve high axial resolution [140]. Very little of the light that is scattered by tissue along the illumination path (dashed orange lines) is collected by the low NA objective, thus the dynamic range is significantly improved. We can adapt our single axis confocal endomicroscope, **Fig. 8.3c,e**, into a dual axes instrument, **Fig. 8.3d,f**. Using the same side-viewing design, two separate fibers are used for illumination and collection.

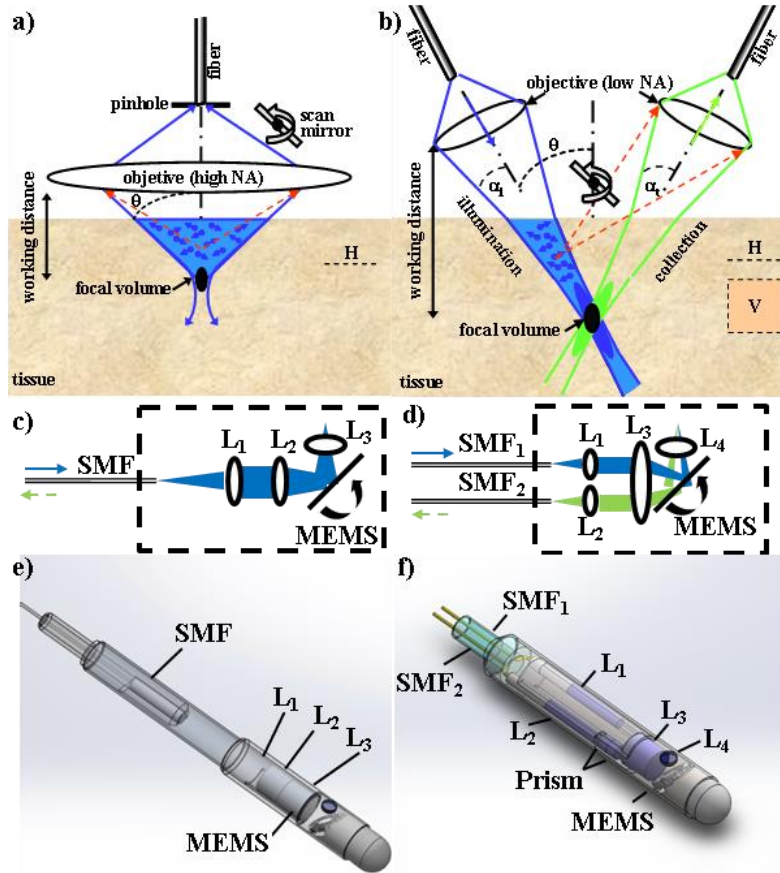


Fig. 8.3. Side-view dual axes confocal endomicroscope. a) In the conventional single axis configuration, the fiber (pinhole) is aligned with the optical axis of the objective, requiring a high NA to achieve sub-cellular resolution. b) The dual axes architecture uses separate, low NA objectives to achieve sub-cellular resolution and long working distance. Post-objective scanning provides a large field-of-view and instrument scalability to millimeter dimensions. c),e) Single axis side-view endomicroscope, schematic and CAD drawing. d),f) Dual axes side-view endomicroscope, schematic and CAD drawing.

8.4 Widefield endoscope

A widefield laser scanning endoscope can be developed with the 2D MEMS scanner, **Fig. 8.4a**. Lasers with three wavelengths, 445, 515, 660 nm, are used for illumination. These three wavelengths were chosen to image blue, green and red channels respectively. The beam coming out of the fiber is collimated and scanned by the 2D MEMS mirror, while reflectance/fluorescence signal is collected using a multimode fiber. This

geometry allows for low NA large FOV illumination, while using high NA fiber for collection. Collected signal is separated into 4 channels, including the reflectance from each channel and fluorescence generated by the red laser. 4 PMTs are used to measure the signal in 4 channels. A CAD drawing is shown in **Fig. 8.4b**. Assembled prototype, **Fig. 8.4c**, with a 2D dog bone shaped MEMS mirror **Fig. 8.4d**. When the scanner is actuated with the blue laser on, a 2D projection pattern can be seen in **Fig. 8.4e**. Widefield images were acquired in red, green, and blue channels, as shown in **Fig. 8.4f-h**. Combined color image from the three channels is shown in **Fig. 8.4i**.

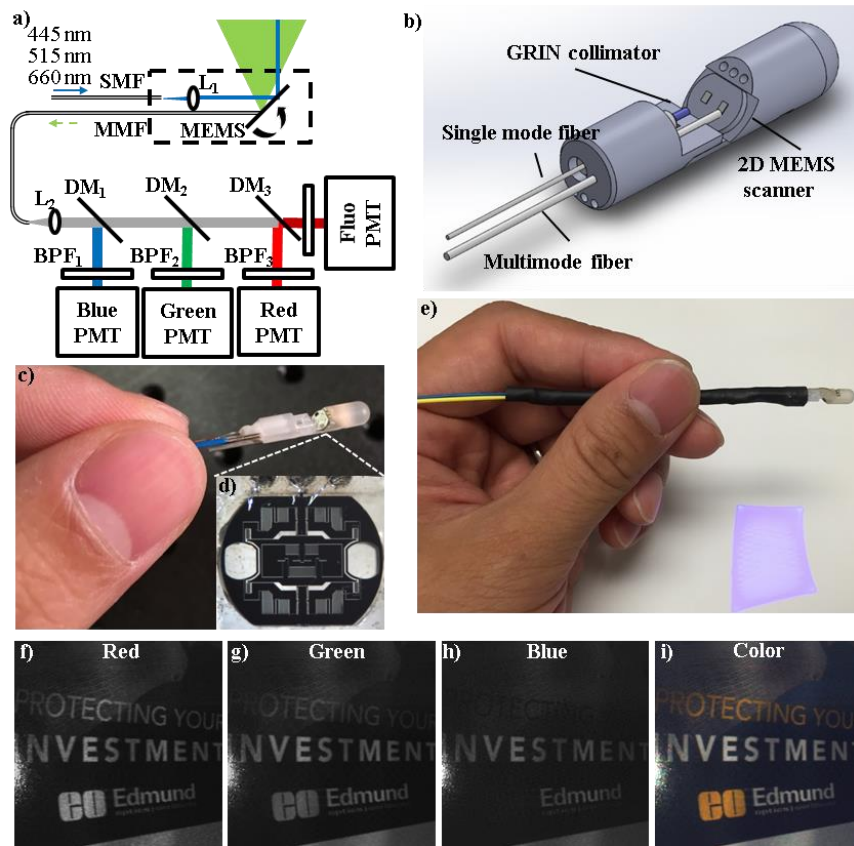


Fig. 8.4. Wide-field endoscope. a) Schematic. b) CAD drawing. c) Assembled prototype with a d) 2D dog bone shaped MEMS mirror. e). Projected 2D scan pattern for wide-field imaging. f-h) Acquired images in red, green and blue channels. f) Merged color image.

Chapter 9 Conclusion

9.1 Summary

Motivated by the need of a high-resolution imaging instrument to study small animals, several types of miniature endomicroscopes have been developed over the time of this thesis. The final version of the instrument can collect horizontal/oblique plane images in the mouse colon in real time (>10 frames/sec) with sub-micron resolution (<1 μm), deep tissue penetration (>200 μm) and large field of view (700×500 μm). A novel side-viewing architecture with distal MEMS scanning was developed to create clear and stable image in the mouse colon. With the use of the instrument, it is convenient to pinpoint location of interest and create a map of the colon using image mosaicking. Imaging performance was demonstrated *in vivo* using fluorescence-labeled peptides that specifically bind to tumors in the distal colon. This will be an extremely useful tool which will enable biologists to perform longitudinal studies *in vivo*.

Appendix

Appendix A. Matlab code for distortion profile of a 2D scan mirror

rotMat3.m

```
% Create a rotation matrix by an axis
% U = (ux, uy, uz): rotation axis
% theta: rotation angle

function output = rotMat3(U, theta)
    ux = U(1);
    uy = U(2);
    uz = U(3);
    output = [
        cos(theta)+ux^2*(1-cos(theta)), ux*uy*(1-cos(theta))-
        uz*sin(theta), ux*uz*(1-cos(theta))+uy*sin(theta);
        uy*uz*(1-cos(theta))+uz*sin(theta), cos(theta)+uy^2*(1-
        cos(theta)), uy*uz*(1-cos(theta))-ux*sin(theta);
        uz*ux*(1-cos(theta))-uy*sin(theta), uz*uy*(1-
        cos(theta))+ux*sin(theta), cos(theta)+uz^2*(1-cos(theta))];
end
```

MirrorRotationXY_45deg_plot.m

```
%%
% x: mechanical rotation about MEMS X axis
% y: mechanical rotation about MEMS Y axis
% x = (0:0.1:15)*pi/180;
% y = (0:0.1:10)*pi/180;

figure;
[x_list,y_list] = meshgrid([-10:1:10]);
for i = 1:length(x_list)
    for j = 1:length(y_list)
        x = x_list(i,j)*pi/180;
        y = y_list(i,j)*pi/180;

        S_x = [cos(x)+ sin(x/2)^2, -sqrt(2)/2*sin(x), sin(x/2)^2;
               sqrt(2)/2*sin(x), cos(x), -sqrt(2)/2*sin(x)];
```

```

        sin(x/2)^2, sqrt(2)/2*sin(x), cos(x)+sin(x/2)^2];

S_y = [cos(y) 0 sin(y);
       0 1 0;
       -sin(y) 0 cos(y)];

A = [0 0 1;
     0 1 0;
     1 0 0]; % reflection matrix for mirror at 45 degrees
input = [1 0 0]';

result = S_x*S_y*A*(S_x*S_y)'+input

% resulting optical deflection angle
angle_y = 180/pi*atan(result(1));
angle_x = 180/pi*atan(result(2));
plot(result(1)/result(3), result(2)/result(3), '.');
drawnow;
hold on;
end
axis off
end
hold off;

axis equal
axis square

```

MirrorRotationXY_90deg_plot.m

```

% x: mechanical rotation about MEMS X axis
% y: mechanical rotation about MEMS Y axis
% x = (0:0.1:15)*pi/180;
% y = (0:0.1:10)*pi/180;

figure;
% axis equal
% axis square
% axis([-12, 12, -12, 12])
[x_list,y_list] = meshgrid([-10:1:10 ]);
for i = 1:length(x_list)
    for j = 1:length(y_list)
        x = x_list(i,j)*pi/180;
        y = y_list(i,j)*pi/180;

        S_x = [cos(x), sin(x), 0;
              -sin(x), cos(x), 0;
              0, 0, 1];
    
```

```

S_y = [cos(y) 0 sin(y);
        0 1 0;
        -sin(y) 0 cos(y)];

R = [-1 0 0;
      0 1 0;
      0 0 1]; % reflection matrix for mirror at 45 degrees
input = [1 0 0]';

result = S_x*S_y*R*(S_x*S_y).'*input;
% resulting optical deflection angle
angle_y = 180/pi*atan(result(2));
angle_x = 180/pi*atan(result(3));
drawnow;
hold on;
end
end
hold off;
axis off
axis equal
axis square

```

References

1. A. Masedunskas, M. Sramkova, L. Parente, and R. Weigert, "Intravital Microscopy to Image Membrane Trafficking in Live Rats," *Methods Mol. Biol.* **931**, 153–167 (2013).
2. B. K. Edwards, A. M. Noone, A. B. Mariotto, E. P. Simard, F. P. Boscoe, S. J. Henley, A. Jemal, H. Cho, R. N. Anderson, B. A. Kohler, C. R. Ehemann, and E. M. Ward, "Annual Report to the Nation on the status of cancer, 1975-2010, featuring prevalence of comorbidity and impact on survival among persons with lung, colorectal, breast, or prostate cancer," *Cancer* **120**, 1290–1314 (2014).
3. "Cancer Facts and Figures 2016, American Cancer Society," Am. Cancer Soc. Inc (2016).
4. J. C. Van Rijn, J. B. Reitsma, J. Stoker, P. M. Bossuyt, S. J. Van Deventer, and E. Dekker, "Polyp miss rate determined by tandem colonoscopy: A systematic review," *Am. J. Gastroenterol.* **101**, 343–350 (2006).
5. T. Fujii, B. J. Rembacken, M. F. Dixon, S. Yoshida, and A. T. R. Axon, "Flat adenomas in the United Kingdom: Are treatable cancers being missed?," *Endoscopy* **30**, 437–443 (1998).

6. A. R. Hart, S. Kudo, E. H. Mackay, J. F. Mayberry, and W. S. Atkin, "Flat adenomas exist in asymptomatic people: important implications for colorectal cancer screening programmes.," *Gut* **43**, 229–231 (1998).
7. G. Gualco, N. Reissenweber, I. Cliché, and C. E. Bacchi, "Flat elevated lesions of the colon and rectum: a spectrum of neoplastic and nonneoplastic entities," *Ann. Diagn. Pathol.* **10**, 333–338 (2006).
8. P. M. Delaney, R. G. King, J. R. Lambert, and M. R. Harris, "Fibre optic confocal imaging (FOCI) for subsurface microscopy of the colon in vivo.," *J. Anat.* **184** (Pt **1**), 157–60 (1994).
9. S. H. Yun, G. J. Tearney, B. J. Vakoc, M. Shishkov, W. Y. Oh, A. E. Desjardins, M. J. Suter, R. C. Chan, J. A. Evans, I.-K. Jang, N. S. Nishioka, J. F. de Boer, and B. E. Bouma, "Comprehensive volumetric optical microscopy in vivo.," *Nat. Med.* **12**, 1429–1433 (2006).
10. T. D. Wang, S. Friedland, P. Sahbaie, R. Soetikno, P. L. Hsiung, J. T. C. Liu, J. M. Crawford, and C. H. Contag, "Functional Imaging of Colonic Mucosa With a Fibered Confocal Microscope for Real-Time In Vivo Pathology," *Clin. Gastroenterol. Hepatol.* **5**, 1300–1305 (2007).
11. R. Kiesslich, M. Goetz, E. M. Angus, Q. Hu, Y. Guan, C. Potten, T. Allen, M. F. Neurath, N. F. Shroyer, M. H. Montrose, and A. J. M. Watson, "Identification of Epithelial Gaps in Human Small and Large Intestine by Confocal Endomicroscopy,"

- Gastroenterology **133**, 1769–1778 (2007).
12. B. A. Flusberg, E. D. Cocker, W. Piyawattanametha, J. C. Jung, E. L. M. Cheung, and M. J. Schnitzer, "Fiber-optic fluorescence imaging," **2**, 941–950 (2005).
 13. M. Goetz, C. Footner, E. Schirmacher, P. Delaney, S. Gregor, C. Schneider, D. Strand, S. Kanzler, B. Memadathil, E. Weyand, M. Holtmann, R. Schirmacher, M. M. Weber, M. Anlauf, G. Klöppel, M. Vieth, P. R. Galle, P. Bartenstein, M. F. Neurath, and R. Kiesslich, "In-vivo confocal real-time mini-microscopy in animal models of human inflammatory and neoplastic diseases," *Endoscopy* **39**, 350–356 (2007).
 14. R. Cotran, V. Kumar, and S. Robbins, "Robbins And Cotran Pathologic Basis Of Disease, 7th ed," Philadelphia, PA Saunders, Ipswich, MA **69**, 1–1368 (2010).
 15. J. Fujimoto, "Optical coherence tomography for ultrahigh resolution in vivo imaging.," *Nat Biotechnol* **21**, 1361–1367 (2003).
 16. M. J. Gora, J. S. Sauk, R. W. Carruth, K. a Gallagher, M. J. Suter, N. S. Nishioka, L. E. Kava, M. Rosenberg, B. E. Bouma, and G. J. Tearney, "Tethered capsule endomicroscopy enables less invasive imaging of gastrointestinal tract microstructure.," *Nat. Med.* **19**, 238–40 (2013).
 17. T. R. C. and G. S. Kino, *Confocal Scanning Optical Microscopy and Related Imaging Systems* (Academic Press, 1996).

18. J. Art, *Photon Detectors for Confocal Microscopy* (Plenum, 2006).
19. A. D. Mehta, J. C. Jung, B. A. Flusberg, and M. J. Schnitzer, "Fiber optic in vivo imaging in the mammalian nervous system," *Curr. Opin. Neurobiol.* **14**, 617–628 (2004).
20. P. Theer, M. T. Hasan, and W. Denk, "Two-photon imaging to a depth of 1000 microm in living brains by use of a Ti:Al₂O₃ regenerative amplifier.," *Opt. Lett.* **28**, 1022–1024 (2003).
21. P. Theer and W. Denk, "On the fundamental imaging-depth limit in two-photon microscopy," *J. Opt. Soc. Am. A* **23**, 3139–3149 (2006).
22. D. Kobat, N. G. Horton, and C. Xu, "In vivo two-photon microscopy to 1.6-mm depth in mouse cortex," *J. Biomed. Opt.* **16**, 106014 (2011).
23. W. Denk, J. H. Strickler, and W. W. Webb, "Two-photon laser scanning fluorescence microscopy.," *Science* **248**, 73–6 (1990).
24. G. H. Patterson and D. W. Piston, "Photobleaching in two-photon excitation microscopy.," *Biophys. J.* **78**, 2159–62 (2000).
25. C. Xu, W. Zipfel, J. B. Shear, R. M. Williams, and W. W. Webb, "Multiphoton fluorescence excitation: new spectral windows for biological nonlinear microscopy.," *Proc. Natl. Acad. Sci. U. S. A.* **93**, 10763–8 (1996).
26. A. F. Gmitro and D. Aziz, "Confocal microscopy through a fiber-optic imaging

- bundle," *Opt. Lett.* **18**, 565 (1993).
27. E. Laemmel, "Fibered Confocal Fluorescence Microcopy (Cell-viZio tm) Facilitates Extended Imagingn in the Field of Microcirculation," *J Vasc Res* **41**, 400–411 (2004).
 28. K. Carlson, M. Chidley, K.-B. Sung, M. Descour, A. Gillenwater, M. Follen, and R. Richards-Kortum, "In vivo fiber-optic confocal reflectance microscope with an injection-molded plastic miniature objective lens.," *Appl. Opt.* **44**, 1792–1797 (2005).
 29. A. M. Buchner, M. W. Shahid, M. G. Heckman, M. Krishna, M. Ghabril, M. Hasan, J. E. Crook, V. Gomez, M. Raimondo, T. Woodward, H. C. Wolfsen, and M. B. Wallace, "Comparison of Probe-Based Confocal Laser Endomicroscopy With Virtual Chromoendoscopy for Classification of Colon Polyps," *Gastroenterology* **138**, 834–842 (2010).
 30. A. a Tanbakuchi, A. R. Rouse, J. a Udovich, K. D. Hatch, and A. F. Gmitro, "Clinical confocal microlaparoscope for real-time in vivo optical biopsies.," *J. Biomed. Opt.* **14**, 44030 (2014).
 31. W. Göbel, J. N. D. Kerr, A. Nimmerjahn, and F. Helmchen, "Miniaturized two-photon microscope based on a flexible coherent fiber bundle and a gradient-index lens objective.," *Opt. Lett.* **29**, 2521–3 (2004).
 32. G. Oh, E. Chung, and S. H. Yun, "Optical fibers for high-resolution in vivo

- microendoscopic fluorescence imaging," *Opt. Fiber Technol.* **19**, 760–771 (2013).
33. Y. S. Sabharwal, A. R. Rouse, L. Donaldson, M. F. Hopkins, and A. F. Gmitro, "Slit-scanning confocal microendoscope for high-resolution in vivo imaging.," *Appl. Opt.* **38**, 7133–7144 (1999).
 34. M. Risi, H. Makhlof, A. Rouse, A. Tanbakuchi, and A. Gmitro, "Design and Performance of a Multi-Point Scan Confocal Microendoscope," *Photonics* **1**, 421–431 (2014).
 35. M. Hughes and G. Z. Yang, "High speed, line-scanning, fiber bundle fluorescence confocal endomicroscopy for improved mosaicking," *Biomed Opt Express* **6**, 1241–1252 (2015).
 36. M. Kyriash, R. Kester, R. Richards-Kortum, and T. Tkaczyk, "Improving spatial resolution of a fiber bundle optical biopsy system," *Proc SPIE* **7558**, 755807 (2010).
 37. Y. Choi, C. Yoon, M. Kim, T. D. Yang, C. Fang-Yen, R. R. Dasari, K. J. Lee, and W. Choi, "Scanner-free and wide-field endoscopic imaging by using a single multimode optical fiber," *Phys. Rev. Lett.* **109**, 1–5 (2012).
 38. C. MacAulay, P. Lane, and R. Richards-Kortum, "In vivo pathology: Microendoscopy as a new endoscopic imaging modality," *Gastrointest. Endosc. Clin. N. Am.* **14**, 595–620 (2004).
 39. C. M. Lee, C. J. Engelbrecht, T. D. Soper, F. Helmchen, and E. J. Seibel, "Scanning

- fiber endoscopy with highly flexible, 1 mm catheterscopes for wide-field, full-color imaging.," *J. Biophotonics* **3**, 385–407 (2010).
40. S. J. Miller, C. M. Lee, B. P. Joshi, A. Gaustad, E. J. Seibel, and T. D. Wang, "Targeted detection of murine colonic dysplasia in vivo with flexible multispectral scanning fiber endoscopy," **17**, 1–11 (2012).
 41. C. J. Engelbrecht, R. S. Johnston, E. J. Seibel, and F. Helmchen, "Ultra-compact fiber-optic two-photon microscope for functional fluorescence imaging in vivo.," *Opt. Express* **16**, 5556–5564 (2008).
 42. Y. Wu, Y. Leng, J. Xi, and X. Li, "Scanning all-fiber-optic endomicroscopy system for 3D nonlinear optical imaging of biological tissues.," *Opt. Express* **17**, 7907–15 (2009).
 43. M. T. Myaing, D. J. MacDonald, and X. Li, "Fiber-optic scanning two-photon fluorescence endoscope.," *Opt. Lett.* **31**, 1076–8 (2006).
 44. D. R. Rivera, C. M. Brown, D. G. Ouzounov, I. Pavlova, D. Kobat, W. W. Webb, and C. Xu, "Compact and flexible raster scanning multiphoton endoscope capable of imaging unstained tissue," (2011).
 45. D. A. Roberts and R. R. A. Syms, "1D and 2D laser line scan generation using a fiber optic resonant scanner," *Proc. SPIE* **4075**, 62–73 (2000).
 46. E. J. Seibel, Q. Y. J. Smithwick, J. L. Crossman-bosworth, and J. A. Myers,

- "Prototype scanning fiber endoscope," **4616**, 173–179 (2002).
47. Z. Qiu and W. Piyawattanametha, "MEMS-Based Medical Endomicroscopes," *IEEE J. Sel. Top. Quantum Electron.* **21**, (2015).
 48. H. Ra, W. Piyawattanametha, Y. Taguchi, D. Lee, M. J. Mandella, and O. Solgaard, "Two-dimensional MEMS scanner for dual-axes confocal microscopy," *J. Microelectromechanical Syst.* **16**, 969–976 (2007).
 49. K. H. Kim, B. H. Park, G. N. Maguluri, T. W. Lee, F. J. Rogomentich, M. G. Bancu, B. E. Bouma, J. F. de Boer, and J. J. Bernstein, "Two-axis magnetically-driven MEMS scanning catheter for endoscopic high-speed optical coherence tomography.," *Opt. Express* **15**, 18130–18140 (2007).
 50. L. Liu, L. Wu, J. Sun, E. Lin, and H. Xie, "Miniature endoscopic optical coherence tomography probe employing a two-axis microelectromechanical scanning mirror with through-silicon vias.," *J. Biomed. Opt.* **16**, 26006 (2011).
 51. T. Naono, T. Fujii, M. Esashi, and S. Tanaka, "A large-scan-angle piezoelectric MEMS optical scanner actuated by a Nb-doped PZT thin film," *J. Micromechanics Microengineering* **24**, 15010 (2014).
 52. R. Kiesslich, J. Burg, M. Vieth, J. Gnaendiger, M. Enders, P. Delaney, A. Polglase, W. McLaren, D. Janell, S. Thomas, B. Nafe, P. R. Galle, and M. F. Neurath, "Confocal laser endoscopy for diagnosing intraepithelial neoplasias and colorectal cancer in vivo," *Gastroenterology* **127**, 706–713 (2004).

53. L. Thiberville, S. Moreno-Swirc, T. Vercauteren, E. Peltier, C. Cavé, and G. B. Heckly, "In Vivo imaging of the bronchial wall microstructure using fibered confocal fluorescence microscopy," *Am. J. Respir. Crit. Care Med.* **175**, 22–31 (2007).
54. W. Piyawattanametha, E. D. Cocker, L. D. Burns, R. P. Barretto, J. C. Jung, H. Ra, O. Solgaard, and M. J. Schnitzer, "In vivo brain imaging using a portable 2.9 g two-photon microscope based on a microelectromechanical systems scanning mirror.," *Opt. Lett.* **34**, 2309–2311 (2009).
55. H. Bao, J. Allen, R. Pattie, R. Vance, and M. Gu, "Fast handheld two-photon fluorescence microendoscope with a $475\ \mu\text{m} \times 475\ \mu\text{m}$ field of view for in vivo imaging," *Opt. Lett.* **33**, 1333 (2008).
56. K. Murakami, "A Miniature Confocal Optical Scanning Microscope for Endoscope," *MOEMS Disp. Imaging Syst. III* **5721**, 119–131 (2005).
57. W. Piyawattanametha, H. Ra, Z. Qiu, S. Friedland, J. T. C. Liu, K. Loewke, G. S. Kino, O. Solgaard, T. D. Wang, M. J. Mandella, and C. H. Contag, "In vivo near-infrared dual-axis confocal microendoscopy in the human lower gastrointestinal tract," *J. Biomed. Opt.* **17**, 21102 (2012).
58. L. Liu, E. Wang, X. Zhang, W. Liang, X. Li, and H. Xie, "MEMS-based 3D confocal scanning microendoscope using MEMS scanners for both lateral and axial scan," *Sensors Actuators A Phys.* **215**, 89–95 (2014).

59. T. Meinert, N. Weber, H. Zappe, and A. Seifert, "Varifocal MOEMS fiber scanner for confocal endomicroscopy," *Opt. Express* **22**, 31529 (2014).
60. X. Duan, H. Li, J. Zhou, Q. Zhou, K. R. Oldham, and T. D. Wang, "Visualizing epithelial expression of EGFR in vivo with distal scanning side-viewing confocal endomicroscope," *Sci. Rep.* **6**, 37315 (2016).
61. Y. Zhao, H. Nakamura, and R. J. Gordon, "Development of a versatile two-photon endoscope for biological imaging.," *Biomed. Opt. Express* **1**, 1159–1172 (2010).
62. C. L. Hoy, O. Ferhanoglu, M. Yildirim, W. Piyawattanametha, H. Ra, O. Solgaard, and A. Ben-Yakar, "Optical design and imaging performance testing of a 9.6-mm diameter femtosecond laser microsurgery probe.," *Opt. Express* **19**, 10536–52 (2011).
63. Y. Zhang, M. L. Akins, K. Murari, J. Xi, M.-J. Li, K. Luby-Phelps, M. Mahendroo, and X. Li, "A compact fiber-optic SHG scanning endomicroscope and its application to visualize cervical remodeling during pregnancy," *Proc. Natl. Acad. Sci.* **109**, 12878–12883 (2012).
64. B. Smith, M. Naji, and S. Murugkar, "Portable, miniaturized, fibre delivered, multimodal CARS exoscope," *Opt. Express* **21**, 1–5 (2013).
65. H.-Y. Chung, W.-C. Kuo, Y.-H. Cheng, C.-H. Yu, S.-H. Chia, C.-Y. Lin, J.-S. Chen, H.-J. Tsai, A. B. Fedotov, A. a. Ivanov, A. M. Zheltikov, and C.-K. Sun, "Blu-ray disk lens as the objective of a miniaturized two-photon fluorescence microscope,"

- Opt. Express **21**, 31604 (2013).
66. D. Do, H. Yoo, and D.-G. Gweon, "Fiber-optic raster scanning two-photon endomicroscope using a tubular piezoelectric actuator.," J. Biomed. Opt. **19**, 66010 (2014).
 67. X. Duan, H. Li, Z. Qiu, B. P. Joshi, A. Pant, A. Smith, K. Kurabayashi, K. R. Oldham, and T. D. Wang, "MEMS-based multiphoton endomicroscope for repetitive imaging of mouse colon," Biomed. Opt. Express **6**, 3074 (2015).
 68. G. Ducourthial, P. Leclerc, T. Mansuryan, M. Fabert, J. Brevier, R. Habert, F. Braud, R. Batrin, C. Vever-Bizet, G. Bourg-Heckly, L. Thiberville, A. Druilhe, A. Kudlinski, and F. Louradour, "Development of a real-time flexible multiphoton microendoscope for label-free imaging in a live animal.," Sci. Rep. **5**, 18303 (2015).
 69. L. Huang, A. K. Mills, Y. Zhao, D. J. Jones, and S. Tang, "Miniature fiber-optic multiphoton microscopy system using frequency-doubled femtosecond Er-doped fiber laser," Biomed. Opt. Express **7**, 1948 (2016).
 70. Y. Wang, Z. Li, X. Liang, and L. Fu, "Four-plate piezoelectric actuator driving a large-diameter special optical fiber for nonlinear optical microendoscopy," Opt. Express **24**, 19949 (2016).
 71. P.-L. Hsiung, P.-L. Hsiung, J. Hardy, S. Friedland, R. Soetikno, C. B. Du, A. P. Wu, P. Sahbaie, J. M. Crawford, A. W. Lowe, C. H. Contag, and T. D. Wang, "Detection of colonic dysplasia in vivo using a targeted heptapeptide and confocal

- microendoscopy.," *Nat. Med.* **14**, 454–8 (2008).
72. M. B. Sturm, B. P. Joshi, S. Lu, C. Piraka, S. Khondee, B. J. Elmunzer, R. S. Kwon, D. G. Beer, H. D. Appelman, D. K. Turgeon, and T. D. Wang, "Targeted Imaging of Esophageal Neoplasia with a Fluorescently Labeled Peptide: First-in-Human Results," *Sci. Transl. Med.* **5**, 184ra61-184ra61 (2013).
73. M. Li, C. P. Anastassiades, B. Joshi, C. M. Komarck, C. Piraka, B. J. Elmunzer, D. K. Turgeon, T. D. Johnson, H. Appelman, D. G. Beer, and T. D. Wang, "Affinity peptide for targeted detection of dysplasia in barrett's esophagus," *Gastroenterology* **139**, 1472–1480 (2010).
74. B. P. Joshi, S. J. Miller, C. M. Lee, E. J. Seibel, and T. D. Wang, "Multispectral endoscopic imaging of colorectal dysplasia in vivo," *Gastroenterology* **143**, 1435–1437 (2012).
75. J. Zhou, B. P. Joshi, X. Duan, A. Pant, Z. Qiu, R. Kuick, S. R. Owens, and T. D. Wang, "EGFR Overexpressed in Colonic Neoplasia Can be Detected on Wide-Field Endoscopic Imaging," **6**, e101-11 (2015).
76. E. F. Rabinsky, B. P. Joshi, A. Pant, J. Zhou, X. Duan, A. Smith, R. Kuick, S. Fan, A. Nusrat, S. R. Owens, H. D. Appelman, and T. D. Wang, "Overexpressed Claudin-1 Can Be Visualized Endoscopically in Colonic Adenomas In Vivo," *C. Cell. Mol. Gastroenterol. Hepatol.* **2**, 222–237 (2016).
77. B. P. Joshi, J. Zhou, A. Pant, X. Duan, Q. Zhou, R. Kuick, S. R. Owens, H.

- Appelman, and T. D. Wang, "Design and Synthesis of Near-Infrared Peptide for in Vivo Molecular Imaging of HER2," *Bioconjug. Chem.* **27**, 481–494 (2016).
78. M. G. Pomper, "Translational molecular imaging for cancer.," *Cancer Imaging* **5 Spec No**, S16-26 (2005).
79. S. Gross and D. Piwnica-Worms, "Molecular imaging strategies for drug discovery and development," *Curr. Opin. Chem. Biol.* **10**, 334–342 (2006).
80. R. Kneuer, H. U. Gremlich, N. Beckmann, H. Karmouty-Quintana, F. X. Blé, and M. Müller, "In vivo mouse imaging and spectroscopy in drug discovery.," *NMR Biomed* **20**, 154–185 (2007).
81. S. Ricketts, P. D. Hockings, and J. C. Waterton, "Small Animal Imaging," (2011).
82. T. Hinoi, A. Akyol, B. K. Theisen, D. O. Ferguson, J. K. Greenon, B. O. Williams, K. R. Cho, and E. R. Fearon, "Mouse model of colonic adenoma-carcinoma progression based on somatic Apc inactivation.," *Cancer Res.* **67**, 9721–30 (2007).
83. A. J. Rowan, H. Lamlum, M. Ilyas, J. Wheeler, J. Straub, A. Papadopoulou, D. Bicknell, W. F. Bodmer, and I. P. M. Tomlinson, "APC mutations in sporadic colorectal tumors: A mutational "hotspot" and interdependence of the "two hits,"" *Proc. Natl. Acad. Sci.* **97**, 3352–3357 (2000).
84. E. Gratton, E. Gratton, M. J, and M. J, "Laser Sources for Confocal Microscopy," in (2006), pp. 80–125.

85. A. Nolte, J. B. Pawley, and L. Höring, "Non-laser light sources for three-dimensional microscopy," in *Handbook of Biological Confocal Microscopy: Third Edition* (2006), pp. 126–144.
86. R. Liang, *Optical Design for Biomedical Imaging* (2010).
87. Z. Liu, S. J. Miller, B. P. Joshi, and T. D. Wang, "In vivo targeting of colonic dysplasia on fluorescence endoscopy with near-infrared octapeptide.," *Gut* **62**, 395–403 (2013).
88. Z. Qiu, Z. Liu, X. Duan, S. Khondee, B. Joshi, M. J. Mandella, K. Oldham, K. Kurabayashi, and T. D. Wang, "Targeted vertical cross-sectional imaging with handheld near-infrared dual axes confocal fluorescence endomicroscope.," *Biomed. Opt. Express* **4**, 322–30 (2013).
89. Q. Zhou, Z. Li, J. Zhou, B. P. Joshi, G. Li, X. Duan, R. Kuick, S. R. Owens, and T. D. Wang, "In vivo photoacoustic tomography of EGFR overexpressed in hepatocellular carcinoma mouse xenograft," *Photoacoustics* (2015).
90. Z. Qiu, S. Khondee, X. Duan, H. Li, M. J. Mandella, B. P. Joshi, Q. Zhou, S. R. Owens, K. Kurabayashi, K. R. Oldham, and T. D. Wang, "Vertical Cross-sectional Imaging of Colonic Dysplasia In Vivo With Multi-spectral Dual Axes Confocal Endomicroscopy," *Gastroenterology* **146**, 615–617 (2014).
91. J. Livet, T. a Weissman, H. Kang, R. W. Draft, J. Lu, R. a Bennis, J. R. Sanes, and J. W. Lichtman, "Transgenic strategies for combinatorial expression of fluorescent

- proteins in the nervous system.," *Nature* **450**, 56–62 (2007).
92. H. J. Snippert, L. G. van der Flier, T. Sato, J. H. van Es, M. van den Born, C. Kroon-Veenboer, N. Barker, A. M. Klein, J. van Rheenen, B. D. Simons, and H. Clevers, "Intestinal crypt homeostasis results from neutral competition between symmetrically dividing Lgr5 stem cells.," *Cell* **143**, 134–44 (2010).
93. L. Madisen, T. A. Zwingman, S. M. Sunkin, S. W. Oh, H. A. Zariwala, H. Gu, L. L. Ng, R. D. Palmiter, M. J. Hawrylycz, A. R. Jones, E. S. Lein, and H. Zeng, "A robust and high-throughput Cre reporting and characterization system for the whole mouse brain.," *Nat. Neurosci.* **13**, 133–40 (2010).
94. J. B. Pawley, "Confocal and two-photon microscopy: Foundations, applications and advances," *Microsc. Res. Tech.* **59**, 148–149 (2002).
95. S. Kimura and T. Wilson, "Confocal scanning optical microscope using single-mode fiber for signal detection.," *Appl. Opt.* **30**, 2143–2150 (1991).
96. R. L. Fork, O. E. Martinez, and J. P. Gordon, "Negative dispersion using pairs of prisms," *Opt. Lett.* **9**, 150 (1984).
97. E. B. Treacy, "Optical Pulse Compression With Diffraction Gratings," *IEEE J. Quantum Electron.* **5**, 454–458 (1969).
98. R. H. Stolen and C. Lin, "Self-phase-modulation in silica optical fibers," *Phys. Rev. A* **17**, 1448–1453 (1978).

99. L. Fu and M. Gu, "Fibre-optic nonlinear optical microscopy and endoscopy.," *J. Microsc.* **226**, 195–206 (2007).
100. J. Knight, *Photonic Crystal Fibres* (2003), Vol. 424.
101. F. Helmchen, D. W. Tank, and W. Denk, "Enhanced two-photon excitation through optical fiber by single-mode propagation in a large core," (2002).
102. L. Fu, X. Gan, and M. Gu, "Nonlinear optical microscopy based on double-clad photonic crystal fibers," *Opt. Express* **13**, 5528–5534 (2005).
103. L. Fu, A. Jain, H. Xie, C. Cranfield, and M. Gu, "Nonlinear optical endoscopy based on a double-clad photonic crystal fiber and a MEMS mirror.," *Opt. Express* **14**, 1027–32 (2006).
104. L. Fu, X. Gan, and M. Gu, "Nonlinear optical microscopy based on double-clad photonic crystal fibers," *Opt. Express* **13**, 5528–5534 (2005).
105. D. G. Ouzounov, K. D. Moll, M. a Foster, W. R. Zipfel, W. W. Webb, and A. L. Gaeta, "Delivery of nanojoule femtosecond pulses through large-core microstructured fibers.," *Opt. Lett.* **27**, 1513–1515 (2002).
106. W. Göbel, A. Nimmerjahn, and F. Helmchen, "Distortion-free delivery of nanojoule femtosecond pulses from a Ti:sapphire laser through a hollow-core photonic crystal fiber.," *Opt. Lett.* **29**, 1285–7 (2004).
107. K. Turner, S. Miller, and P. Hartwell, "Five parametric resonances in a

- microelectromechanical system," *Nature* **396**, 149–152 (1998).
108. H. Li, Z. Qiu, X. Duan, K. R. Oldham, K. Kurabayashi, and T. D. Wang, "2D resonant microscanner for dual axes confocal fluorescence endomicroscope," *Proc. IEEE Int. Conf. Micro Electro Mech. Syst.* 805–808 (2014).
 109. M. Hafez, T. Sidler, and R.-P. Salathé, "Study of the beam path distortion profiles generated by a two-axis tilt single-mirror laser scanner," *Opt. Eng.* **42**, 1048 (2003).
 110. W. Denk, J. H. Strickler, and W. W. Webb, "Two-photon laser scanning fluorescence microscopy.," *Science* **248**, 73–76 (1990).
 111. R. H. Webb, "Optics for laser rasters.," *Appl. Opt.* **23**, 3680 (1984).
 112. W. Piyawattanametha, R. P. J. Barretto, T. H. Ko, B. a Flusberg, E. D. Cocker, H. Ra, D. Lee, O. Solgaard, and M. J. Schnitzer, "Fast-scanning two-photon fluorescence imaging based on a microelectromechanical systems two-dimensional scanning mirror.," *Opt. Lett.* **31**, 2018–20 (2006).
 113. L. Fu, A. Jain, C. Cranfield, H. Xie, and M. Gu, "Three-dimensional nonlinear optical endoscopy.," *J. Biomed. Opt.* **12**, 40501 (2009).
 114. W. Shahid, Z. Qiu, X. Duan, H. Li, T. D. Wang, and K. R. Oldham, "Modeling and Simulation of a Parametrically Resonant Micromirror With Duty-Cycled Excitation.," *J. Microelectromech. Syst.* **23**, 1440–1453 (2014).
 115. L. Ritsma, S. I. J. Ellenbroek, A. Zomer, H. J. Snippert, F. J. de Sauvage, B. D.

- Simons, H. Clevers, and J. van Rheenen, "Intestinal crypt homeostasis revealed at single-stem-cell level by in vivo live imaging.," *Nature* **507**, 362–5 (2014).
116. R. Le Harzic, I. Riemann, M. Weinigel, K. König, and B. Messerschmidt, "Rigid and high-numerical-aperture two-photon fluorescence endoscope.," *Appl. Opt.* **48**, 3396–400 (2009).
117. D. M. Huland, C. M. Brown, S. S. Howard, D. G. Ouzounov, I. Pavlova, K. Wang, D. R. Rivera, W. W. Webb, and C. Xu, "In vivo imaging of unstained tissues using long gradient index lens multiphoton endoscopic systems.," *Biomed. Opt. Express* **3**, 1077–85 (2012).
118. E. J. Botcherby, C. W. Smith, M. M. Kohl, D. Débarre, M. J. Booth, R. Juškaitis, O. Paulsen, and T. Wilson, "Aberration-free three-dimensional multiphoton imaging of neuronal activity at kHz rates.," *Proc. Natl. Acad. Sci. U. S. A.* **109**, 2919–24 (2012).
119. P. Kim, E. Chung, H. Yamashita, K. E. Hung, A. Mizoguchi, R. Kucherlapati, D. Fukumura, R. K. Jain, and S. H. Yun, "In vivo wide-area cellular imaging by side-view endomicroscopy.," *Nat. Methods* **7**, 303–5 (2010).
120. S. Tang, W. Jung, D. McCormick, T. Xie, J. Su, Y.-C. Ahn, B. J. Tromberg, and Z. Chen, "Design and implementation of fiber-based multiphoton endoscopy with microelectromechanical systems scanning," *J. Biomed. Opt.* **14**, 34005 (2009).
121. T. Wang, Q. Li, P. Xiao, J. Ahn, Y. E. Kim, M. Kim, M. Song, E. Chung, W. K. Chung, S. Kim, P. Kim, S. Myung, and K. H. Kim, "Gradient index lens based

- combined two-photon microscopy and optical coherence tomography," **22**, 12962–12970 (2014).
122. S. Lee, J. Xie, and X. Chen, "Peptides and peptide hormones for molecular imaging and disease diagnosis," *Chem. Rev.* **110**, 3087–3111 (2010).
123. G. M. Thurber, M. M. Schmidt, and K. D. Wittrup, "Antibody tumor penetration: Transport opposed by systemic and antigen-mediated clearance," *Adv. Drug Deliv. Rev.* **60**, 1421–1434 (2008).
124. C.-H. Wu, Y.-H. Kuo, R.-L. Hong, and H.-C. Wu, "-Enolase-binding peptide enhances drug delivery efficiency and therapeutic efficacy against colorectal cancer," *Sci. Transl. Med.* **7**, 290ra91-290ra91 (2015).
125. D. Kang, R. W. Carruth, M. Kim, S. C. Schlachter, M. Shishkov, K. Woods, N. Tabatabaei, T. Wu, and G. J. Tearney, "Endoscopic probe optics for spectrally encoded confocal microscopy.," *Biomed. Opt. Express* **4**, 1925–36 (2013).
126. H. Li, X. Duan, Z. Qiu, Q. Zhou, K. Kurabayashi, K. R. Oldham, and T. D. Wang, "Integrated monolithic 3D MEMS scanner for switchable real time vertical / horizontal cross- sectional imaging," *Opt. Express* **24**, 462–471 (2016).
127. N. Barker, R. a Ridgway, J. H. van Es, M. van de Wetering, H. Begthel, M. van den Born, E. Danenberg, A. R. Clarke, O. J. Sansom, and H. Clevers, "Crypt stem cells as the cells-of-origin of intestinal cancer.," *Nature* **457**, 608–11 (2009).

128. A. L. Polglase, W. J. McLaren, S. A. Skinner, R. Kiesslich, M. F. Neurath, and P. M. Delaney, "A fluorescence confocal endomicroscope for in vivo microscopy of the upper- and the lower-GI tract," *Gastrointest. Endosc.* **62**, 686–695 (2005).
129. J. W. Jeong, M. J. Mandella, G. S. Kino, C. H. Contag, and O. Solgaard, "3-D MEMS scanning system for dual-axis confocal microendoscopy," *Int. Conf. Opt. MEMS Nanophotonics* 71–72 (2011).
130. M. Drobizhev, N. Makarov, S. Tillo, T. Hughes, and A. Rebane, "Two-photon absorption properties of fluorescent proteins," *Nat. Methods* **8**, 393–399 (2011).
131. T. Hinoi, M. Loda, and E. R. Fearon, "Silencing of CDX2 Expression in Colon Cancer via a Dominant Repression Pathway," *J. Biol. Chem.* **278**, 44608–44616 (2003).
132. E. K. Griffiths, O. Sanchez, P. Mill, C. Krawczyk, C. V. Hojilla, E. Rubin, M. M. Nau, R. Khokha, S. Lipkowitz, C.-C. Hui, and J. M. Penninger, "Cbl-3-deficient mice exhibit normal epithelial development.," *Mol. Cell. Biol.* **23**, 7708–7718 (2003).
133. H. Clevers, "The intestinal crypt, a prototype stem cell compartment," *Cell* **154**, 274–284 (2013).
134. M. J. Koehler, T. Vogel, P. Elsner, K. Köhlig, R. Bockle, and M. Kaatz, "In vivo measurement of the human epidermal thickness in different localizations by multiphoton laser tomography," *Ski. Res. Technol.* **16**, 259–264 (2010).

135. F. Helmchen, W. Go, W. Göbel, and B. M. Kampa, "Imaging cellular network dynamics in three dimensions using fast 3D laser scanning.," *Nat Methods* **4**, 73–79 (2007).
136. E. J. Botcherby, R. Juskaitis, M. J. Booth, and T. Wilson, "Aberration-free optical refocusing in high numerical aperture microscopy," *Opt. Lett.* **32**, 2007 (2007).
137. E. E. Hoover, M. D. Young, E. V Chandler, A. Luo, J. J. Field, K. E. Sheetz, A. W. Sylvester, and J. a Squier, "Remote focusing for programmable multi-layer differential multiphoton microscopy.," *Biomed. Opt. Express* **2**, 113–22 (2010).
138. P. Rupprecht, A. Prendergast, C. Wyart, and R. W. Friedrich, "Remote z-scanning with a macroscopic voice coil motor for fast 3D multiphoton laser scanning microscopy," *Biomed. Opt. Express* **7**, 1656 (2016).
139. A. D. Corbett, R. A. B. Burton, G. Bub, P. S. Salter, S. Tuohy, M. J. Booth, and T. Wilson, "Quantifying distortions in two-photon remote focussing microscope images using a volumetric calibration specimen," *Front. Physiol.* **5**, (2014).
140. T. D. Wang, M. J. Mandella, C. H. Contag, and G. S. Kino, "Dual-axis confocal microscope for high-resolution in vivo imaging.," *Opt. Lett.* **28**, 414–6 (2003).